

Transcriptional Landscape of the Dorsal Raphe Nucleus

A dissertation presented

by

Kee Wui Huang

to

The Division of Medical Sciences

in partial fulfillment of the requirements

for the degree of

Doctor of Philosophy

in the subject of

Neurobiology

Harvard University

Cambridge, Massachusetts

September 2019

© 2019 Kee Wui Huang

All rights reserved.

Transcriptional Landscape of the Dorsal Raphe Nucleus

Abstract

The dorsal raphe nucleus (DRN) is a major source of neuromodulators in the brain that has been implicated in a wide range of neurological and psychiatric disorders. However, little is known about how dysfunction of DRN neurons causes behavioral deficits. The DRN is the largest of the serotonergic nuclei housing approximately a third of all serotonergic neurons (5-HT neurons). Although it is further comprised of many other cell types that interact with 5-HT neurons, complexities at the molecular level have impeded efforts to identify and isolate specific subsets of DRN cells to study their unique contributions to the regulation of behavior.

Here we used single-cell RNA sequencing (scRNA-seq) to assess the cell type composition of the mouse DRN. We identified at least 17 major cell types and 18 distinct neuron subtypes in the DRN, of which 5 are subtypes of 5-HT neurons. We showed that these subtypes differ in their anatomical distribution and axonal projections, and described a specific 5-HT neuron subtype that is poised to regulate both motor and cognitive functions via modulation of basal ganglia circuits. This study provides a resource that lays out the cellular organization of the DRN to guide the design of molecular and genetic strategies for functional studies of the DRN and its subcircuits.

Additionally, we used scRNA-seq to characterize transcriptional changes that occur in the DRN during viral infection. Here we describe the changes in cell type composition resulting from infiltration by leukocytes, as well as both global and cell type-specific changes in gene expression mediating the antiviral inflammatory response. These results provide further insights into distinct functions performed by various non-neuronal cell types to mediate different facets of the immunological response.

Collectively, this dissertation provides an updated molecular and anatomical map of the DRN, which will serve as a framework for the molecular and genetic dissection of its diverse functions. Finally, we outline a roadmap for the continued investigation of the distinct functions of each DRN cell type and their interactions in mediating state-dependent changes in behavior.

TABLE OF CONTENTS

Abstract.....	iii
Table of Contents	v
Acknowledgements	vii
List of Figures.....	ix
Dedication	xi
Chapter 1 : Introduction	1
1.1 From Cells to Behavior: The Cell Type-Centric Framework in Neuroscience	2
1.2 Anatomical Organization of the Serotonergic System	4
1.3 Cytoarchitecture of the Dorsal Raphe Nucleus.....	6
1.4 Connectivity of DRN 5-HT Neurons	10
1.5 Functional Heterogeneity of the Dorsal Raphe Nucleus	13
Chapter 2 : Molecular and Anatomical Organization of the Dorsal Raphe Nucleus.....	15
2.1 Abstract	16
2.2 Introduction.....	17
2.3 Results	20
2.4 Discussion	73
2.5 Materials and Methods.....	87
Chapter 3 : Single-Cell Analysis of Antiviral Neuroinflammatory Responses in the Dorsal Raphe Nucleus.....	101
3.1 Abstract	102
3.2 Introduction.....	103
3.3 Results.....	104

3.4 Discussion	137
3.5 Materials and Methods.....	142
Chapter 4 : Conclusions & Future Directions.....	153
4.1 Resolving Subtypes and States from Transcriptional Heterogeneity	154
4.2 Functional Dissection of DRN Subcircuits – A Focus on the Basal Ganglia	157
4.3 From Transcriptional Types to Behavioral States	161
References	163

Acknowledgements

The graduate school experience has certainly had its fair share of joys and hardships, and I am thankful for all of the people whom I have had the privilege of sharing it with.

I am undoubtedly grateful to my advisor, Bernardo Sabatini, for the extraordinary degree of intellectual freedom that he has entrusted me with. Learning to go where the science takes us has truly been an invaluable and eye opening experience for me that would not have been possible without his support and confidence in my abilities, and I am thankful for all of the opportunities and valuable insights that he has given me over the years.

It goes without saying that the Sabatini Lab has defined much of my life as a graduate student. There are too many things to say about the lab in just a few short paragraphs, but nevertheless I am grateful for each and every single one of them – they have all taught me many valuable lessons along the way. I am especially grateful to Nicole Ochandarena, Adi Philson, and Jackie Birnbaum for all of the hard work that they have put into helping me with my many projects. I have learned so much from having had the opportunity to work with them, and I am thankful for their continued trust and friendship. I also wish to thank the many undergraduate students, Audrey, Marissa, Lauren, Maddie, Olivia, and Taylor, who have collectively provided a lot of technical assistance over the years.

I am also thankful for the wonderful people I have met through the Program in Neuroscience. I am especially grateful to Karen Harmin, who has been an amazing source of advice, support, encouragement, and chocolate over the years. Thanks also to my student committee advisors Pascal Kaeser and Rachel Wilson, as well as Lisa Goodrich, who has informally been an advisor to me thanks to our many conversations in the classroom and on the D line.

I also thank the members of my dissertation advisory committee, Susan Dymecki, Mark Andermann, Bob Datta, and John Assad, for their collective insight and support through the years with my ever-changing dissertation project.

Much of this work has also been made possible thanks to the support of Alex Ratner, Mandovi Chatterjee, and Sarah Boswell at the HMS ICCB Single Cell Core, as well as the staff of the Bauer Core Facility at Harvard University and the HMS Neurobiology Imaging Facility. Sinisa Hrvatin, Aurel Nagy, and Daniel Hochbaum have also provided valuable advice with scRNA-seq protocols and analysis pipelines. Byung Kook Lim (UCSD) and Ian Wickersham (MIT) have also generously provided both advice and reagents. Special thanks also to Arpy Saunders for being a wonderful collaborator, and for the perspectives he's given me along the way. This work has also been made possible through the generous financial support from the Harvard Brain Initiative Bipolar Disorder Seed Grant, the HMS Department of Neurobiology Graduate Fellowship, and the HMS Stuart H.Q. & Victoria Quan Fellowship in Neurobiology.

I am also grateful for my family and for all of their support and encouragement, despite being literally halfway around the planet and as far away as one could physically be from me without leaving Earth. Words are hardly used to express feelings between us, but they have never been needed to know that you all truly care.

Most importantly, a big thank you to my wife Stephanie, who has been with me every step of the way through this journey. Thank you for your love, support, and patience through it all, and I am excited to continue onwards to our next adventure together.

List of Figures

Figure 1.1: Anatomical distribution of CNS serotonergic neurons.	5
Figure 1.2: Cytoarchitectural subregions of the DRN.	7
Figure 1.3: DRN 5-HT neurons innervate a broad range of targets.....	11
Figure 2.1: High-throughput single cell transcriptomic profiling of the DRN.	22
Figure 2.2: Comparison of cell type composition across sample batches and sex.	24
Figure 2.3: Ependymal cells lining the ventral cerebral aqueduct are of several distinct subtypes.....	26
Figure 2.4: Serotonin receptors are expressed in both neurons and non-neuronal cells.	30
Figure 2.5: Neuron subtypes can be distinguished transcriptionally.	34
Figure 2.6: Average log-scaled expression of genes differentially expressed between neuron subtypes...	36
Figure 2.7: Characterization of genes differentially expressed between serotonergic neuron subtypes. ...	41
Figure 2.8: Average log-scaled expression of genes differentially expressed between 5-HT neuron subtypes.....	44
Figure 2.9: Enriched gene ontology terms associated with genes differentially expressed between 5-HT neuron subtypes.....	46
Figure 2.10: Additional validation of differential gene expression between 5-HT neuron subtypes using <i>FISH</i>	48
Figure 2.11: Processing of <i>ISH</i> images for spatial correlation analysis.....	52
Figure 2.12: Correlation coefficient maps for DRN 5-HT neuron subtypes.	54
Figure 2.13: 5-HT neuron subtypes are distributed in distinct but overlapping spatial domains.	56
Figure 2.14: Projection-defined DRN neuron subpopulations overlap with multiple 5-HT subtypes.	60
Figure 2.15: Spatial distributions of projection-defined subpopulations.	62
Figure 2.16: Ventrolateral DRN neurons send axon collaterals to both striatum and motor cortex.....	65
Figure 2.17: Caudal DRN B7 neurons innervate ventral striatum and prefrontal cortex.	66
Figure 2.18: Quantification of RNAscope puncta in Str-projecting neurons.	69
Figure 2.19: Striatum receives inputs from multiple DRN 5-HT neuron subtypes.	70

Figure 2.20: <i>Pdyn</i> ⁺ 5-HT neurons target basal ganglia circuits.	74
Figure 2.21: <i>Pet1</i> ⁺ ; <i>Pdyn</i> ⁺ neurons innervate a subset of regions targeted by DRN <i>Pet1</i> ⁺ neurons.	76
Figure 3.1: Recruitment of leukocytes in response to viral infection.	106
Figure 3.2: Leukocyte recruitment varies with infection magnitude.	108
Figure 3.3: RbV transcripts are detected in neurons and phagocytic cells.	112
Figure 3.4: Rabies infection induces both global and cell type-specific transcriptional changes.....	118
Figure 3.5: Cell type-specific expression of cytokines.	120
Figure 3.6: Type I interferon responses are induced by IFN β from microglia.	124
Figure 3.7: Identification of immune cell clusters.	126
Figure 3.8: Microglia are found in distinct transcriptional states along an activation trajectory.	130
Figure 3.9: Number of inferred interactions between cell types by condition.....	134
Figure 3.10: The structure of intercellular interactions is altered by the immune response.	136

Dedication

*This thesis is dedicated to our parents
for the sacrifices they have made so that we could pursue our passions.*

Chapter 1:
Introduction

1.1 From Cells to Behavior: The Cell Type-Centric Framework in Neuroscience

The concept that *structure informs function* is a guiding principle in the study of biology, and has been a key motivator for the development of detailed atlases, or “parts lists”, of various biological systems. These atlases range across multiple scales from the human body and its organ systems down to individual cells and their molecule constituents. In spite of the tremendous accumulation of work that has been put into building these atlases, the need for an increasingly detailed parts list for the nervous system is still one of the biggest challenges in neuroscience to this day, as evidenced by recent push for both publically- and privately-funded large scale collaborative projects aimed at cataloguing all of the cell types in the brain and human body, such as the BRAIN Initiative Cell Census Consortium (Ecker et al., 2017) and the Human Cell Atlas Project (Regev et al., 2017).

The diversity of functions performed by the nervous system can be attributed to its organizational complexity and immense heterogeneity at the cellular level. The brain is comprised of a large collection of cell types that are viewed as the fundamental operating units of neural circuits, where each cell type performs a distinct set of physiological and computational functions. The properties and functions of different cell types have not only been major topics of study, but are also crucial components of a “cell type-centric” framework which continues to guide the design of many studies that seek to understand how the nervous system is organized to generate vast behavioral repertoires (Luo et al., 2008; Luo et al., 2018).

While cell types are described as discrete building blocks of the brain, a major challenge facing efforts to build a unified cell types census of the brain has been the continuous and high-

dimensional nature of variation between individual cells. Neuronal cells types are defined on the basis of a multitude of features or dimensions that include their anatomical distribution, morphology, connectivity, passive and active electrophysiological properties, and gene expression (Zeng and Sanes, 2017). Individual cells of the same type can also vary continuously along individual dimensions, such as a single gene, such that overlaps in the range of expression by different cell types are often observed. While this points to the need for high-dimensional data to fully capture the features that uniquely define a cell type, gaining access to specific cell types to investigate their functions still requires finding appropriate low-dimensional components that can be practically exploited using molecular and genetic tools. In recent years, new methods for both acquiring and analyzing such high-dimensional data have been developed that have allowed us to address these challenges that have been major obstacles to the cell type-centric framework.

This introduction provides an overview of the challenges that have impeded efforts to apply the cell type-centric framework towards investigating the diverse functions of the serotonergic system and its roles in mediating changes in behavioral state. In this dissertation, we present a collection of work that provides a foundational roadmap for the design of cell type-centric approaches towards understanding the cellular and circuit mechanisms underlying changes in cognitive functions that occur over multiple timescales.

1.2 Anatomical Organization of the Serotonergic System

Serotonin (5-HT) is an evolutionarily conserved signaling molecule that serves many functions across many species and organ systems (Azmitia, 2010). Within the nervous system, 5-HT is released as a neurotransmitter from serotonergic neurons (5-HT neurons), which are defined by their ability to synthesize, package, and release 5-HT via fast and action potential-dependent vesicular exocytosis. Although 5-HT neurons comprise a very small fraction of the mammalian brain, at approximately 0.01% of the total number of neurons (Okaty et al., 2019), they have far-reaching effects and serve a wide range of functions in the nervous system.

The cell bodies of all 5-HT neurons in the central nervous system (CNS) are situated in the brain where they are organized into several discrete clusters (Dahlström and Fuxe, 1964). These clusters are distributed throughout the hindbrain and brainstem, and are labeled B1 to B9 in the posterior-to-anterior direction. While the B1-B9 nomenclature describes clusters of only 5-HT neurons, these clusters are located within other cytoarchitecturally-defined anatomical regions and nuclei that contain other cell types interspersed with the 5-HT neurons (Hornung, 2010). These regions, or serotonergic nuclei, include the raphe pallidus (B1), raphe obscurus (B2), raphe magnus (B3), dorsal raphe nucleus, (B6 and B7), and median raphe nucleus (B5 and B8), with the B9 cluster laterally adjacent to the median raphe nucleus. Serotonergic nuclei are also broadly categorized into two groups: the caudal group is comprised of the raphe pallidus, raphe obscurus, and raphe magnus that send descending projections into the brainstem and spinal cord, whereas the rostral group is comprised of the dorsal raphe nucleus, median raphe nucleus, and cluster B9 that collectively innervate most of the brain (Figure 1.1).

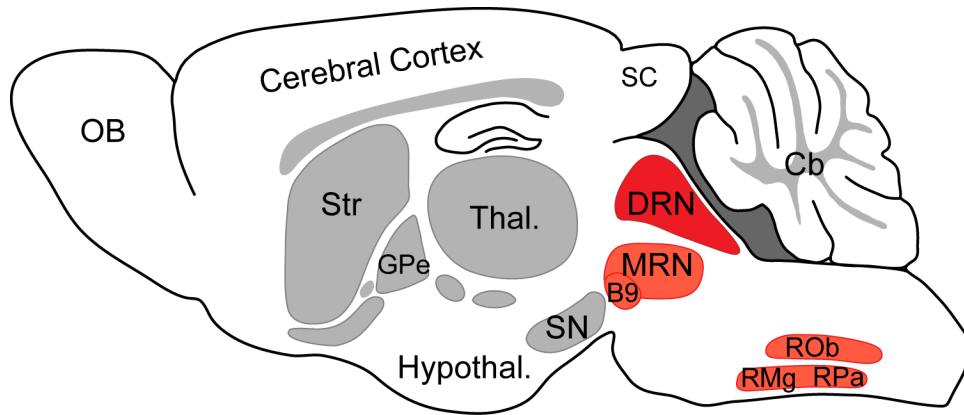


Figure 1.1: Anatomical distribution of CNS serotonergic neurons.

Sagittal schematic of the mouse brain. Major structures such as the cerebral cortex, olfactory bulbs (OB), and thalamus are labeled. Raphe nuclei in the hindbrain/brainstem regions are colored in orange, with the DRN highlighted in red. The DRN is in the rostral group along with the MRN and B9 cluster, and lies just ventral to the cerebral aqueduct (shaded dark gray). Abbreviations: Cb – cerebellum; DRN – dorsal raphe nucleus; GPe – external globus pallidus; Hypothal. – hypothalamus; MRN – median raphe nucleus; OB – olfactory bulb; RMg – raphe magnus; ROb – raphe obscurus; RPa – raphe pallidus; SC – superior colliculus; SN – substantia nigra. Str – striatum; Thal. - thalamus.

During development, neural progenitors that give rise to 5-HT neurons in these clusters are also correspondingly organized along the anterior-posterior axis of the embryonic hindbrain – progenitors giving rise to 5-HT neurons clusters of the rostral group are located in anterior rhombomeres R1-R3, whereas 5-HT neurons of the caudal group are derived from progenitors in the more posterior rhombomere R6 (Jensen et al., 2008). 5-HT neurons share a common gene expression program important for their specification and maturation, which includes the ETS-domain transcription factor *Pet1* (also known as *Fev*) (Hendricks et al., 1999; Pfaar et al., 2002; Maurer et al., 2004; Wyler et al., 2016). However, differential expression of transcription factors in different rhombomeres has allowed for the design and application of intersectional genetic

strategies for labeling and manipulating subsets of 5-HT neurons by their developmental origins (Bang et al., 2012; Okaty et al., 2015; Ray et al., 2011). The developmental and genetic diversity of 5-HT neurons are reviewed in further detail by Okaty et al. (2019), and the remainder of this introduction will be focused on the dorsal raphe nucleus.

1.3 Cytoarchitecture of the Dorsal Raphe Nucleus

The dorsal raphe nucleus (DRN) is the largest of the serotonergic nuclei, housing approximately a third of all 5-HT neurons in the brain (Hornung, 2010). The DRN is a midline structure that spans over 1 mm along the anterior-posterior axis in the anterior hindbrain. The DRN is situated just ventral to the cerebral aqueduct, and contains the 5-HT neuron clusters B6 and B7.

Classically, the DRN has been further divided into several subregions or subnuclei based on cytoarchitectural features that are visible with dyes traditionally used for the annotation of anatomical atlases of the brain, such as the Nissl stain (Paxinos and Franklin, 2001). The anterior B7-containing region, which forms most of the DRN volume, is roughly divided along the three major anatomical axes into the dorsomedial DRN (dmDRN, or DRd), ventromedial DRN (vmDRN, or DRv), interfascicular DRN (DRi), and the dorsolateral wings of the DRN (dlDRN, also sometimes referred to as vlDRN and lwDRN). Although this nomenclature has been used by many studies, it is worth noting that several of the widely used brain atlases, including the Paxinos Mouse Brain Atlas (Paxinos and Franklin, 2001) and the Allen Institute Reference Atlas (Lein et al., 2007), differ in their annotation of the DRN and its boundaries. The lack of a consensus between these atlases points towards the difficulty in delineating clear boundaries between the DRN and ventrolateral periaqueductal gray, in addition to the boundaries between DRN subregions (Figure 1.2).

In addition to 5-HT neurons, which comprise approximately 30-50% of neurons in the DRN, a number of histological studies of the DRN have also identified various neuronal populations that release other neurotransmitters that include dopamine (DA), GABA, glutamate, nitrous oxide, and several peptide hormones (Michelsen et al., 2007; Fu et al., 2010). Several DRN neuron types, including 5-HT neurons, are also capable of co-releasing several neurotransmitters, based on their expression of genes involved in the synthesis and release of different neurotransmitters. These studies also show that genes that are commonly used as “canonical markers” for distinguishing neuron types, including the GABA synthesis enzymes GAD65 (*Gad2*) and GAD67 (*Gad1*) and the vesicular glutamate transporter VGluT3 (*Slc17a8*), are expressed in multiple neuron types. These overlaps in “marker” gene expression have made it challenging to use commonly used genetic driver lines, such as the *Gad2-IRES-Cre* or *VGluT3-IRES-Cre* mouse lines, to specifically target and study the function of each cell type in isolation. This problem is further exacerbated by the close spatial intermingling between the different neuron types of the DRN, which hinders the use of anatomical approaches to target specific cell types. The function of non-5-HT neurons in the DRN has been relatively understudied compared to 5-HT neurons. Although recent studies have begun to investigate the function of these non-5HT populations in a variety of behaviors (Cho et al., 2017; Matthews et al., 2016; McDevitt et al., 2014; Nectow et al., 2017; Schneeberger et al., 2019; Seo et al., 2019), further attempts to study the unique functions of each neuron type will require a detailed assessment of the similarities and differences in their gene expression patterns to identify genetic and molecular approaches that will achieve a sufficient level of specificity.

All DRN 5-HT neurons are derived from R1 progenitors and are therefore labeled by expression of both *Pet1* and *En1*, in addition to classical “marker genes” for 5-HT neurons which include tryptophan hydroxylase 2 (*Tph2*), the rate limiting enzyme for 5-HT biosynthesis, the vesicular monoamine transporter VMAT2 (*Slc18a2*) for vesicular packaging of 5-HT, the serotonin reuptake transporter *Slc6a4* (SERT), and synaptic release machinery such as *Snap25* and *Syn1*. However, a number of studies have described molecular heterogeneity among DRN 5-HT neurons in relation to differences in their anatomical location, intrinsic membrane properties, and axonal projections (Calizo et al., 2011; Fernandez et al., 2015; Kiyasova et al., 2013; Niederkofler et al., 2016; Okaty et al., 2015; Prouty et al., 2017; Spaethling et al., 2014). Several genes that are differentially expressed between subsets of DRN 5-HT neurons are involved in the release of other neurotransmitters. A subset of DRN 5-HT neurons express the vesicular glutamate transporter VGluT3 (Fremeau et al., 2002; Gagnon and Parent, 2014; Shutoh et al., 2008), and several studies have confirmed co-release of glutamate from the terminals of 5-HT neurons in regions such as the ventral tegmental area (Liu et al., 2014; Wang et al., 2019). Some DRN 5-HT neurons have also been shown to express GAD65/67 (Okaty et al., 2015), although the co-release of GABA and 5-HT from these neurons has not been demonstrated.

Despite the extensive efforts to characterize many differences between DRN 5-HT neurons, an overall consensus regarding the organization of DRN 5-HT neurons has not been achieved. Although it is broadly agreed that DRN 5-HT neurons are heterogeneous, most studies have found that the variation in many features loosely matches the spatial distribution of 5-HT neurons. Most differences between DRN 5-HT neurons are described as gradients along a continuous scale that vary smoothly along anatomical axes without clear transitions that

correspond to spatial boundaries between subregions. Several of these studies have also been limited in their scope to differences in a small collection of candidate genes and molecules due to technical limitations of the methods used. It therefore remains to be determined if DRN 5-HT neurons are organized into molecularly distinct subsets, or subtypes, that are differentially distributed within the various subregions of the DRN.

1.4 Connectivity of DRN 5-HT Neurons

DRN 5-HT neurons collectively innervate most of the mammalian forebrain (Hornung, 2010). Many anatomical studies using double retrograde tracing and juxtacellular labeling of single DRN 5-HT neurons (Gagnon and Parent, 2014) have shown that individual 5-HT neurons can send highly branched axonal arbors to form terminal fields in several targets. Regions innervated by single 5-HT neurons can also include both cortical and subcortical regions throughout the brain (Figure 1.3). Given the high divergence of axons from this relatively small population of cells, 5-HT neurons are morphologically poised to broadcast coordinated signals across a wide range of regions and cell types.

Efferent projections of DRN 5-HT neurons are also topographically organized and vary by subregion. Anterograde tracing studies using focal injections to label small groups of 5-HT neurons in different subregions of the DRN have shown that each subregion innervates a distinct set of brain regions, although there are extensive overlaps between them (Muzerelle et al., 2016). Topography of DRN efferent projections have also been described through an extensive

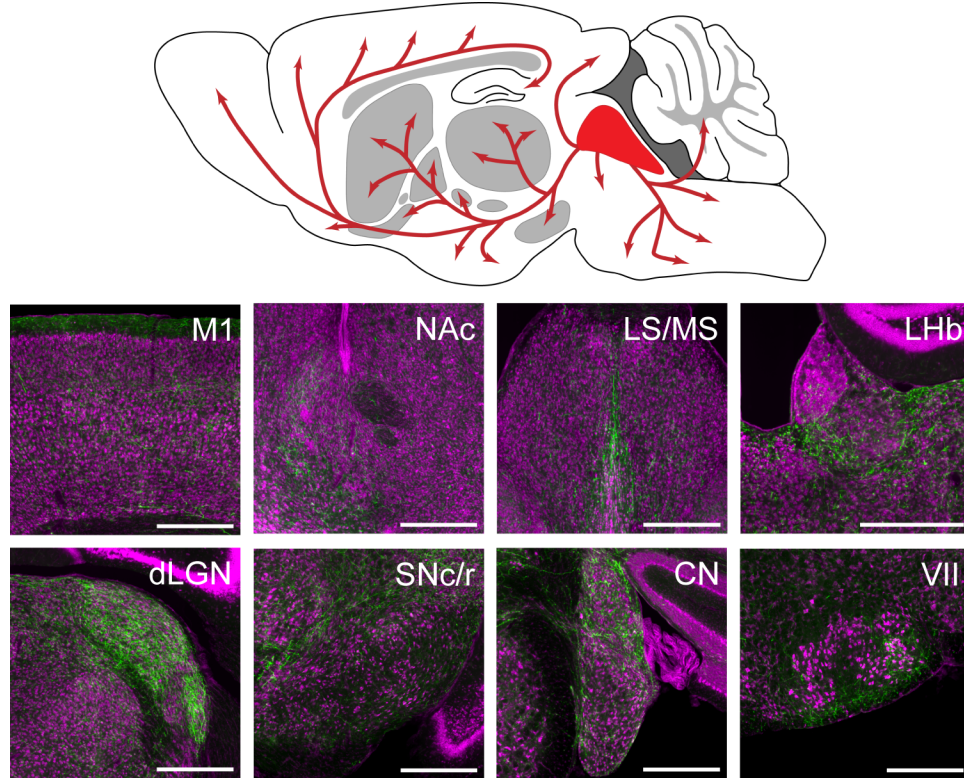


Figure 1.3: DRN 5-HT neurons innervate a broad range of targets.

Fluorescence images of coronal brain sections from anterograde tracing experiments. DRN 5-HT neurons were labeled using Cre-dependent expression of a fluorescent protein from an adeno-associated virus (AAV2/1-FLEX-EGFP). Cre-dependent AAVs were stereotactically injected into the DRN of adult *Pet1-Cre* mice. Axons of DRN 5-HT neurons (green) can be found in many regions throughout the brain, including frontal cortical areas, structures of the basal ganglia, thalamic nuclei, hypothalamus, and nuclei in the brainstem. Abbreviations: CN – cochlear nucleus; dLGN – dorsal lateral geniculate nucleus; LHb – lateral habenula; LS – lateral septum; M1 – primary motor cortex; MS – medial septum; NAc – nucleus accumbens; SNc/r – substantia nigra pars compacta/reticulata; VII – facial motor nucleus. Scale bars: 500 μm . All sections were counterstained with Neurotrace (magenta).

collection of retrograde tracing studies, which are discussed at length in several reviews (e.g. Waselus et al., 2011). The overlaps in the regions innervated by different DRN subregions and the lack of a “one-to-one” mapping are consistent with the broad innervation of multiple targets by individual 5-HT neurons. The topographical organization of these efferent projections also suggests the 5-HT mediated modulation of distinct target networks may be spatially and temporally separated by independent sets of inputs that recruit different 5-HT neuron subsets.

A large number of presynaptic inputs to DRN 5-HT neurons have been identified using cell type-specific transsynaptic tracing with genetically modified rabies viruses (Ogawa et al., 2014; Pollak Dorocic et al., 2014; Weissbourd et al., 2014). The DRN receives many reciprocal connections from structures that it innervates. A large proportion of inputs to the DRN originate from limbic structures, including the hypothalamus and amygdala, which are also heavily innervated by DRN 5-HT neurons. Neurons in frontal cortical areas, such as motor cortex and insular cortex, provide a large proportion of the cortical inputs to the DRN. DRN 5-HT neurons also receive inputs from several nuclei of the basal ganglia, including a direct GABAergic projection from the striatum. Additionally, the DRN forms reciprocal connections with dopaminergic centers in the midbrain, the ventral tegmental area (VTA) and the substantia nigra pars compacta (SNc). These structures provide dense dopaminergic inputs to basal ganglia input nuclei that are also innervated by DRN 5-HT neurons. Many of the structures innervating DRN 5-HT neurons are involved in the regulation of motivated behaviors as well as the evaluation and representation of value, and are thought to convey various signals representing different aspects of internal state to the DRN.

Axons innervating the DRN from different inputs also exhibit subregional specificity. Analyses of a large collection of anterograde tracing experiments from the Allen Institute Brain Connectivity Atlas (Oh et al., 2014) showed that DRN inputs can be clustered into several distinct groups based on the density of their axon fibers in each anatomical subregion of the DRN (Commons, 2015). The topographical organization of both inputs and outputs of the DRN have led to the proposal that the DRN is comprised of multiple subsystems, or subcircuits, that participate in distinct processes to regulate different behaviors (Hale and Lowry, 2011; Lowry, 2002; Niederkofler et al., 2016).

1.5 Functional Heterogeneity of the Dorsal Raphe Nucleus

The function of 5-HT has been of great interest given their relevance to a large number of neurological and psychiatric disorders, with selective serotonin reuptake inhibitors (SSRIs) still being used as a frontline treatment (Vaswani et al., 2003). However, the endogenous functions of 5-HT neurons have remained elusive, partly due to the numerous and at times conflicting functions that have been attributed to the DRN and 5-HT neurons.

A large number of studies have shown that DRN 5-HT neurons exhibit responses to diverse stimuli. These include both motor and sensory events during performance of a goal directed task (Ranade and Mainen, 2009), as well as both rewarding and aversive stimuli (Cohen et al., 2015; Inaba et al., 2013; Li et al., 2016; Liu et al., 2014; Nakamura et al., 2008; Ren et al., 2018; Takase et al., 2004). DRN 5-HT neurons have also been implicated in a variety of behaviors and behavioral functions that range from anxiety (Marcinkiewicz et al., 2016), aggression (Nautiyal et al., 2015; Niederkofler et al., 2016), behavioral inhibition (Miyazaki et al., 2012; Bari and

Robbins, 2013; Agnoli and Carli, 2012; Miyazaki et al., 2014), active persistence (Lottem et al., 2018), sensory gating (Davis et al., 1980; Dugue et al., 2014), wakefulness (Monti, 2011; Ursin, 2002), social preference (Dölen et al., 2013), motor facilitation (Jacobs and Fornal, 1997), and sensorimotor learning (Kawashima et al., 2016). Inflammatory damage to the DRN has also been shown to induce long-term behavioral changes that alters the stress response to induce “manic-like” behaviors (Howerton et al., 2014). Several studies performing optogenetic activation of DRN 5-HT neurons have also reported conflicting results and disagreed on whether DRN 5-HT neuron stimulation is reinforcing (Fonseca et al., 2015; Liu et al., 2014). Additionally, the effects of 5-HT neuron stimulation appear to be state-dependent (Correia et al., 2017; Lottem et al., 2018).

The diverse and conflicting functions that have been assigned to DRN 5-HT neurons can be attributed to the molecular and anatomical heterogeneity that we have outlined in the earlier sections of this introduction. While it is now well-recognized that the DRN is comprised of multiple cell types and subcircuits, the formation of a unified view of DRN function is still hindered by the lack of a reference cell atlas. Furthermore, the layout of local interactions and circuit motifs between DRN cell types that may mediate competition between functionally distinct DRN subcircuits have yet to be elucidated. Charting a reference map of DRN cell types that links their transcriptional profiles to other anatomical, physiological, and functional features will provide a common handle on each distinct cell type to facilitate the joint interpretation of results from independent studies of different DRN cell types. A reference map will also guide the design of better tools and techniques to access each cell type with sufficient specificity for the study of their actions and interactions.

Chapter 2:

Molecular and Anatomical Organization of the Dorsal Raphe Nucleus

Kee Wui Huang, Nicole E. Ochandarena, Adrienne C. Philson, Minsuk Hyun, Jaclyn E. Birnbaum, Marcelo Cicconet, and Bernardo L. Sabatini

This chapter is adapted from our publication:

Huang, K. W., Ochandarena, N. E., Philson, A. C., Hyun, M., Birnbaum, J. E., Cicconet, M., & Sabatini, B.L. Molecular and anatomical organization of the dorsal raphe nucleus. *Elife* **8**, (2019).

Author Contributions:

K.W.H. and B.L.S. designed the experiments, and K.W.H. performed most of the experiments and data analysis. N.E.O. assisted with stereotaxic injections for anatomical tracing, sample preparation for histology, and data analysis for retrograde tracing. A.C.P. assisted with rabies virus production and fluorescent *in situ* hybridization experiments. M.H. assisted with scRNA-seq experiments. J.E.B. and M.C. assisted with imaging data processing and analysis. K.W.H. and B.L.S. wrote the manuscript with contributions from the other authors.

2.1 Abstract

The dorsal raphe nucleus (DRN) is an important source of neuromodulators and has been implicated in a wide variety of behavioral and neurological disorders. The DRN is subdivided into distinct anatomical subregions comprised of multiple cell types, and its complex cellular organization has impeded efforts to investigate the distinct circuit and behavioral functions of its subdomains. Here we used single-cell RNA sequencing, *in situ* hybridization, anatomical tracing, and spatial correlation analysis to map the transcriptional and spatial profiles of cells from the mouse DRN. Our analysis of 39,411 single-cell transcriptomes revealed at least 18 distinct neuron subtypes and 5 serotonergic neuron subtypes with distinct molecular and anatomical properties, including a serotonergic neuron subtype that preferentially innervates the basal ganglia. Our study lays out the molecular organization of distinct serotonergic and non-serotonergic subsystems, and will facilitate the design of strategies for further dissection of the DRN and its diverse functions.

2.2 Introduction

The dorsal raphe nucleus (DRN) is a major source of neuromodulators in the central nervous system, and is the largest of the serotonergic nuclei, containing approximately a third of all serotonergic neurons (5-HT neurons) in the brain (Hornung, 2010). DRN 5-HT neurons send highly divergent projections that target many functionally distinct brain regions (Azmitia and Segal, 1978; Muzerelle et al., 2016; Vertes, 1991). Concordantly, diverse and at times conflicting functions have been proposed for DRN 5-HT neurons, including arousal (Monti, 2010), motor facilitation (Jacobs and Fornal, 1997), behavioral inhibition (Miyazaki et al., 2012), cognitive flexibility (Matias et al., 2017), value representation (Bromberg-Martin et al., 2010; Cohen et al., 2015; Hayashi et al., 2015; Li et al., 2016), motor learning (Kawashima et al., 2016), mood (Cools et al., 2008), and regulation of social interactions (Dölen et al., 2013; Niederkofler et al., 2016). Changes in DRN 5-HT neuron function have been implicated in various neuropsychiatric diseases, including major depressive disorder, bipolar disorder, schizophrenia, and obsessive-compulsive disorder, as well as movement disorders such as Parkinson's Disease (Huot et al., 2011; Mahmood and Silverstone, 2001; Politis and Niccolini, 2014; Vaswani et al., 2003). Serotonergic signaling pathways are also targets of widely-used therapeutic drugs, such as selective serotonin reuptake inhibitors (SSRIs) and atypical antipsychotics (Meltzer and Massey, 2011; Vaswani et al., 2003). However many of these drugs can acutely induce adverse side effects including anxiety and increased risk of suicidal behaviors (Ferguson, 2001; Gartlehner et al., 2011; Vaswani et al., 2003). This suggests these drugs affect multiple 5-HT pathways with distinct and contrasting effects on behavior and highlights the need for new approaches to target specific 5-HT neurons and their outputs (Marcinkiewicz et al., 2016; Urban et al., 2016). Understanding of the organization of the DRN and 5-HT neurons in functionally distinct

subsystems may help explain conflicting conclusions for the role of serotonin in the etiology of mental disorders.

Neurons in the DRN are neurochemically and anatomically diverse – only 30 to 50% are serotonergic, and many release other neurotransmitters including GABA, glutamate, dopamine (DA), nitric oxide, and a variety of peptides (Fu et al., 2010). Some DRN neurons co-express genes that are traditionally used as markers for different neuronal cell types based on their neurotransmitter usage (e.g. *Gad1*, *Gad2*, *Slc17a6*, and *Slc17a8*) (Fu et al., 2010; Okaty et al., 2015). This presents a major challenge to attempts at separating cell types in the DRN using many genetic driver lines, which will label mixed populations in the DRN that have overlapping expression of these “canonical” marker genes. Furthermore, these distinct neuronal cell types are spatially intermingled within the DRN and are difficult to separate anatomically.

Even bona fide DRN 5-HT neurons are molecularly, anatomically, and physiologically heterogeneous. Cytoarchitecturally, the DRN contains the 5-HT neuron clusters B6 and B7 (Dahlström and Fuxe, 1964; Hornung, 2010), and is further divided into subregions along all three major anatomical axes (Hale and Lowry, 2011). While these subregions can be roughly defined by the spatial clustering of 5-HT neurons, the density of 5-HT neurons varies gradually between the subregions preventing the delineation of clear boundaries. Although DRN 5-HT neurons share a common developmental lineage (Deneris and Gaspar, 2018; Jensen et al., 2008), DRN 5-HT neurons in different subregions express different G protein-coupled receptors and vesicular transporters, suggesting spatial clustering of functionally specialized neurons (Calizo et al., 2011; Fernandez et al., 2015; Lowry et al., 2000; Templin et al., 2012). Nevertheless, these

anatomical subregions fail to capture many features of 5-HT neurons, as most of the variation does not show subregional specificity. Additionally, DRN 5-HT neurons vary in their axonal projection patterns, and the spatial distributions of these projection-defined subpopulations are broad and do not map cleanly to DRN subregions. This likely arises, in part, from the extensive collateralization of axons from individual 5-HT neurons (Gagnon and Parent, 2014; Waselus et al., 2011) – different 5-HT neurons are therefore likely to have overlapping axonal projection fields, even if they target distinct sets of regions to serve separate functions.

The heterogeneity of 5-HT neurons suggests that they may be organized into distinct subsystems. However, there is no consensus on the definition of these subsystems and only an incomplete understanding of correspondences between anatomically, molecularly, and functionally defined 5-HT neuron subtypes. Functional differences exist between projection-defined subpopulations of DRN 5-HT neurons (Ren et al., 2018), but it is unknown if these subpopulations map onto molecularly defined subtypes. Furthermore an unbiased census of DRN cell types and subtypes of 5-HT neurons is lacking, and presents a major obstacle in achieving a unified understanding of the diverse functions performed by these neurons.

Here we dissect the cellular composition of the DRN and relate molecular profiles of cell types to anatomical features. We used high-throughput single-cell RNA sequencing (scRNA-seq) to survey the cell types in and around the DRN and identified at least 5 distinct subtypes of 5-HT neurons, in addition to uncovering organizational principles for both neuronal and non-neuronal cell types based on gene expression profiles. Spatial information from *in situ* hybridization imaging datasets allowed us to infer the anatomical distribution of these DRN 5-HT neuron

subtypes within the DRN. Molecularly defined subtypes of DRN 5-HT neurons are found in overlapping but different sets of anatomical subregions that do not match the spatial distribution of projection-defined subpopulations. Using viral retrograde tracing and multiplexed *in situ* hybridization, we characterized the expression of subtype-enriched genes in projection-defined neuronal subpopulations and found that the striatal-projecting 5-HT neuron subpopulation is a heterogeneous group comprised of at least 2 distinct molecular subtypes. Additionally, we defined a DRN 5-HT neuron subtype that is well-positioned to modulate basal ganglia circuits, based on its molecular and anatomical features. Our findings validate the feasibility of intersectional approaches to achieve the molecular and spatial specificity required to access distinct 5-HT neuron subsystems *in vivo*, and provide a resource to aid in the design of experimental strategies for the functional dissection of diverse DRN cell types and circuits.

2.3 Results

Cell type composition of the DRN by transcriptomic profiling

To survey the cell type composition of the DRN, we used the droplet-based inDrop platform (Klein et al., 2015; Zilionis et al., 2017) to perform transcriptomic profiling with single-cell resolution (Figure 2.1A). The DRN and surrounding areas were dissected from acute coronal brain sections spanning the rostro-caudal extent of the DRN, and dissociated cell suspensions were prepared by digesting the dissected tissue in a protease cocktail containing inhibitors of neural activity, transcription, and translation to reduce the effects of the dissociation procedure on gene expression (Hrvatin et al., 2018). Cells were sequenced to an average read depth of 48,805 reads per cell (median = 31,286 reads), and low-quality cells were removed prior to clustering (see Methods). Aligned reads were filtered using unique molecular identifiers (UMIs)

and quantified as UMI filtered mapped read (UMIFM) counts. Clustering using a graph-based algorithm and a shared-nearest-neighbors distance metric grouped yielded 17 major clusters (Figure 2.1B). These major clusters were identified and assigned to cell classes based their expression of previously-described marker gene combinations that were extensive cross-referenced with published datasets (Marques et al., 2016; Okaty et al., 2015; Poulin et al., 2014; Saunders et al., 2018; Vanlandewijck et al., 2018; Zeisel et al., 2018) (Figure 2.1C). Smaller clusters containing putative doublets were identified based on co-expression of marker genes from different cell types and were removed manually. The processed dataset contained 39,411 cells from 8 mice (4 male and 4 female, age range 8-10 weeks) with a median UMIFM count of 2333 counts per cell (min. = 548, max. = 17976, IQR = 1903) and median gene detection rate of 1034 genes per cell (min. = 216, max. = 5765, IQR = 693). Cells from male and female mice were pooled for analysis as no major transcriptional sex differences were observed (Figure 2.2).

The majority of cells in the dataset were non-neuronal cells that included astrocytes, oligodendrocyte precursor cells (or polydendrocytes), differentiating and mature oligodendrocytes, ependymal cells of the cerebral aqueduct, lymphocytes, microglia, perivascular macrophages (pvMΦs), fibroblast-like or mesenchymal cells, endothelial cells, pericytes, and smooth muscle cells. Iterative subclustering identified subtypes of cells within each major non-neuronal class that included novel subpopulations – in addition to resolving different subtypes of endothelial cells (Vanlandewijck et al., 2018) and developmental stages of oligodendrocytes (Marques et al., 2016), we found multiple subtypes or states of astrocytes, oligodendrocytes, and ependymal cells. Ependymal cells shared expression of the histamine

Figure 2.1: High-throughput single cell transcriptomic profiling of the DRN.

(A) Schematic for scRNA-seq using the inDrop platform. (1) Tissue containing the DRN and surrounding regions was microdissected from acute coronal brain slices prepared from adult C57BL/6J mice. (2) Tissue chunks were digested in a cocktail of proteases and inhibitors of neuronal spiking, transcription, and translation. Digestion was followed by trituration and filtration to obtain a cell suspension. (3) Single cells were encapsulated using a droplet-based microfluidic device for cell barcoding and RNA capture.

(B) t-SNE plot of the processed dataset containing 39,411 cells from 8 animals. Cells are color-coded according to the cluster labels shown in (C). **(C)** Left: Dendrogram with cell class labels corresponding to clusters shown in (B). Right: Dot plot displaying expression of example genes used to identify each major cell class. The color of each dot (blue to red) indicates the relative expression of each gene whereas the dot size indicates the fraction of cells expressing the gene.

Figure 2.1 (Continued)

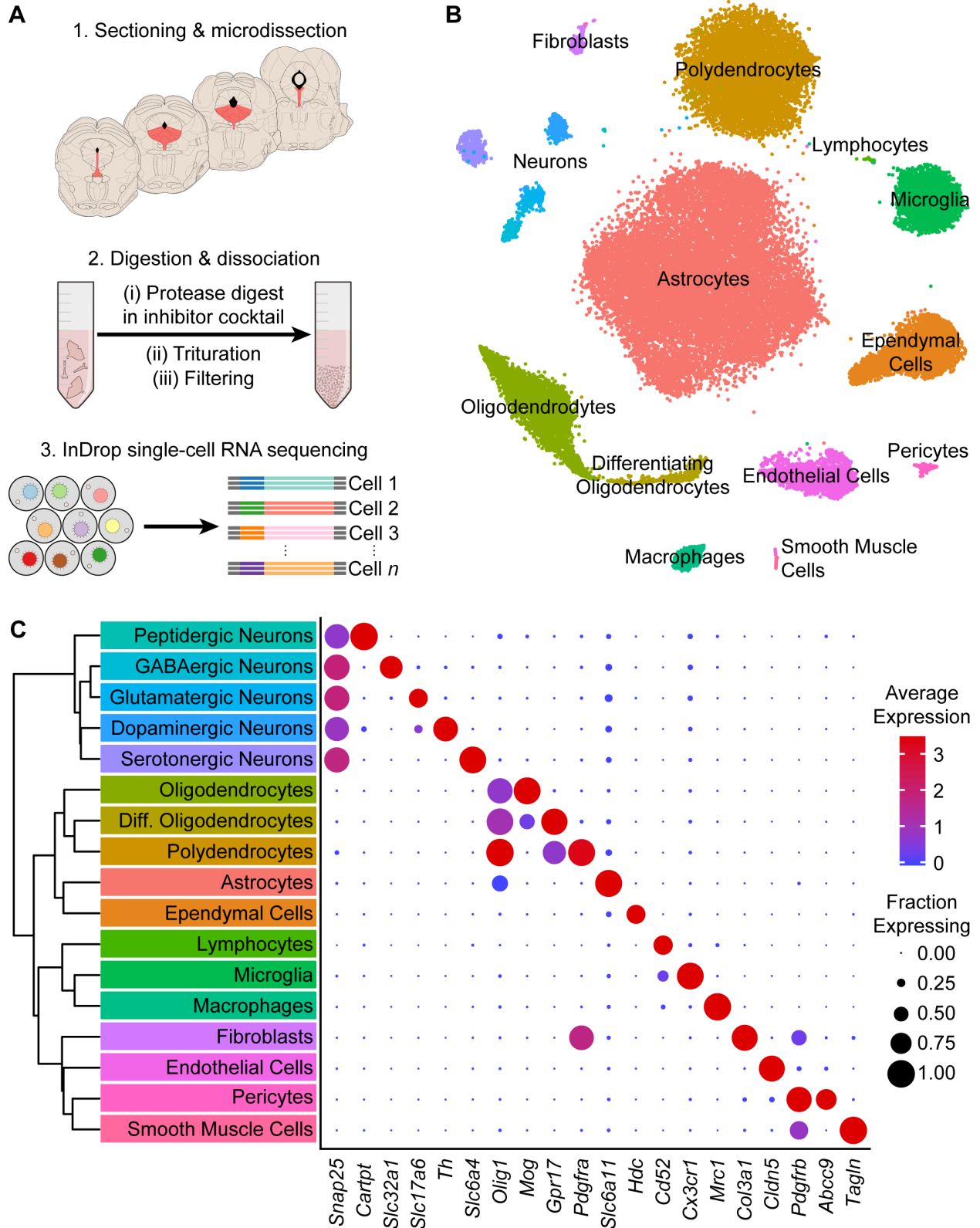


Figure 2.2: Comparison of cell type composition across sample batches and sex.

(A) t-SNE plot of the dataset with cells color-coded by experiment batch. All clusters contain cells from both batches. (B) t-SNE plot of the dataset with cells color-coded by the sex of the mouse from which the sample was acquired. (C) Bar plots showing the percentage of cells in each batch (left) or sex (right) that are categorized into each of the 17 major cell types.

Figure 2.2 (Continued)

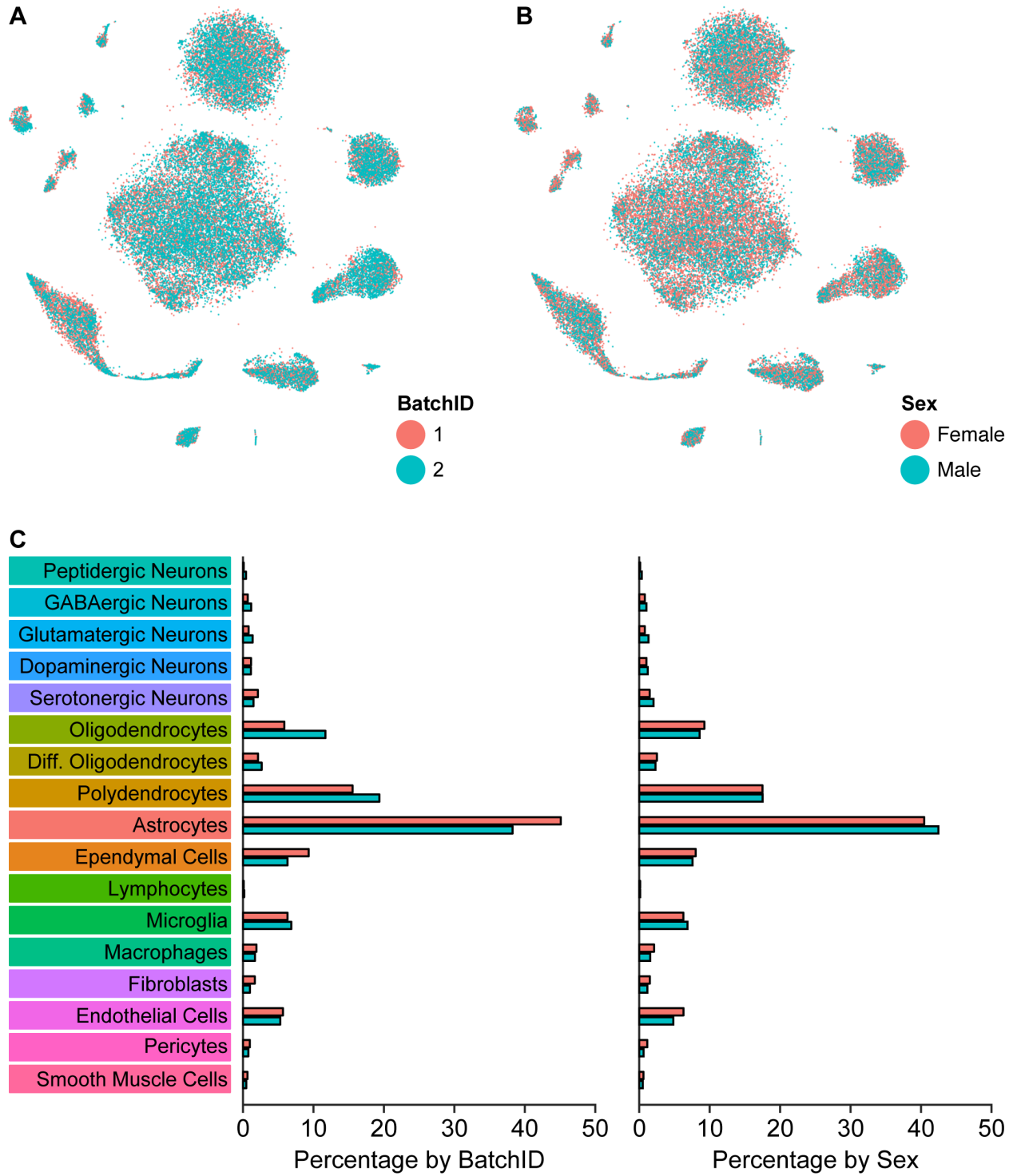
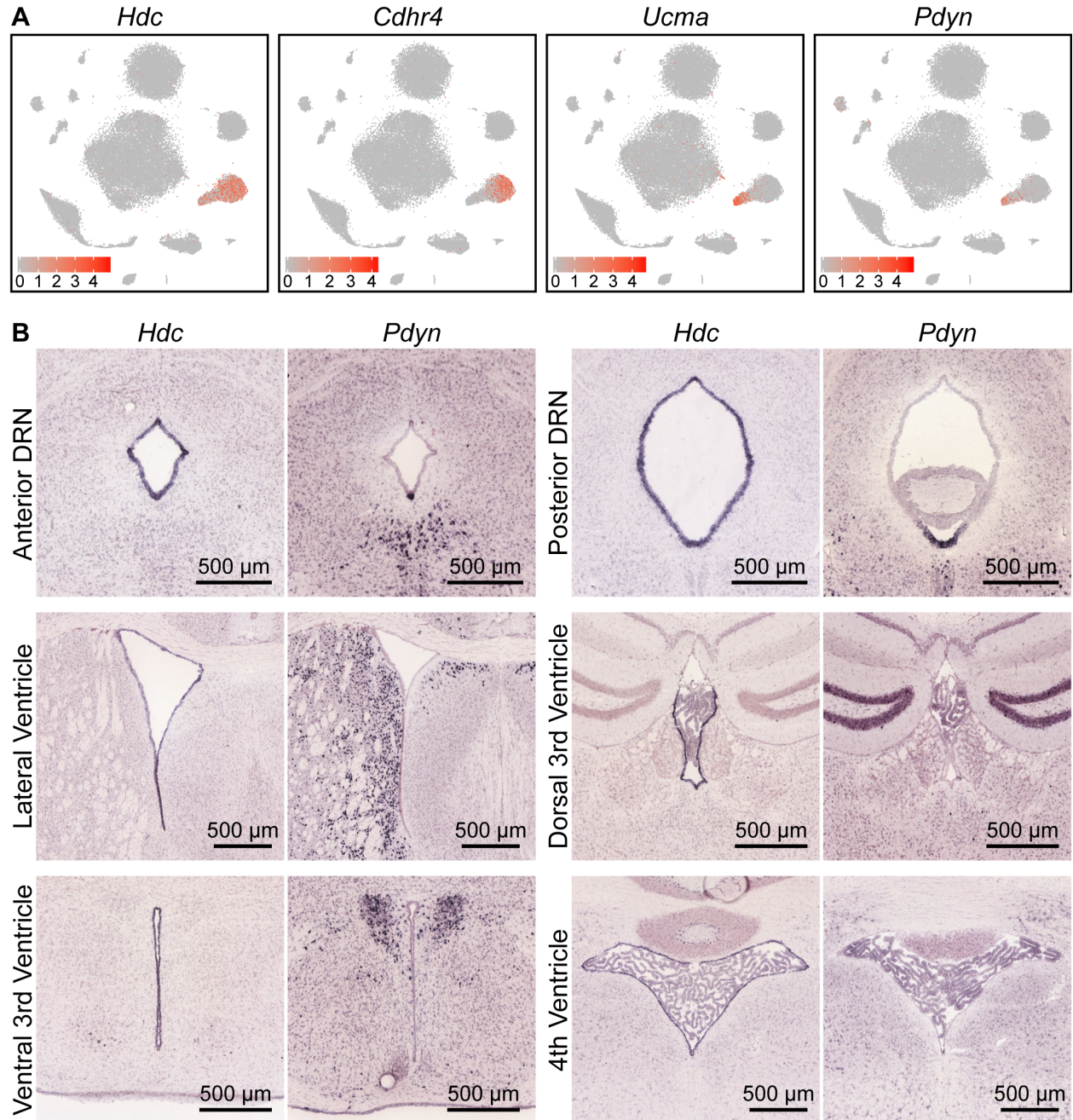


Figure 2.3: Ependymal cells lining the ventral cerebral aqueduct are of several distinct subtypes.

(A) t-SNE plots of the dataset, with cells color-coded by their expression of genes identifying different subsets of ependymal cell. *Hdc* is expressed in all ependymal cells, whereas genes such as *Cdhr4*, *Ucma*, and *Pdyn* are expressed in distinct subsets. **(B)** Images of coronal *ISH* from the Allen Brain Atlas showing expression of *Hdc* and *Pdyn* at various parts of the ventricular system. *Hdc* is expressed by ependymal cells lining most of the ventricular system. *Pdyn* expression is specific to the cells lining the ventromedial part of the posterior ventricular system, where it is highly expressed in the cerebral aqueduct, but not the lateral ventricles or 3rd ventricle.

Figure 2.3 (Continued)



synthesis gene *Hdc*, but were further divided into distinct subtypes that differed in expression of cell adhesion and matrix-associated genes as well as signaling peptides such as *Pdyn* (Figure 2.3). *In situ* hybridization (*ISH*) analyses of these differentially expressed genes revealed that these ependymal cell subtypes are topographically organized along major anatomical axes – *Pdyn*-expressing ependymal cells are restricted to ventromedial ventricular walls of the midbrain and hindbrain but are absent from the lateral and third ventricles in the forebrain (Figure 2.3B), suggesting zonation of functionally specialized ependymal cell subtypes throughout the ventricular system. Furthermore, the presence of these molecules used for both paracrine and synaptic communication suggests a locally specialized function of ependymal cells in signaling directly to neurons and other cells that express the appropriate G-protein coupled receptors, such as κ -opioid and histamine receptors.

Neurons ($n = 2,041$ cells), identified by expression of genes required for chemical synaptic transmission such as *Snap25*, clustered into 5 main classes that could be distinguished by their neurotransmitter usage. The 5 major neuronal classes (in decreasing order of abundance) are 5-HT, dopaminergic (DA), GABAergic, glutamatergic, and peptidergic neurons. Peptidergic neurons were depleted of genes for the synthesis and release of small molecule neurotransmitters (e.g. *Slc6a4*, *Slc6a3*, *Slc32a1*, *Slc17a6*, *Slc17a8*), but were highly enriched for the genes encoding neuropeptides such as *Cck*, *Cartpt*, *Ucn*, and *Postn*. Inspection of *ISHs* from the Allen Brain Atlas (Lein et al., 2007) indicated that these neurons were located in the Edinger-Westphal nucleus, which is adjacent to the DRN, confirming that our dissection region spanned most of the DRN along the anterior-posterior axis. Inspection of rhombomere-specific marker gene expression in the 5-HT neuron cluster showed a lack of markers for R2 (*Hoxa2*) and R3/5 (*Egr2*)

derived neurons in contrast to the expression of R1 markers (*En1* and *En2*), indicating that our dissection, as intended, excluded most of the median raphe nucleus (Okaty et al., 2015).

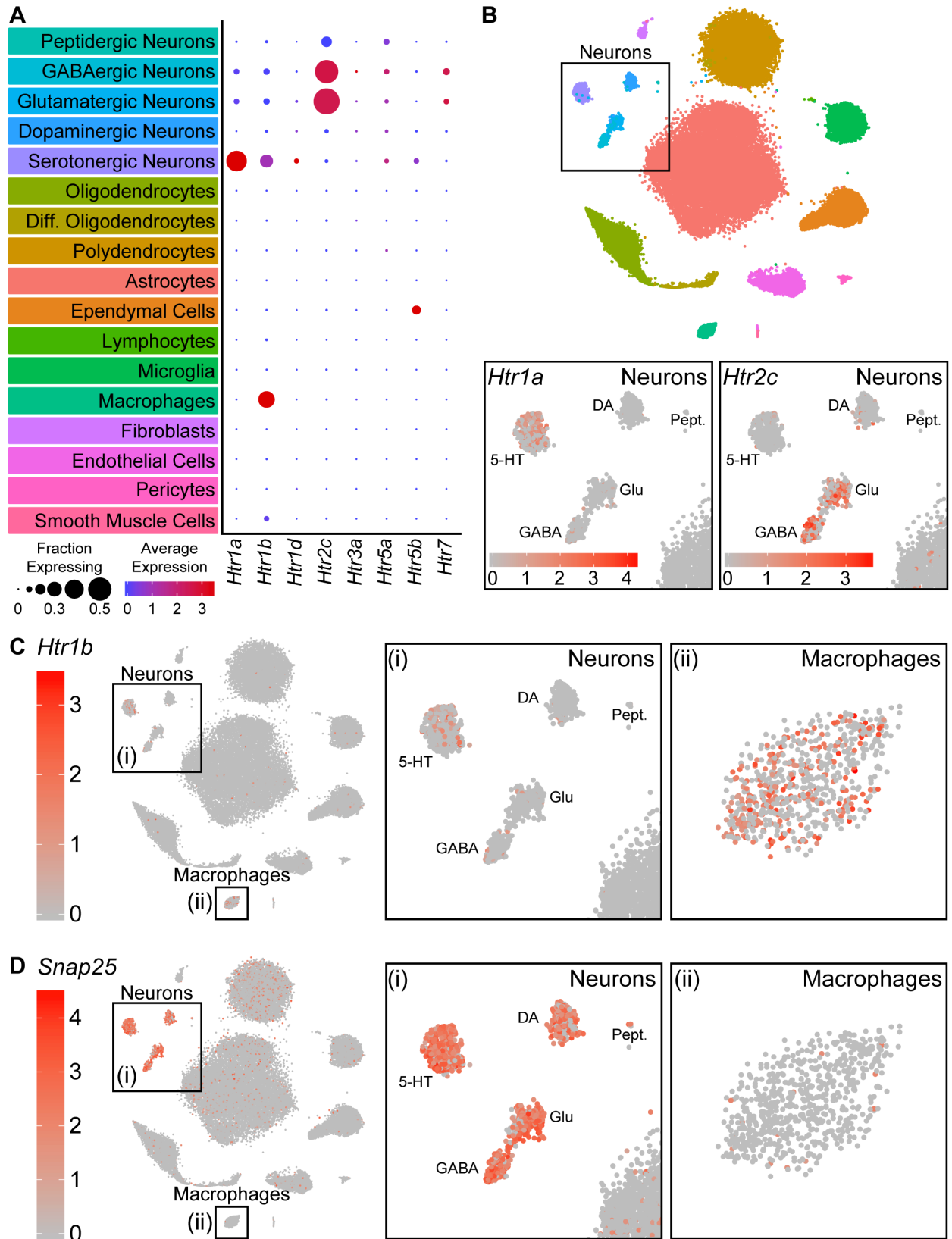
Serotonin receptor expression in neuronal and non-neuronal cell types

Analysis of single cell transcriptomic data allowed us to infer signaling between cell types based on expression of receptors and known ligands. As 5-HT can be released somatodendritically and from 5-HT axon terminals in the DRN (Colgan et al., 2012; de Kock et al., 2006; Kaushalya et al., 2008), we examined the expression patterns of 5-HT receptors in the dataset to infer local 5-HT signaling. Transcripts encoding 8 of the 15 5-HT receptors in the mouse genome were detected in our dataset (Figure 2.4A). Of these *Htr1a*, *Htr1b*, *Htr2c*, *Htr5b*, and *Htr7* were strongly expressed in different subsets of cells. The autoinhibitory G_i-coupled receptor *Htr1a* was expressed primarily in 5-HT neurons, whereas the G_q-coupled *Htr2c* receptor was expressed in both GABAergic and glutamatergic neurons (Figure 2.4B). Additionally, we unexpectedly observed expression of the G_i-coupled *Htr1b* receptor in both 5-HT neurons and pvMΦs of the DRN (Figure 2.4C). Examination of *Htr1b* expression in cortex, striatum, and ventral midbrain suggests that expression of this receptor in pvMΦs is unique to the DRN and its close surroundings (Hrvatin et al., 2018; Saunders et al., 2018; Zeisel et al., 2018). Additionally, the absence of abundant neuronal marker genes (e.g. *Snap25*) in pvMΦs indicates that the presence of *Htr1b* transcripts was unlikely to be a result of engulfment of neuronal debris containing mRNA (Figure 2.4D). *Htr5b*, which is a pseudogene in humans (Grailhe et al., 2001), was found in ependymal cells and a subset of 5-HT neurons. The G_s-coupled *Htr7* receptor was also found in a small subset of GABAergic and glutamatergic neurons.

Figure 2.4: Serotonin receptors are expressed in both neurons and non-neuronal cells.

(A) Dot plots showing expression of the serotonin receptors present in the scRNA-seq dataset in each major cell class. *Htr1a* is expressed specifically in 5-HT neurons, whereas *Htr1b* is expressed in both 5-HT neurons and perivascular macrophages. *Htr2c* is expressed in both GABAergic and glutamatergic neurons. *Htr5b* is expressed in ependymal cells and a subset of 5-HT neurons. *Htr7* is expressed in subsets of GABAergic and glutamatergic neurons. The remaining 5-HT receptors were detected at low levels. **(B)** t-SNE plots with the region containing neuronal clusters enlarged to show expression of *Htr1a* (bottom, left) or *Htr2c* (bottom, right) in individual cells. Cells are color-coded by expression of each transcript. Scale bars are in log-normalized UMI-filtered counts for the respective transcripts. **(C)** t-SNE plots with cells color-coded by their expression of *Htr1b*. Regions containing neuronal or perivascular macrophage clusters are enlarged. **(D)** t-SNE plots with cells color-coded by their expression of the neuron-specific transcript *Snap25*. Regions containing neuronal or perivascular macrophage clusters are enlarged. *Snap25* transcripts are abundant in all neuronal clusters but not in perivascular macrophages, suggesting that *Htr1b* transcripts in perivascular macrophages are unlikely to be a result of engulfment of neuronal debris.

Figure 2.4 (Continued)



Molecularly distinct neuronal subtypes in the DRN

To further resolve the neuronal clusters into separate cell types or subtypes, we analyzed the neuronal clusters separately from the full dataset (see Methods). Subclustering conservatively separated the 2,041 neurons into 18 distinct clusters, which we aggregated into 5 major groups based on similarities in their expression of genes, most notably those involved in the synthesis and release of different neurotransmitters (Figure 2.5A). These groups corresponded to the 5 major neuronal classes that were identified from clustering the full dataset, suggesting that neurotransmitter usage is a primary attribute for neuronal cell type identification. However, we also noted significant overlaps in the expression of genes whose loci are typically exploited for the generation of cell type-specific driver lines (Figure 2.5B, Figure 2.6). These genes included *Gad1* and *Gad2*, which encode GABA synthetic enzymes and are expressed in GABAergic neurons and a subset of both 5-HT and glutamatergic DRN neurons, as well as *Slc17a6*, which encodes a vesicular glutamate transporter and is expressed in most DRN glutamatergic and DA neurons. These overlaps in expression of “canonical” marker genes are consistent with the release of multiple neurotransmitters by individual neurons, especially by monoaminergic neurons (Granger et al., 2017).

All of the major neuronal cell classes, with the exception of the peptidergic neurons, were comprised of several subclusters that each represent a distinct neuron subtype (Figure 2.5B); we found 5 5-HT neuron subtypes, 3 DA neuron subtypes, 5 glutamatergic neuron subtypes, 3 GABAergic neuron subtypes, and 1 cluster co-expressing markers for both GABAergic and glutamatergic neurotransmission (GABA/Glu cluster). To validate the existence of these mixed GABAergic/glutamatergic neurons, we performed multiplexed fluorescent *in situ* hybridization

(FISH) for *Slc32a1* and *Slc17a6* as well as *Crhbp*, which was predicted to be strongly expressed by this cluster (Figure 2.5C). Cells co-expressing the 3 transcripts were found within the caudal-linear nucleus (CLi) and dorsal regions of the anterior DRN. Thus, this cluster, representing just 0.08% (32 of 39,411) of cells in the scRNA-seq dataset, corresponds to a bona fide and previously unrecognized neuronal cell type within the DRN that may be a caudal extension of the recently described GABA/Glu neuron group of the ventral midbrain (Root et al., 2018).

GABAergic and glutamatergic neurons shared the most similarities despite differences in neurotransmitter usage. We found that many subtypes of both GABAergic and glutamatergic neurons shared expression of genes that are enriched in the ventrolateral periaqueductal gray such as *Penk*, as well as the *Htr2c* receptor as described earlier. Within each major group, GABAergic and glutamatergic subtypes differed in their expression of a wide variety of genes that included those for many transcription factors, such as *Nkx2.2*, *Vsx2*, and *Satb1*, as well as peptides and transporters. Additionally, we found a glutamatergic neuron subtype that expressed the vesicular glutamate transporter *Slc17a8* (VGluT3), in contrast to all other DRN glutamatergic neuron subtypes that expressed *Slc17a6* (VGluT2). Consistent with previous descriptions, the *Slc17a8*-expressing glutamatergic subtype also expressed low levels of the transcription factor *Fev* (also known as *Pet1*) similar to 5-HT neurons, despite lacking genes required for the synthesis and release of 5-HT such as *Slc6a4* and *Tph2* (Haugas et al., 2016; Hioki et al., 2010).

Figure 2.5: Neuron subtypes can be distinguished transcriptionally.

(A) t-SNE plot of 2,041 neurons. The main neuron types were defined by the expression of genes necessary to make or release specific neurotransmitters or neuropeptides, and are highlighted by the shaded regions. Several subtypes of each class of neuron, designated by the cell color, can be contained in each shaded region. Color codes for subtype identities correspond to column headers in **(B)**. The cluster outlined in red corresponds to cells expressing both glutamatergic and GABAergic markers. **(B)** Heatmap showing the cluster average Z-scored expression of selected genes that are enriched in each neuron subtype. Genes used to identify major neuronal cell types by their neurotransmitters are labeled in red. **(C)** Fluorescent *in situ* hybridization validating the existence of cells expressing both GABAergic and glutamatergic markers. Cells expressing *Slc32a1*, *Slc17a6*, and *Crhbp* were found in anterior regions of the DRN in the caudal linear nucleus (CLi) and dorsomedial DRN in close proximity to the cerebral aqueduct. The regions indicated by the yellow boxes are shown enlarged on the right.

Figure 2.5 (Continued)

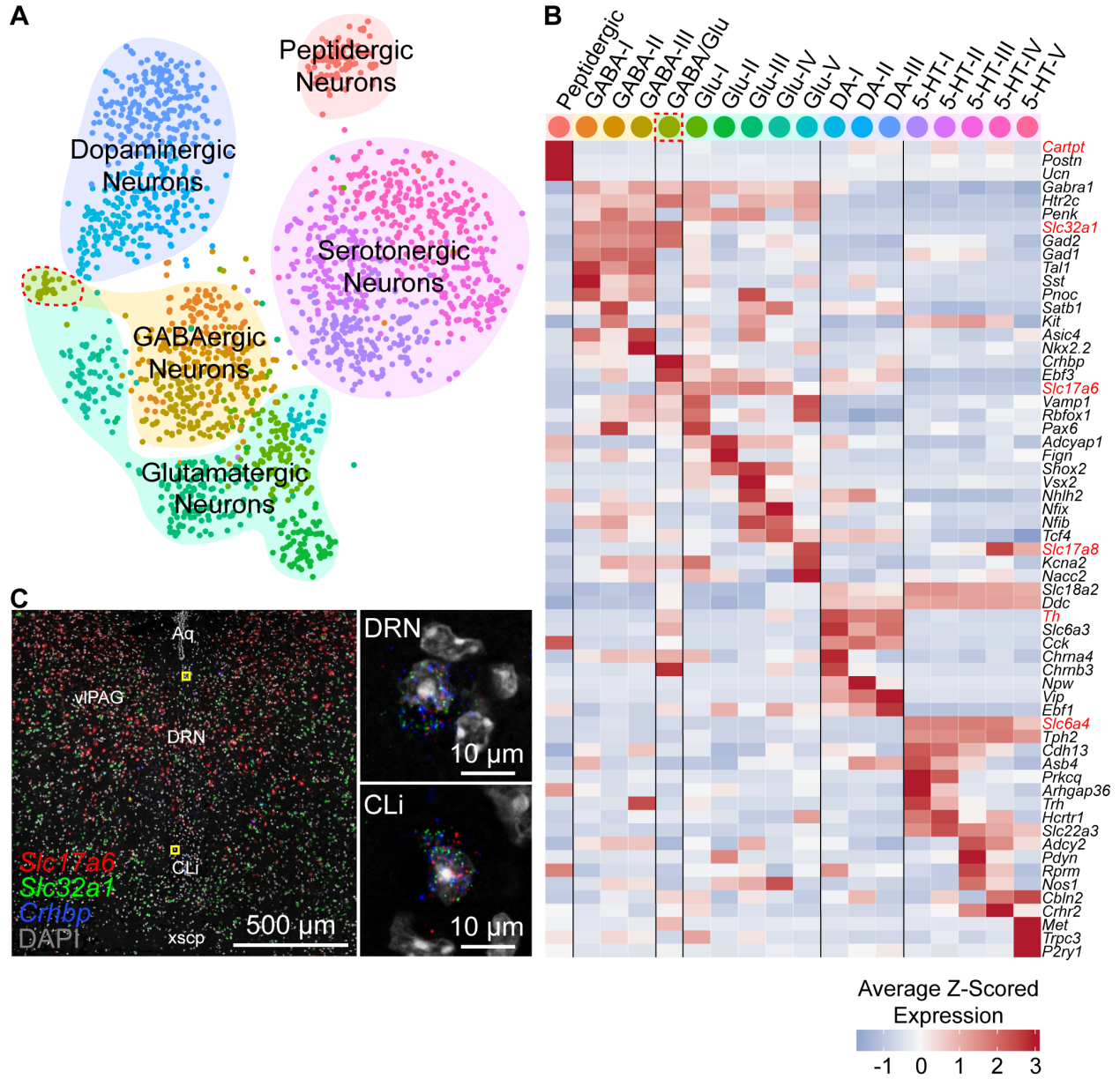
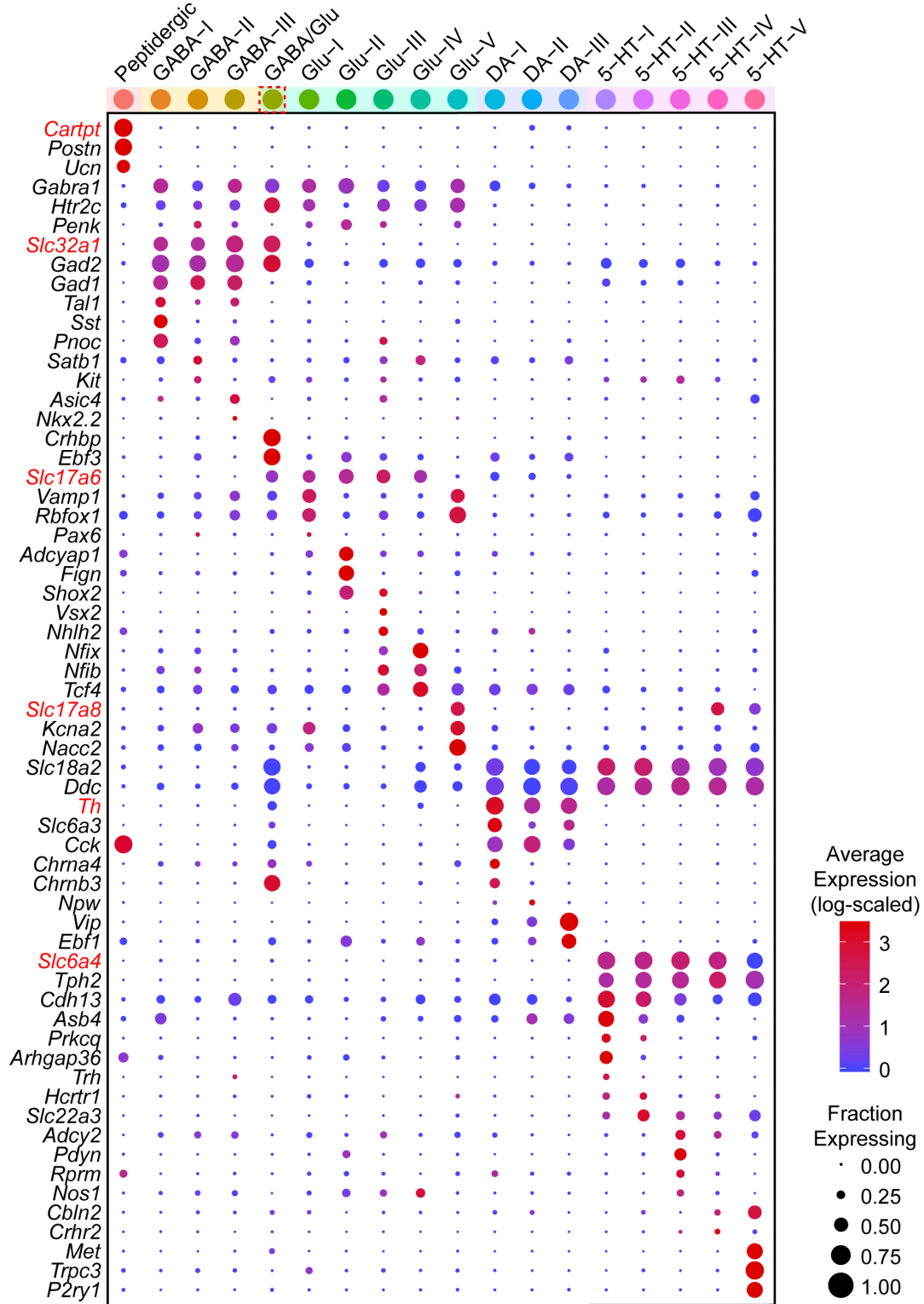


Figure 2.6: Average log-scaled expression of genes differentially expressed between neuron subtypes.

Dot plot showing the log-scaled expression for each gene shown in Figure 2.5B. The color of each dot represents the average log-transformed UMI counts for each gene after normalizing for the total transcript count per cell, while the size of the dot represents the fraction of cells in each neuron subtype cluster in which transcripts for that gene were detected.

Figure 2.6 (Continued)



Monoaminergic neurons were well separated into distinct DA and 5-HT classes. Although *Vip* was found in all 3 DA neuron subtypes, as previously reported for DRN and CLi DA neurons (Dougalis et al., 2012; Poulin et al., 2018; Poulin et al., 2014), *Vip* expression varied between the 3 subtypes. The *Vip*^{low} DA-I subtype showed more similarities in gene expression with the GABA/Glu neurons of CLi as compared to the *Vip*^{high} DA-III subtype, indicating a corresponding topographical organization of these DA neuron subtypes along the anterior-posterior axis from the CLi to DRN. *Vip*^{low} DA-I subtype neurons also expressed nicotinic receptors including *Chrna4* and *Chrb3* that are also found in GABA/Glu neurons, suggesting differences in nicotinic cholinergic activation of these DA neuron subtypes along the anterior-posterior axis and between DA neurons in CLi versus DRN. The DRN DA neurons lacking expression of nicotinic receptors separated into 2 subtypes, DA-II and DA-III, that differed in expression of genes related to neurotransmission including peptides, such as *Npw*, and the vesicular glutamate transporter *Slc17a6*, suggesting that DRN DA neurons are functionally heterogeneous.

Genes differentially expressed between DRN 5-HT neuron subtypes

DRN 5-HT neurons ($n = 704$ cells) separated into 5 distinct subtypes. We constructed a cluster dendrogram using the averaged cluster gene expression to examine the molecular differences between these subtypes (Figure 2.7A, Figure 2.8). We found 333 differentially expressed genes (DE genes) by performing differential expression tests at each node on the cluster dendrogram at a 5% false discovery rate (Benjamini-Hochberg correction). Enrichment tests for gene ontology (GO) terms and analysis of DE genes with annotated functions showed that genes involved in neuronal development and identity specification, such as transcription factors, and genes

involved in specifying neuronal connectivity, such as cell adhesion and axon guidance molecules, were overrepresented in the transcripts differentiating the 5-HT subtypes (Figure 2.9). A large proportion of DE genes encoded for membrane proteins (GO:0016020 – membrane, 193 of 333 DE genes) with functions in neurotransmission and regulating intrinsic cellular excitability, such as neurotransmitter receptors, ion channels, vesicular transporters, neuropeptides, and other proteins involved in the synthesis or reuptake of neurotransmitters (Figure 2.7A).

The cluster dendrogram for 5-HT neuron subtypes showed that the smallest subtype cluster 5-HT-V ($n = 7$ cells) was the most transcriptionally distinct, was marked by expression of genes such as *Met*, *P2ry1*, and *Trpc3* (Figure 2.10C), and lacked expression of genes for GABA co-transmission. Inspection of *ISHs* probing these genes suggests that 5-HT-V subtype neurons are located in the posterior B6 tail of the DRN (Figure 2.7B).

The remaining 4 subtypes separated into 2 groups: the first was comprised of subtypes 5-HT-I ($n = 178$ cells) and 5-HT-II ($n = 186$ cells) that had enriched expression of genes for GABAergic neurotransmission such as *Gad1* and *Slc6a1*, and the calcium-independent protein kinase *Prkcq*. The second group was comprised of subtypes 5-HT-III ($n = 125$ cells) and 5-HT-IV ($n = 208$ cells) that were enriched in genes such as *Adcy2*, which was not expressed in the 5-HT-I/II group. The 5-HT-III/IV group also expressed different cell adhesion and axon guidance molecules from the 5-HT-I/II group, suggesting differences in both cell location and axonal projections between them. However, the expression of several genes in 5-HT-III appeared to be intermediate between 5-HT-I/II and 5-HT-IV – while the 5-HT-III/IV group showed reduced

expression of genes for GABAergic neurotransmission relative to subtypes 5-HT-I/II, several genes that were enriched in 5-HT-III over 5-HT-IV were also expressed in subtypes 5-HT-I or 5-HT-II, including *Pax5*, *Nxph4*, *Gad1*, and *Gad2*. Although the 5-HT-III/IV group expressed genes for glutamatergic transmission, subtype 5-HT-IV expressed higher levels of the vesicular glutamate transporter *Slc17a8* compared to 5-HT-III. 5-HT-III was also enriched in several genes such as *Pdyn*, *Ret*, *Plxna4*, and *Hrh3* compared to the other subtypes. The features shared between 5-HT-III, with both 5-HT-IV and the 5-HT-I/II group are suggestive of gradients in gene expression along orthogonal anatomical axes on which the subtypes are differentially distributed.

ISHs for genes enriched in these 4 subtypes revealed expression patterns that were consistent with the hypothesis that the two groups 5-HT-I/II and 5-HT-III/IV largely separated along the medial-lateral axis, with the added separation of 5-HT-IV from the other 3 subtypes along the dorsal-ventral axis. Genes enriched in subtypes 5-HT-I and 5-HT-II were expressed in lateral parts of the DRN (Figure 2.7C-D), whereas genes enriched in subtypes 5-HT-III and 5-HT-IV showed enrichment in medial parts of the DRN along the midline (Figure 2.7E-F). Additionally, the genes that were differentially expressed between subtypes 5-HT-III and 5-HT-IV showed graded expression along the dorsal-ventral axis along the midline. Multiplexed fluorescent *ISH* (*FISH*) further validated the differential expression of several subtype-enriched genes between 5-HT neurons in different spatial subregions of the DRN (Figure 2.7G-I, Figure 2.10).

Figure 2.7: Characterization of genes differentially expressed between serotonergic neuron subtypes.

(A) Z-scored expression heatmaps of selected genes with functional annotations that are differentially expressed between DRN 5-HT neuron subtypes. A total of 333 differentially expressed (DE) genes were found (5% false discovery rate, Benjamini-Hochberg correction). A large proportion of DE genes encode for cell surface and transmembrane proteins. Genes shown are categorized into five groups: transcription factors, cell adhesion and axon guidance molecules, transmembrane receptors, ion channels, and neurotransmission-related genes. (B-F) *In situ* hybridizations from the Allen Brain Atlas showing the expression patterns of selected DE genes enriched in each of the five 5-HT neuron subtypes. Many DE genes are not expressed uniformly throughout the DRN and are instead spatially heterogeneous along the anterior-posterior, medial-lateral, and dorsal-ventral axes, suggesting that 5-HT neuron subtypes are differentially distributed across spatial domains.

Figure 2.7 (Continued)

(G) Confocal images from a representative DRN coronal section (AP = -4.40 mm) stained for mRNA transcripts of *Trh* (magenta), *Pdyn* (green), and *Slc6a4* (blue) using RNAscope single molecule fluorescent *in situ* hybridization (*FISH*). Regions marked in yellow are enlarged in images (i)-(iii) and show differential expression of *Trh* and *Pdyn* in three DRN subregions. *Trh* and *Pdyn* expression is low in the ventromedial DRN (vmDRN), whereas 5-HT neurons expressing high levels of *Trh* or *Pdyn* can be found in the dorsomedial DRN (dmDRN) and dorsolateral DRN (dlDRN). Cells expressing both *Pdyn* and *Trh* were occasionally observed in the regions bordering dmDRN and dlDRN. **(H)** Proportion of 5-HT neurons (*Slc6a4*⁺) containing *Pdyn* or *Trh* transcripts (minimum of 3 puncta). *Trh* transcripts were detected in a small proportion of *Pdyn*⁺ 5-HT neurons. **(I)** Probability distribution maps of *Slc6a4*⁺ 5-HT neurons containing transcripts for *Pdyn* (green), *Trh* (red), or *Cbln2* (blue) across multiple *FISH* experiments. Cells of each category were separately mapped to a reference atlas and counted in 50 μm x 50 μm bins. Bin counts were normalized to the total cell count for each category to obtain the probability maps that are displayed as heatmaps overlaid on the average coronal Nissl template from the Allen Brain Atlas. *Pdyn*-expressing 5-HT neurons are enriched along the midline, whereas *Trh*-expressing 5-HT neurons are enriched in dorsolateral regions. *Cbln2*-expressing 5-HT neurons are distributed more ventrally, and are also found in the posterior B6 tail of the DRN (panel I7). Positions of *Slc6a4*⁺ cells are not shown. Scale bars: 500 μm , unless otherwise stated.

Figure 2.7 (Continued)

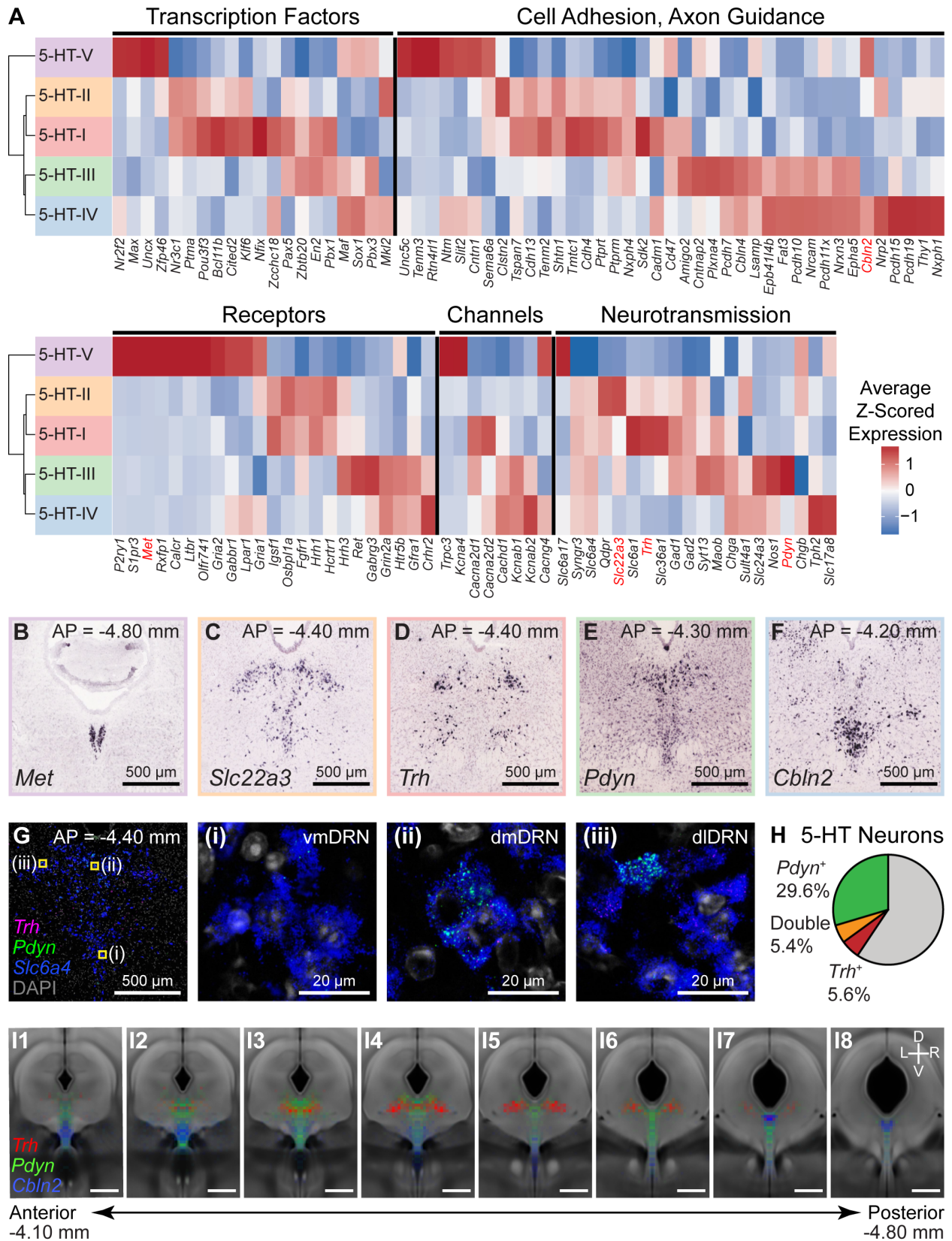


Figure 2.8: Average log-scaled expression of genes differentially expressed between 5-HT neuron subtypes.

Dot plot showing the log-scaled expression for each gene shown in Figure 4A. Genes are sorted into 4 separate dot plots based on their functional grouping. The color of each dot represents the average log-transformed UMI counts for each gene after normalizing for the total transcript count per cell, while the size of the dot represents the fraction of cells in each 5-HT neuron subtype cluster in which transcripts for that gene were detected.

Figure 2.8 (Continued)

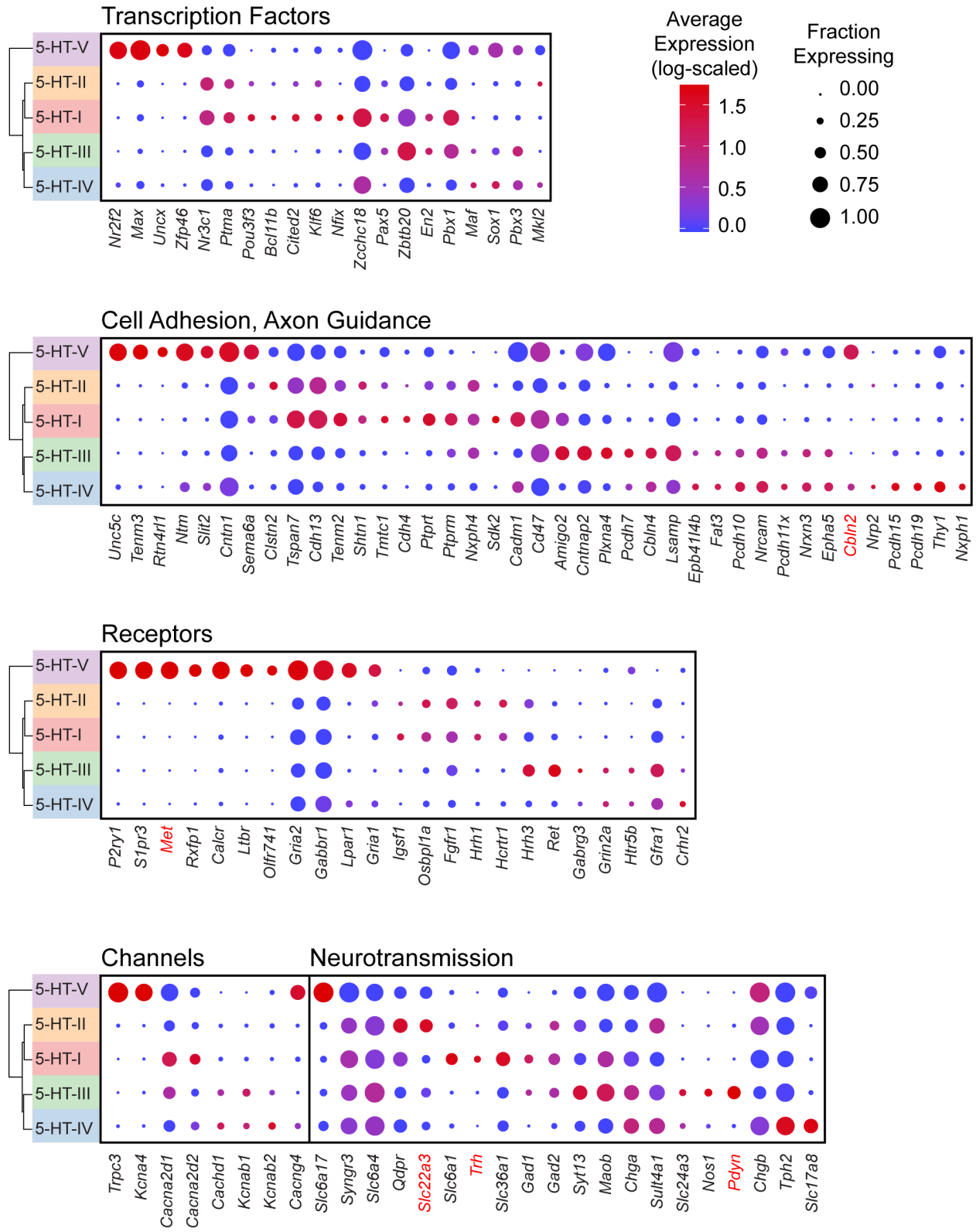


Figure 2.9: Enriched gene ontology terms associated with genes differentially expressed between 5-HT neuron subtypes

Selected gene ontology (GO) terms that were significantly enriched ($Q < 0.05$, Benjamini-Hochberg correction) were sorted by ontology category and arranged in order of increasing Q values. Q values and the proportion of differentially expressed genes associated with each GO term, expressed as a percentage of genes in the background list associated with the GO term, are shown as bar plots. The majority of genes differentially expressed between 5-HT neuron subtypes were membrane proteins (GO:0016020, 193 of 333 genes) that included transporters, cell adhesion molecules, receptors, and synaptic proteins.

Figure 2.9 (Continued)

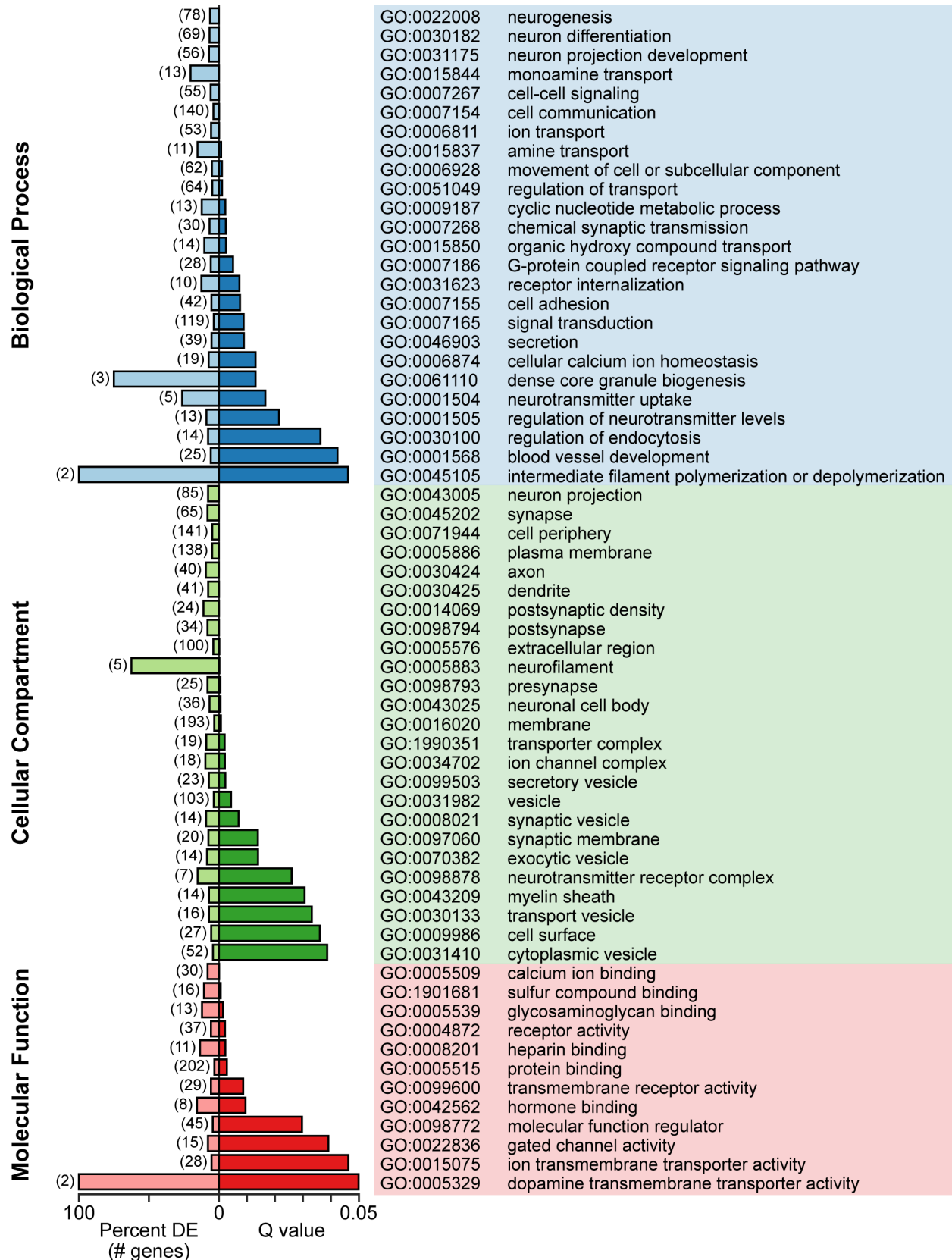
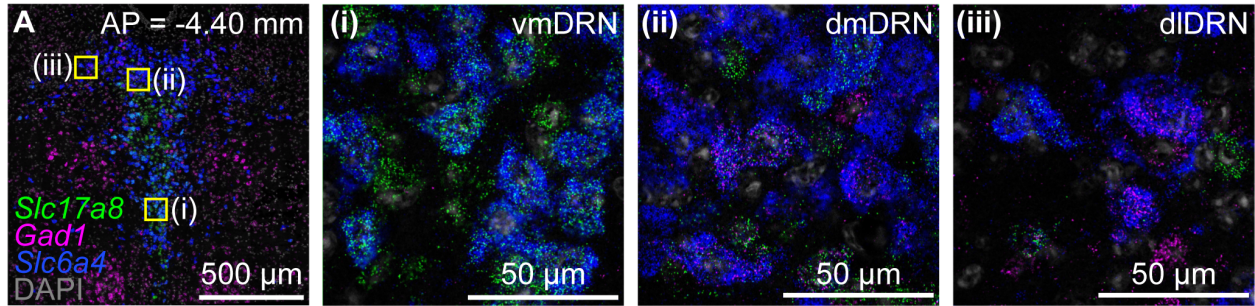


Figure 2.10: Additional validation of differential gene expression between 5-HT neuron subtypes using *FISH*.

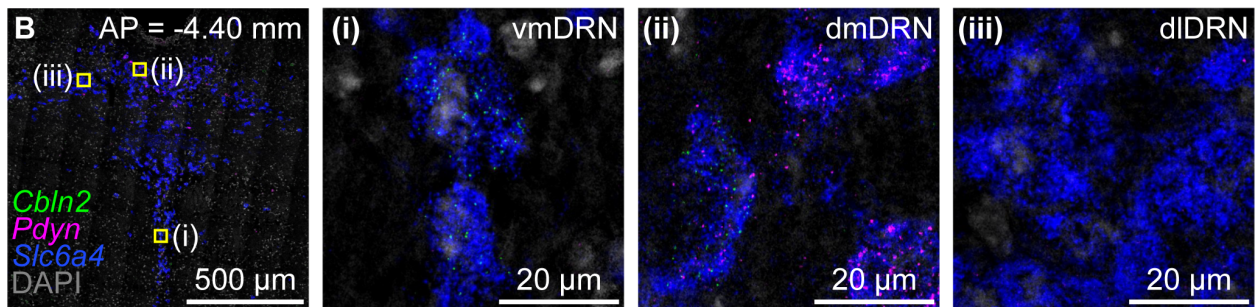
(A-D) Confocal images from representative DRN coronal sections stained for transcripts of interest using multiplexed single molecule *FISH*. All sections were stained for *Slc6a4* (blue) to identify 5-HT neurons, and counterstained using DAPI (gray). For panels A and B, regions outlined in yellow are enlarged in the images on the right labeled (i), (ii), and (iii), which correspond to the ventromedial DRN (vmDRN), dorsomedial DRN (dmDRN), and dorsolateral DRN (dlDRN), respectively. **(A)** 5-HT neurons expressing *Slc17a8* (green) are enriched along the midline in both vmDRN and dmDRN. 5-HT neurons expressing *Gad1* (magenta) were found in dmDRN and dlDRN. **(B)** *Cbln2* (green) is expressed in 5-HT neurons along the midline, but is largely absent from dlDRN. 5-HT neurons expressing both *Cbln2* and *Pdyn* were also found in both vmDRN and dmDRN. 5-HT neurons in dmDRN expressed higher levels of *Pdyn* compared to *Pdyn*⁺ 5-HT neurons in vmDRN. **(C)** Putative 5-HT-V neurons expressing high levels of both *Cbln2* (green) and *Trpc3* (magenta) were found in the posterior B6 subregion of the DRN, which is enlarged in the image on the right. Cells co-expressing *Cbln2* and *Trpc3* also showed reduced staining for *Slc6a4* transcripts compared to 5-HT neurons in other subregions, consistent with reduced expression of *Slc6a4* in the 5-HT-V cluster from the scRNA-seq data. **(D)** Putative 5-HT-I neurons expressing *Trh* (green) are a subset of *Prkcg*⁺ (magenta) 5-HT neurons. *Prkcg*⁺;*Trh*⁻ 5-HT neurons are putative 5-HT-II neurons. **(E)** Spatial distribution of 5-HT neurons from a single *FISH* experiment co-staining for *Cbln2*, *Pdyn*, and *Slc6a4* ($n = 5806$ cells, 3 mice). The locations of 5-HT neurons positive for *Cbln2* only (blue, $n = 1926$ cells), *Pdyn* only (green, $n = 1048$ cells), or double-positive for both transcripts (magenta, $n = 1517$ cells) are displayed as probability heatmaps overlaid on the coronal averaged Nissl template. **(F)** Probability heatmaps from a separate *FISH* experiment co-staining for *Trh*, *Pdyn*, and *Slc6a4* ($n = 6304$ cells, 3 mice). Heatmaps show the spatial distribution of 5-HT neurons positive for *Trh* only (red, $n = 355$ cells), *Pdyn* only (green, $n = 1867$ cells), or double-positive for both transcripts (orange, $n = 339$ cells). Scale bars: 500 μm , unless otherwise stated.

Figure 2.10 (Continued)

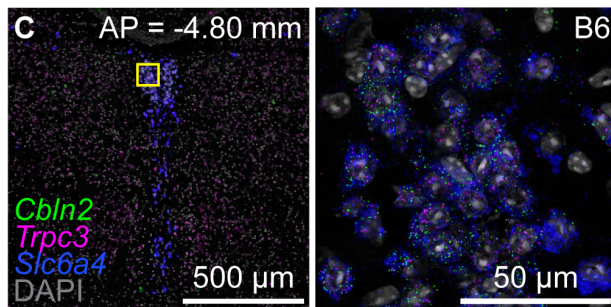
5-HT-I/II vs. 5-HT-III vs. 5-HT-IV



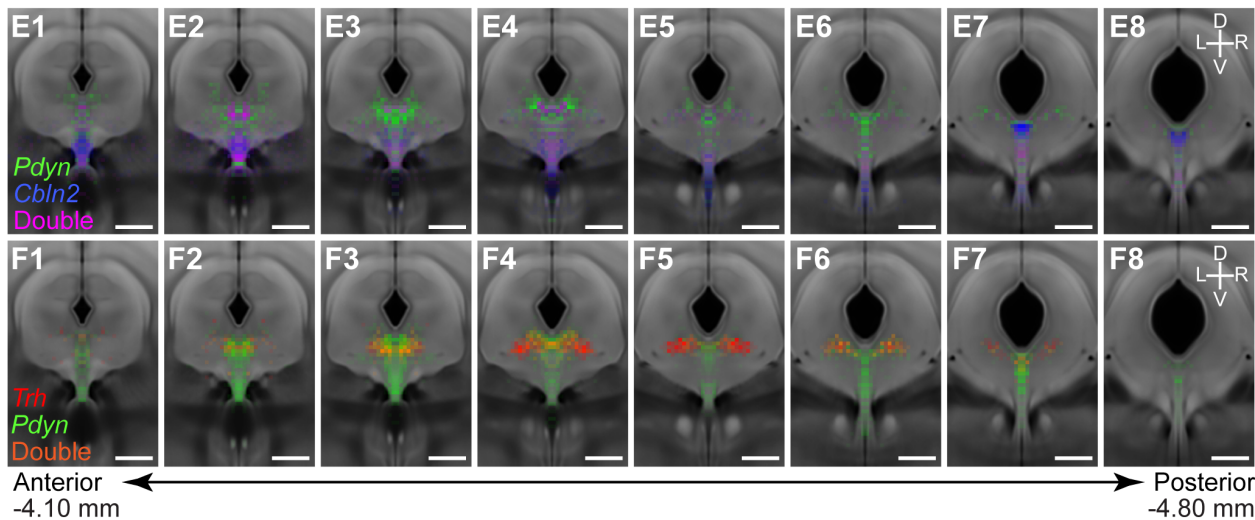
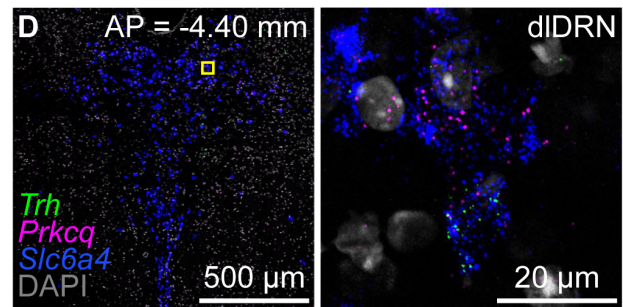
5-HT-III vs. 5-HT-IV



5-HT-V



5-HT-I vs. 5-HT-II



Spatial distribution of 5-HT neuron subtypes in the DRN

Anatomical features are lost during the dissociation of tissue for droplet-based scRNA-seq techniques. *ISH* against a small set of marker genes expressed exclusively in one cell type can be used to localize the putative location of cell types in complex tissue. However, this approach ignores the full information contained in the many dozens or hundreds of genes whose expression differs in a graded manner across different cellular subtypes. In order to exploit information from many genes differentially expressed across 5-HT neuron subtypes to infer the spatial distribution of transcriptionally defined subtypes, we utilized large imaging datasets from the Allen Brain Atlas, which contain the brain-wide spatial expression profiles of nearly every gene. We built a matrix of spatially binned gene expression for DE genes using images of coronal *ISH* spanning the DRN registered to the Allen Brain Atlas Common Coordinate Framework (see Methods, Figure 5–Figure Supplement 1A-B, and Supplementary File 2). We first used the spatial distribution of *Tph2* expression to define spatial bins (voxels) within the Common Coordinate Framework that contain DRN 5-HT neurons. Spatial *ISH* expression data was additionally filtered to retain only spatially variable genes within the region defined by the *Tph2* expression mask (Figure 2.11C). Subsequently, correlation coefficients between the normalized expression scores for 112 DE genes for each of these voxels and each 5-HT neuron subtype cluster were calculated (Figure 2.11D, Figure 2.12). Collections of voxels with high positive correlation coefficients represented the inferred spatial distribution of each subtype within the DRN (Figure 2.13). Missing data in the Allen Brain Atlas dataset as well as artifacts apparently introduced in tissue processing that hampered alignment to the Common Coordinate Framework prevented us from analyzing the full 333 DE genes.

Correlation maps showed that the 5-HT neuron subtypes identified from the scRNA-seq dataset have distinct but overlapping spatial distributions spread along all three major anatomical axes. Most subtypes were not confined to a specific DRN subregion, with the exception of subtype 5-HT-V (Figure 2.13, purple) that showed a tight distribution within the dorsomedial posterior B6 tail of the DRN. The remaining four 5-HT neuron subtypes were found within the larger anterior B7 part of the DRN, and were segregated along both the medial-lateral axis and the dorsal-ventral axis. Subtypes 5-HT-I and 5-HT-II showed the greatest similarities in spatial distribution – both subtypes occupied the dorsolateral subregions in the posterior half of the DRN where they are likely spatially intermingled, consistent with their higher expression of GABAergic transmission genes *Gad1* and *Gad2*. In the more anterior DRN where the lateral wings are absent, subtypes 5-HT-I (Figure 2.13, red) and 5-HT-II (Figure 2.13, orange) were also found within the dorsomedial subregion. This overlaps with the distribution of the *Pdyn*-enriched subtype 5-HT-III (Figure 5, green), which showed the highest correlations with voxels in the dorsomedial part of the DRN in its anterior half. Both subtypes 5-HT-III and 5-HT-IV (Figure 2.13, blue) showed higher correlations with voxels along the midline, but were separated along the dorsal-ventral axis with the *Slc17a8*-enriched 5-HT-IV subtype occupying most of the ventral DRN. Subtype 5-HT-IV was also most evenly distributed along the anterior-posterior axis compared to the other subtypes.

Figure 2.11: Processing of *ISH* images for spatial correlation analysis.

(A) Overview of workflow for processing *ISH* images from the Allen Brain Atlas to generate the spatial expression matrix. Coronal images spanning the DRN in each *ISH* experiment were downsampled and centered on the brain slice. The midline in each slice was identified and the image was rotated to align the midline vertically. Rotated images were cropped and assigned to corresponding positions along the anterior-posterior axis relative to the Allen Brain Atlas coronal template. Cells positive for the *ISH* signal were identified using a spot detection algorithm and counted in 50 x 50 μm bins to generate 2D histograms for each image. 2D histograms, representing the spatial expression profile of the probed gene in a given coronal section, were aligned and cropped along the dorsal-ventral axis to retain only the region containing the DRN (36 X bins x 36 Y bins). Cropped histograms were averaged with the left-right reflection and combined with the other histograms generated from other images in the same experiment image series to generate the volume data (36 X bins x 36 Y bins x 12 images) including *NaN* values for missing data. Volume data for each gene was unrolled into a single row vector (of 15,552 entries), and row vectors were concatenated to generate the spatial expression matrix for spatial correlation analysis.

(B) Sum of 2D histograms generated by the workflow in (A), displayed as a series of 12 coronal sections showing the summed count of cells detected across all *ISH* images analyzed. Anatomical landmarks such as the cerebral aqueduct, fiber tracts, periaqueductal gray, and DRN are easily discerned from the images of the histograms, suggesting that the histograms were well aligned and have good coverage of the DRN.

(C) Scatter plot of the total expression and mean-normalized variance for genes in the spatial expression matrix within the *Tph2*⁺ region. Each dot represents 1 of the 123 genes in the expression matrix. Genes with low spatial variability within the masked region, such as *Tph2* (marked red), and low total expression were excluded from the spatial correlation analysis. *Met*, which showed the most spatial variability since its expression is restricted to the posterior cluster, is also marked on the plot. **(D)** Plot of the number of genes used for the spatial correlation analysis at each of the 12 coronal sections (genes per 2D histogram). Genes with missing data (i.e. no image or damaged slice) were not included in the count.

Figure 2.11 (Continued)

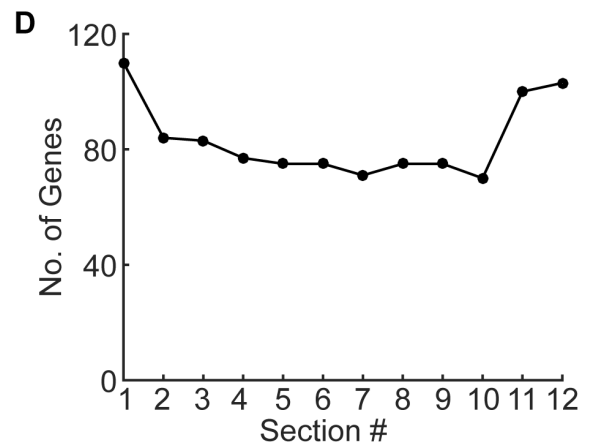
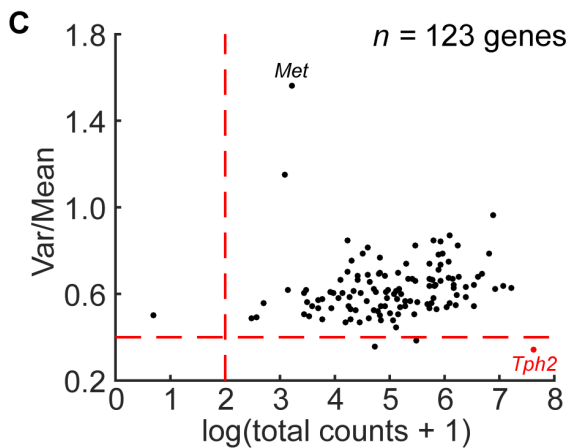
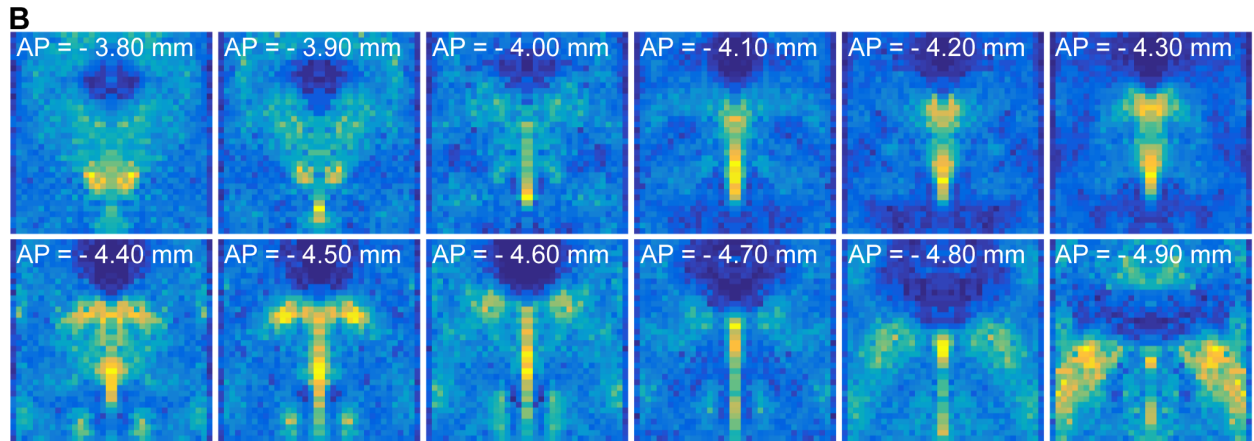
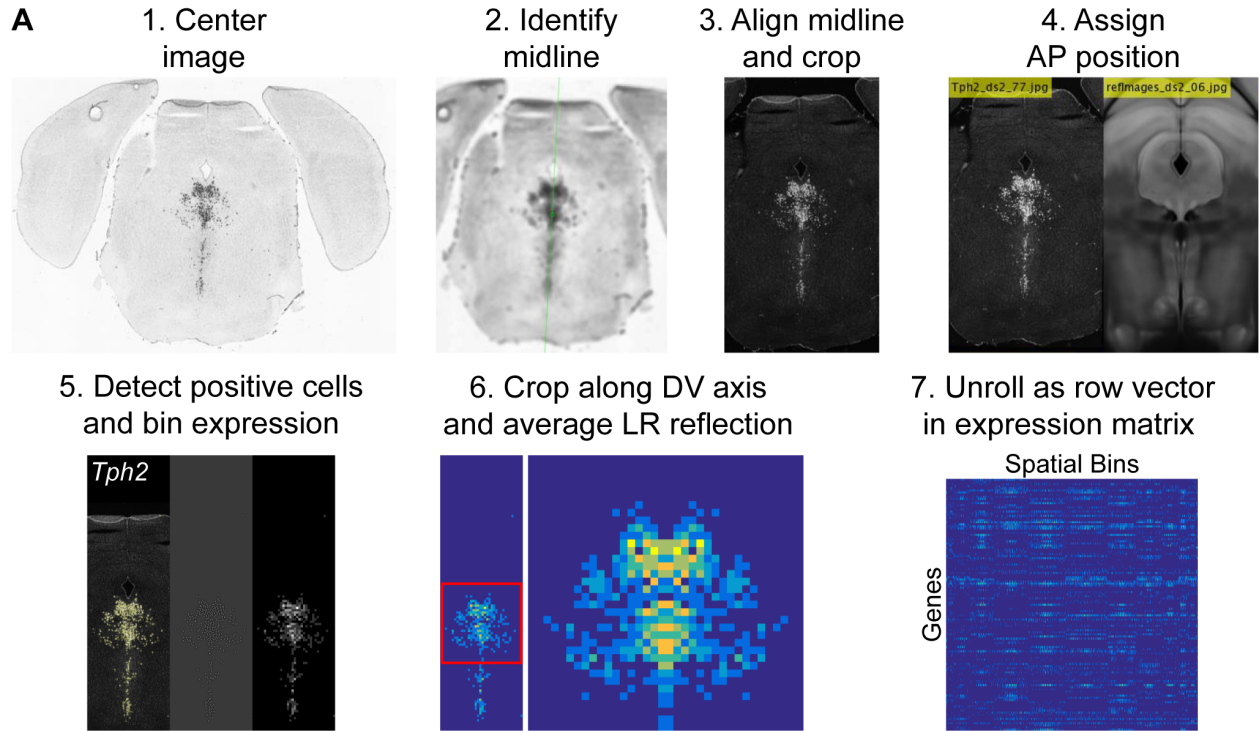


Figure 2.12: Correlation coefficient maps for DRN 5-HT neuron subtypes.

Spatial correlation maps displayed as heatmaps arranged in columns for each 5-HT neuron subtype. Heatmaps correspond to coronal sections, and are arranged vertically in order along the anterior-posterior axis. The averaged *Tph2 ISH* signal is included in the left-most column as a reference for the DRN outline. Anatomical landmarks visible in the averaged Nissl template, such as the cerebral aqueduct and fiber tracts, are outlined and overlaid on each coronal image. Spatial bins in the heatmaps with positive correlations (green) indicate the most likely locations of each 5-HT neuron subtype. Spatial correlation maps have been smoothed using a 2D Gaussian filter (1SD) for visualization. Since only differentially expressed genes were used for this analysis, negative correlations are also seen. These reflect the locations of 5-HT neurons of other subtypes from which, by definition, the differentially expressed genes that define one subtype are excluded. Scale bars: 500 μm .

Figure 2.12 (Continued)

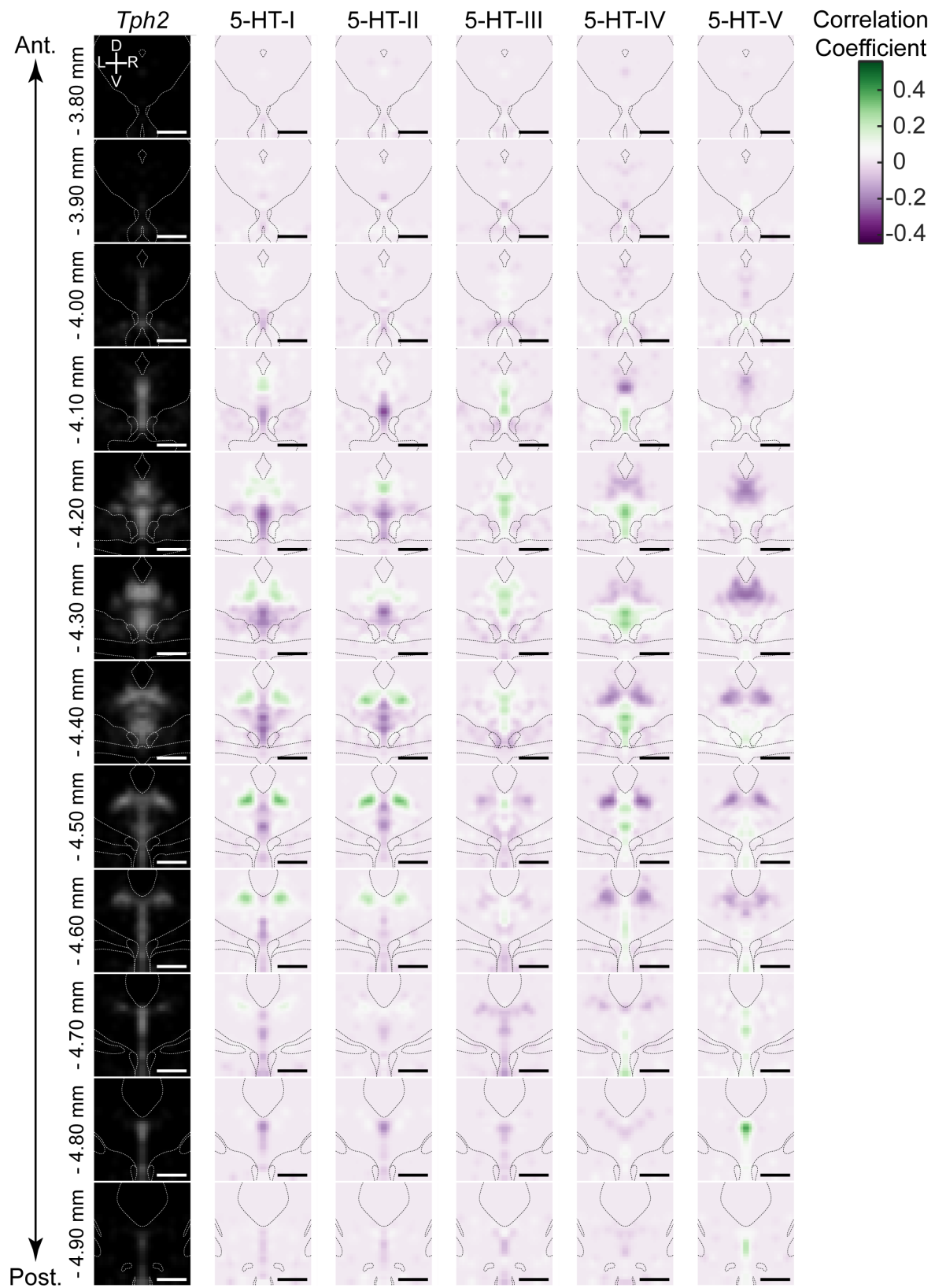
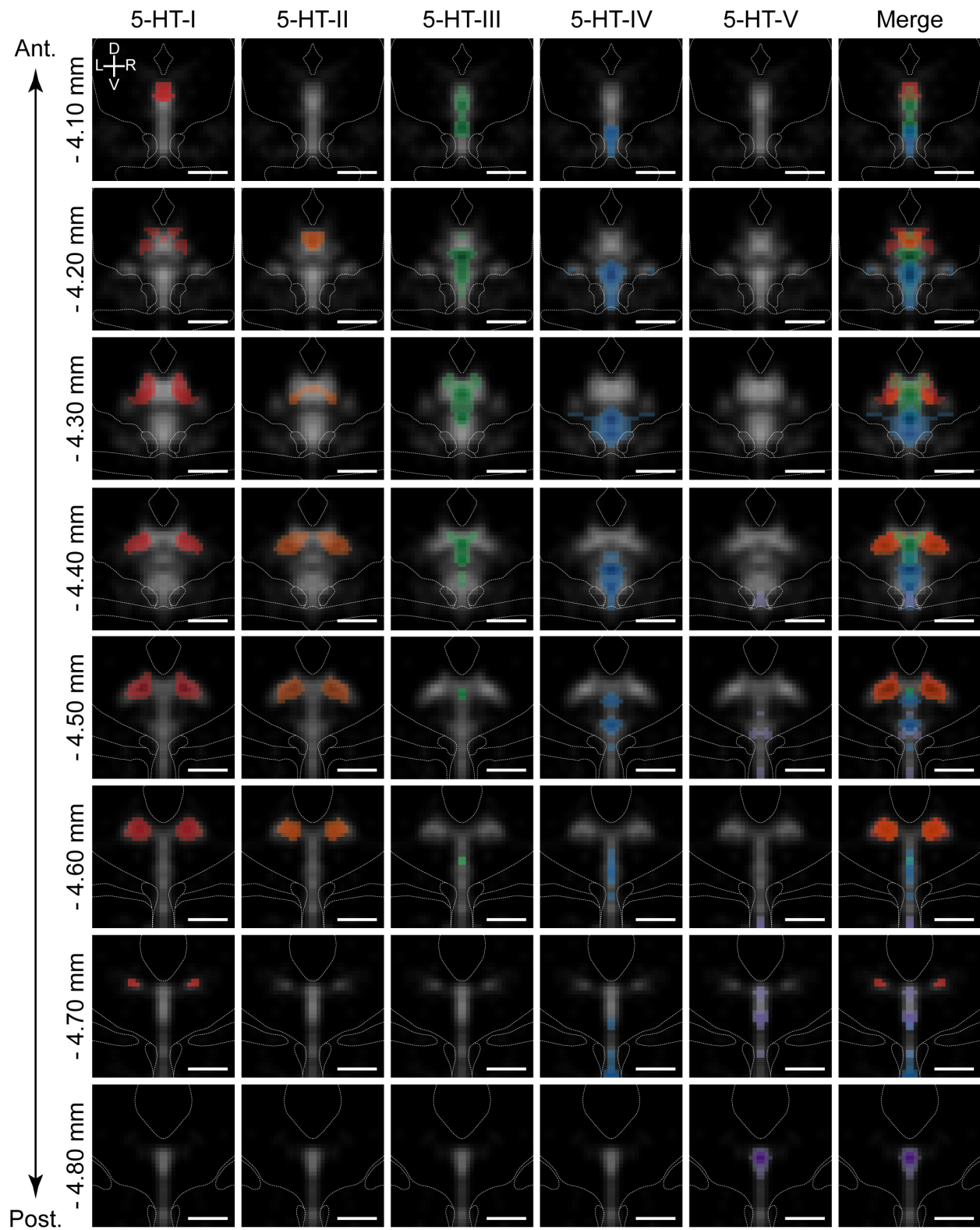


Figure 2.13: 5-HT neuron subtypes are distributed in distinct but overlapping spatial domains.

Inferred spatial distributions of 5-HT neuron subtypes displayed as a map of correlation coefficients between profiles of gene expression of each subtype and each spatial bin. Each column shows the correlation map for each 5-HT neuron subtype at different coronal sections along the anterior-posterior axis of the DRN (rows). Only bins with positive correlation coefficients greater than 0.1 are shown, and maps were smoothed using a 2D Gaussian filter (1SD) for display. Correlation maps are overlaid on the averaged *Tph2* expression (grayscale, based on *ISH* data from the Allen Brain Atlas). Anatomical landmarks visible in the averaged Nissl template, such as the cerebral aqueduct and fiber tracts, are outlined and overlaid on each coronal image. Correlation maps for subtypes 5-HT-I and 5-HT-II suggest that they are largely intermingled in the dorsolateral DRN, with some overlap in the anterior DRN with 5-HT-III in the dorsomedial DRN. 5-HT-IV was enriched in the ventral regions of the DRN, while 5-HT-V was highly restricted to the posterior B6 tail of the DRN that was highly enriched in expression of the 5-HT-V enriched gene *Met*. Scale bars: 500 μ m.

Figure 2.13 (Continued)



5-HT neuron subtype distributions coincide with different projection-defined subpopulations

The nuclei of the basal ganglia are major targets of DRN 5-HT neurons, with approximately one-third of all DRN 5-HT neurons innervating the striatum (Str) (Steinbusch et al., 1981). In addition to the extensive anatomical connectivity between the basal ganglia and DRN, both structures have motor and cognitive functions, and have been implicated in disorders that affect motor control and motivation such as impulsivity, obsessive-compulsive disorder, and major depressive disorder (Di Matteo et al., 2008; Miguez et al., 2014; Pauls et al., 2014; Schilman et al., 2010). Although the DRN has many shared functions with the basal ganglia, DRN neurons are also involved in modulation of sensory pathways, limbic and neuroendocrine systems, and brainstem motor nuclei, and it has been proposed that anatomically segregated subsets of DRN 5-HT neurons form separate efferent pathways to perform these different functions (Hale and Lowry, 2011; Lowry, 2002; Muzerelle et al., 2016; Waselus et al., 2011). Therefore to compare the distribution of the 5-HT neuron subtypes from our scRNA-seq dataset with those of projection-defined neuron subpopulations in the DRN, we performed retrograde tracing from several nuclei of the basal ganglia, structures connected to basal ganglia circuits such as frontal and prefrontal cortical regions, as well as more functionally and anatomically distant structures that include thalamic sensory nuclei, such as the dorsal lateral geniculate nucleus (dLGN).

To map the distribution of projection-defined DRN neuron subpopulations, we performed retrograde tracing using glycoprotein-deleted rabies viruses (RbV) injected into brain regions known to receive inputs from DRN 5-HT neurons (Figure 2.14A). Cells infected via their axons by RbV were fluorescent, and their positions were manually registered onto an averaged Nissl

coronal template from the Allen Brain Atlas (Figure 2.13B-C). Cells were counted in 50 x 50 μm bins, and bin counts were normalized by the total cell count to obtain the probability distributions for each projection-defined subpopulation. Probability distributions are displayed as heatmaps overlaid on reference template images to compare their distributions.

Most projection-defined subpopulations were located either ipsilateral to the injection site or along the midline, with the exception of the habenula-projecting neurons which were found in both ipsilateral and contralateral lateral wings of the DRN (Figure 2.15). Within the cortical-projecting group, frontal- and prefrontal-projecting subpopulations were differentially distributed along the anterior-posterior axis of the DRN – M1-projecting neurons were relatively confined to the anterior half of the DRN, whereas mPFC-projecting neurons were found in both anterior and posterior halves. Consistent with previous reports (Ren et al., 2018; Waterhouse et al., 1986), we found that most subcortical-projecting neurons were located in the dorsal DRN, whereas most cortical-projecting neurons were located in the ventral DRN. Although there was a crude separation of cortical- and subcortical-projecting subpopulations along the dorsal-ventral axis, there were considerable overlaps between their distributions, preventing the delineation of a clear boundary between cortical- and subcortical-projecting groups. The Str-projecting and M1-projecting subpopulations were largely segregated into the dorsal and ventral DRN respectively. However, there were overlaps in their distributions at intermediate levels – both Str-projecting and M1-projecting neurons were found in the ventrolateral DRN (outlined in cyan in Figure 2.14D column 3) and dorsal border of the

Figure 2.14: Projection-defined DRN neuron subpopulations overlap with multiple 5-HT subtypes.

(A) Schematic of retrograde tracing experiments in which unpseudotyped rabies viruses (SADΔG B19 stain) were used to infect and label neurons whose axons innervate the virus-injected target region (GPe in this example). **(B)** Image of a coronal section of the DRN showing rabies-labeled, GPe-projecting neurons. Brains were fixed 7 days post-injection for histology, and 5-HT neurons in the DRN were visualized using immunohistochemistry against TPH2. Sections were counterstained using a fluorescent Nissl stain (Neurotrace). **(C)** The location of all rabies-labeled cells within the DRN and vIPAG, such as the GPe-projecting cells in (B), were manually registered onto a coronal template derived from the averaged Allen Brain Atlas coronal Nissl stain. Labeled neurons outside of this region of interest, such as the PPN and dorsal PAG, were not included. **(D1-5)** Distributions of Str-projecting (green), M1-projecting (blue), and dLGN-projecting (red) subpopulations, displayed as a probability density map (50 μm x 50 μm bins) overlaid on the coronal template. Coronal sections shown are centered in panel D3 at the maximum density of the Str-projecting population. Str- and M1-projecting populations were largely separated along the dorsal-ventral axis, with some overlap. Co-labeled neurons projecting to both Str and M1 were typically found in the ventrolateral DRN, outlined in cyan in D3, and the ventromedial DRN. **(E)** Pairwise correlations between the distributions of projection-defined subpopulations. Correlations between the Str-projecting subpopulation were higher with other subpopulations that also innervate nuclei of the basal ganglia, compared with subpopulations innervating functionally distinct targets such as M1 or dLGN. **(F-G)** Overlap between the distributions of neurons innervating Str (F) or M1 (G) and the 5-HT neuron subtype distributions at AP = -4.30 mm. Distributions of each projection-defined subpopulation are represented as probability maps (magenta) overlaid on the averaged *Tph2* expression. Subtype distributions are represented as color-coded outlines corresponding to the colors used in Figure 4 for each subtype. Str-projecting neurons largely fell into regions occupied by both 5-HT-III and 5-HT-IV subtypes, suggesting molecular heterogeneity within this projection-defined population. M1-projecting neurons were more confined to the ventral DRN, overlapping with the distribution of the 5-HT-IV subtype. Scale bars: 500 μm.

Figure 2.14 (Continued)

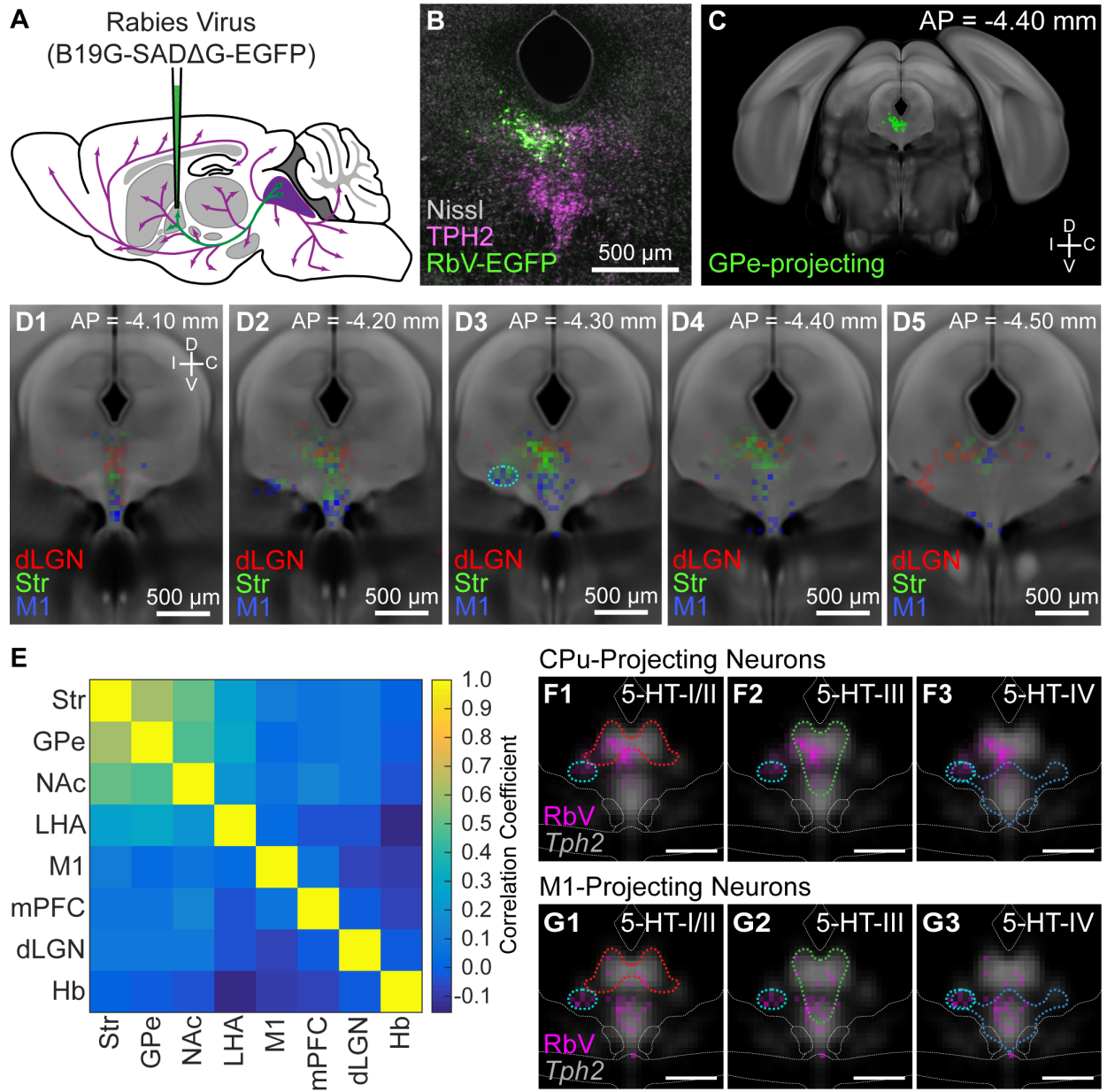
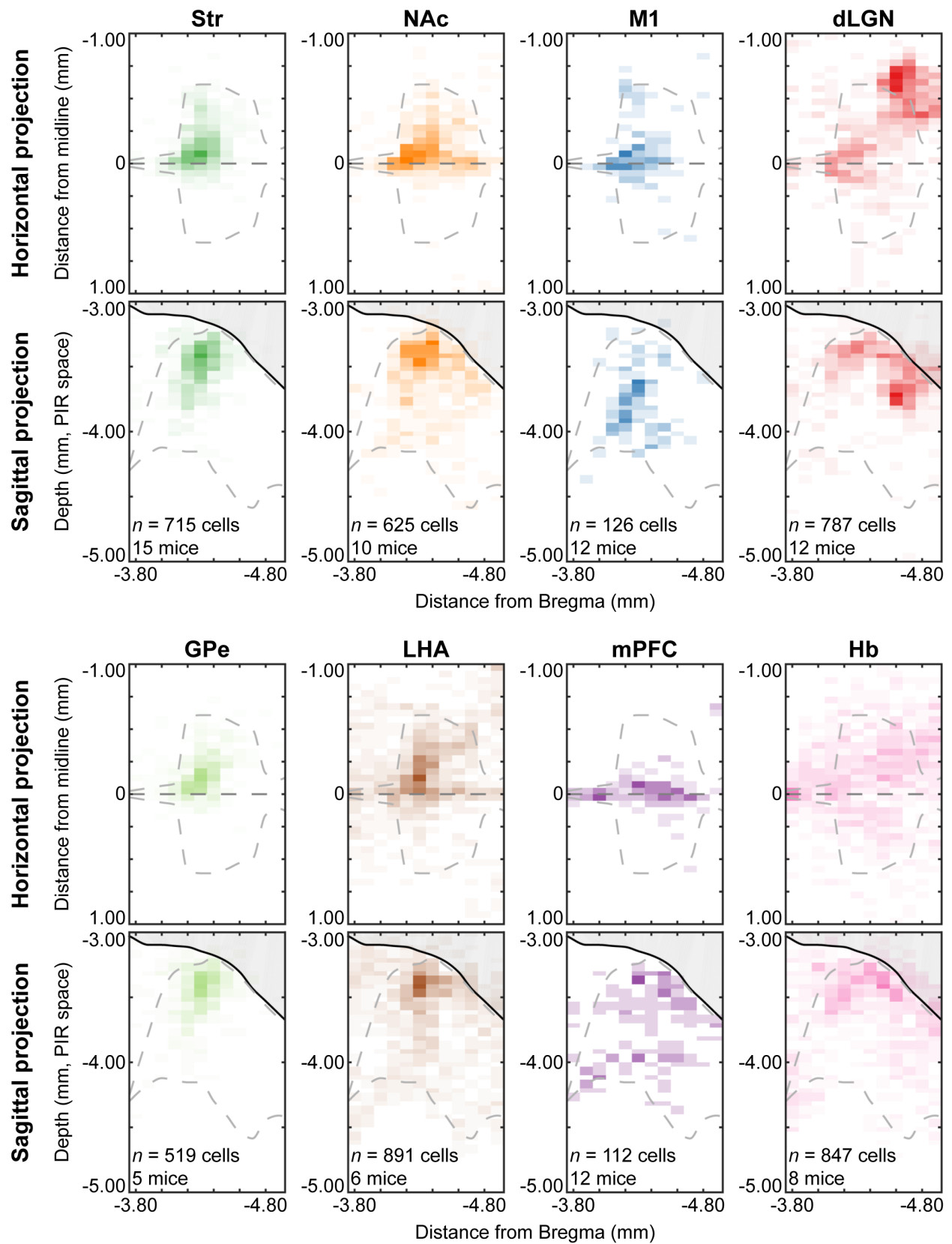


Figure 2.15: Spatial distributions of projection-defined subpopulations.

Distributions of all projection-defined subpopulations in Figure 5 displayed as probability density maps. Distributions for each subpopulation were projected onto either the horizontal or sagittal plane (50 x 100 μm bins). The midline in horizontal projections is indicated by a straight gray line at 0 mm, and distances from the midline are negative for the hemisphere ipsilateral to the injection site. The region occupied by the cerebral aqueduct is shaded in solid gray in sagittal projections, and the depth indicated is relative to the origin of the PIR space in the Allen Brain Atlas. The flattened projection of the region containing *Tph2*⁺ cells is outlined by the gray dashed line in each image. Str-projecting and GPe-projecting subpopulations were the most similar, whereas the Str-projecting and NAc-projecting subpopulations were mostly overlapping in the anterior DRN but differed in the posterior DRN. Cells outside of the ventrolateral periaqueductal gray and DRN, such as cells in the pedunclopontine nucleus or dorsal periaqueductal gray, were excluded from the probability maps. Abbreviations: Str: striatum; GPe: globus pallidus, external; NAc: nucleus accumbens; LHA: lateral hypothalamic area; M1: primary motor cortex; mPFC: medial prefrontal cortex; dLGN: dorsal lateral geniculate nucleus; Hb: habenula.

Figure 2.15 (Continued)



ventromedial DRN. Double retrograde tracing experiments also showed that DRN neurons innervating both Str and M1 were often found in these regions (Figure 2.16).

Projection-defined subpopulations that innervated different subcortical targets, such as the Str-projecting versus dLGN-projecting subpopulations, were spatially segregated within the DRN (Figure 2.14D). dLGN-projecting neurons were mostly located in dorsolateral subregions at more posterior levels, whereas Str-projecting neurons were mostly in the dorsomedial subregion at more anterior levels. The distributions of subpopulations innervating related structures within the basal ganglia were more similar (Figure 2.14E) and, while the subpopulations innervating the external globus pallidus (GPe) and Str were most similar, the subpopulations innervating the Str and nucleus accumbens (NAc, also called the ventral striatum) showed a larger difference. This difference was largely driven by the presence of NAc-projecting neurons in posterior parts of the DRN where mPFC-projecting neurons were also located, whereas Str-projecting DRN neurons were relatively confined to the anterior half of the DRN (Figure 2.17). This is also consistent with differences in the function of Str and NAc and their relation to functional differences between the anterior and posterior DRN (Lowry, 2002; Van Bockstaele et al., 1993).

Differential expression of many axon guidance and cell adhesion molecules between 5-HT neuron subtypes predicts that 5-HT subtypes innervate different brain regions. Two models for how these molecularly-defined subtypes relate to projection-defined subpopulations that would be consistent with this hypothesis are (i) 5-HT neuron subtypes have non-overlapping axonal projection fields and thus a projection-defined subpopulation is comprised of a single subtype

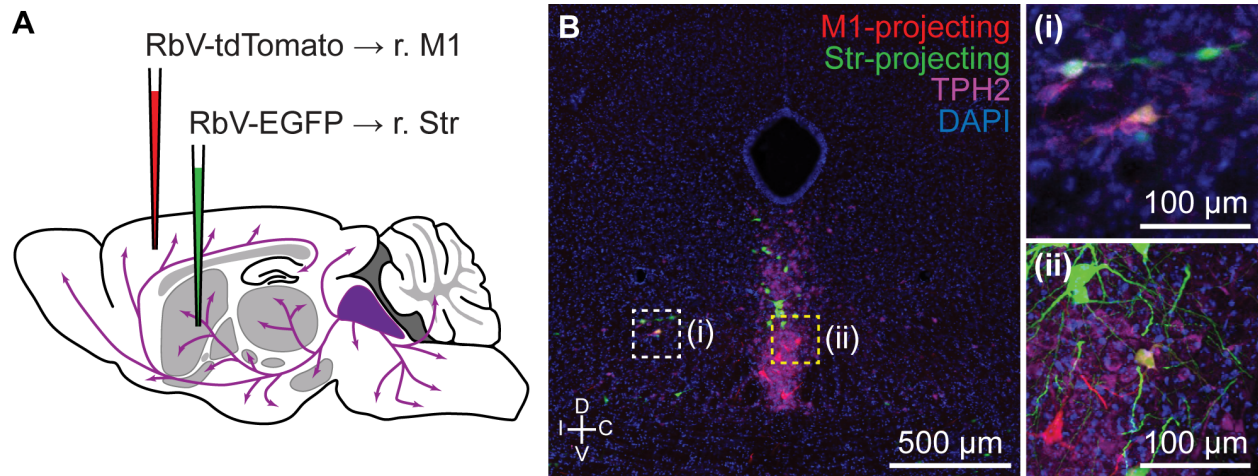


Figure 2.16: Ventrolateral DRN neurons send axon collaterals to both striatum and motor cortex.

(A) Schematic of double retrograde tracing experiment using unpseudotyped rabies viruses. RbV-tdTomato was injected into primary motor cortex, and RbV-EGFP was injected into the ipsilateral striatum. Tissue collection for histology was performed 7 days post-injection. (B) Representative fluorescent image of a coronal section through the anterior DRN containing both M1- and Str-projecting neurons. 5-HT neurons were labeled by an antibody stain for TPH2. Neurons innervating both M1 and Str were co-labeled by RbV-tdTomato and RbV-EGFP, and were typically found in the ventrolateral DRN and the dorsal border of the ventromedial DRN. Inset (i) is a confocal image of the ventrolateral DRN region in (B) marked by the white dashed box, and inset (ii) is a confocal image of the ventromedial DRN region in (B) marked by the yellow dashed box. Both insets are centered on TPH2⁺ cells co-labeled by RbV-tdTomato and RbV-EGFP.

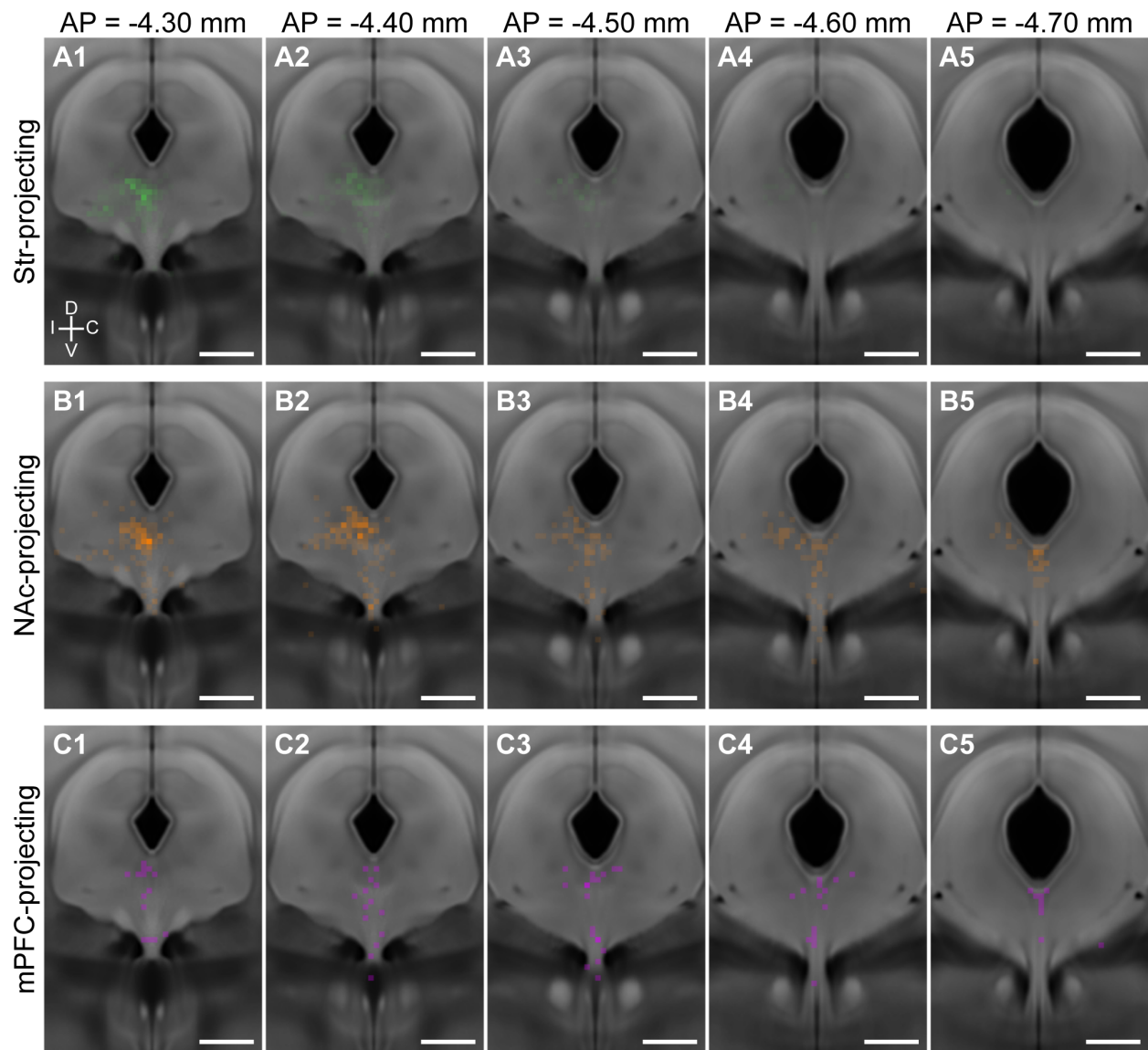


Figure 2.17: Caudal DRN B7 neurons innervate ventral striatum and prefrontal cortex.

Distributions of Str-projecting (A), NAc-projecting (B), and mPFC-projecting (C) neurons displayed as probability density maps overlaid on the Allen Brain Atlas coronal template. Str-projecting and NAc-projecting are both found in the dorsomedial DRN at anterior sections (columns 1 – 2). Str-projecting neurons are more restricted to anterior sections of the DRN, whereas the NAc-projecting neurons are also found in posterior sections of the DRN (columns 3 – 5) where they overlap with the distribution of mPFC-projecting neurons.

and is contained within the subtype's distribution, or (ii) different 5-HT neuron subtypes can innervate the same structure and thus projection-defined subpopulations can be comprised of one or more subtypes. To predict the 5-HT neuron subtypes present in different projection-defined neuron subpopulations, we compared the distributions of projection-defined subpopulations with the inferred 5-HT neuron subtype distributions.

It has been reported that cortical-projecting subpopulations of DRN 5-HT neurons express *Slc17a8*, in agreement with the extensive overlap between the spatial distribution of cortical-projecting neurons and *Slc17a8* expression (Ren et al., 2018). This suggests that cortical-projecting subpopulations should correspond to subtype 5-HT-IV from the scRNA-seq dataset, which is *Slc17a8*-expressing and distributed to the ventral DRN. Additionally, we would predict that the Str-projecting subpopulation corresponds to the subtype 5-HT-III, since their distributions overlap extensively in the dorsomedial DRN. Consistent with our hypothesis that 5-HT neuron subtypes innervate different brain regions, we found that the inferred distributions of each 5-HT neuron subtype coincides with a different set of projection-defined subpopulations – the distribution of subtype 5-HT-III was most similar to the distribution of Str-projecting neurons (Figure 2.14F), whereas the distribution of subtype 5-HT-IV was more similar to that of M1-projecting neurons (Figure 2.14G). However, neither Str-projecting nor M1-projecting subpopulations were fully contained within the distribution of a single 5-HT neuron subtype. Str-projecting neurons in the ventrolateral DRN (marked cyan in Figure 2.14D, F, G), where neurons innervating both Str and M1 are located, fell within the distribution of subtype 5-HT-IV but not of subtype 5-HT-III. This suggests that Str is a target of multiple molecular subtypes of 5-HT

neurons, and supports the model that some structures are innervated by multiple 5-HT neuron subtypes due to overlaps in the axonal projection fields of different subtypes.

Striatal-projecting 5-HT neurons are transcriptionally heterogeneous

To determine the molecular identities of individual projection-defined DRN neurons, we combined RbV-mediated retrograde tracing with multiplexed *FISH* for genes enriched in different 5-HT neuron subtypes. We focused on determining the subtype identity of Str-projecting 5-HT neurons, since their location overlaps with the distributions of multiple 5-HT neuron subtypes. Neurons projecting to Str were labeled using axon-infecting unpseudotyped SADΔG B19 rabies viruses (B19G-SADΔG-tdTomato) injected into the ventrolateral Str. Rabies-infected neurons were identified by expression of the viral transcript *B19N* using *FISH* (RNAscope probe: RABV-gp1), and 5-HT neurons were identified based on expression of the serotonin reuptake transporter gene *Slc6a4* (Figure 2.18). The subtype identity of RbV-infected 5-HT neurons was identified by expression of genes that were highly enriched in each subtype: *Trh* for subtype 5-HT-I, *Pdyn* for subtype 5-HT-III, *Cbln2* and *Slc17a8* for subtype 5-HT-IV. *ISH* for each of these subtype-enriched genes was performed on separate sets of RbV-labeled cells (Figure 2.19).

We found that Str-projecting DRN 5-HT neurons expressed the subtype 5-HT-III enriched gene *Pdyn* (52%, 39 of 75 RbV-labeled 5-HT neurons) or the 5-HT-IV enriched gene *Cbln2* (46%, 49 of 106 RbV-labeled 5-HT neurons), consistent with the overlap in the distribution of this projection-defined subpopulation with the inferred distributions of these two distinct subtypes. A subset of Str-projecting neurons also expressed *Slc17a8* (57%, 70 of 123 RbV-labeled 5-HT

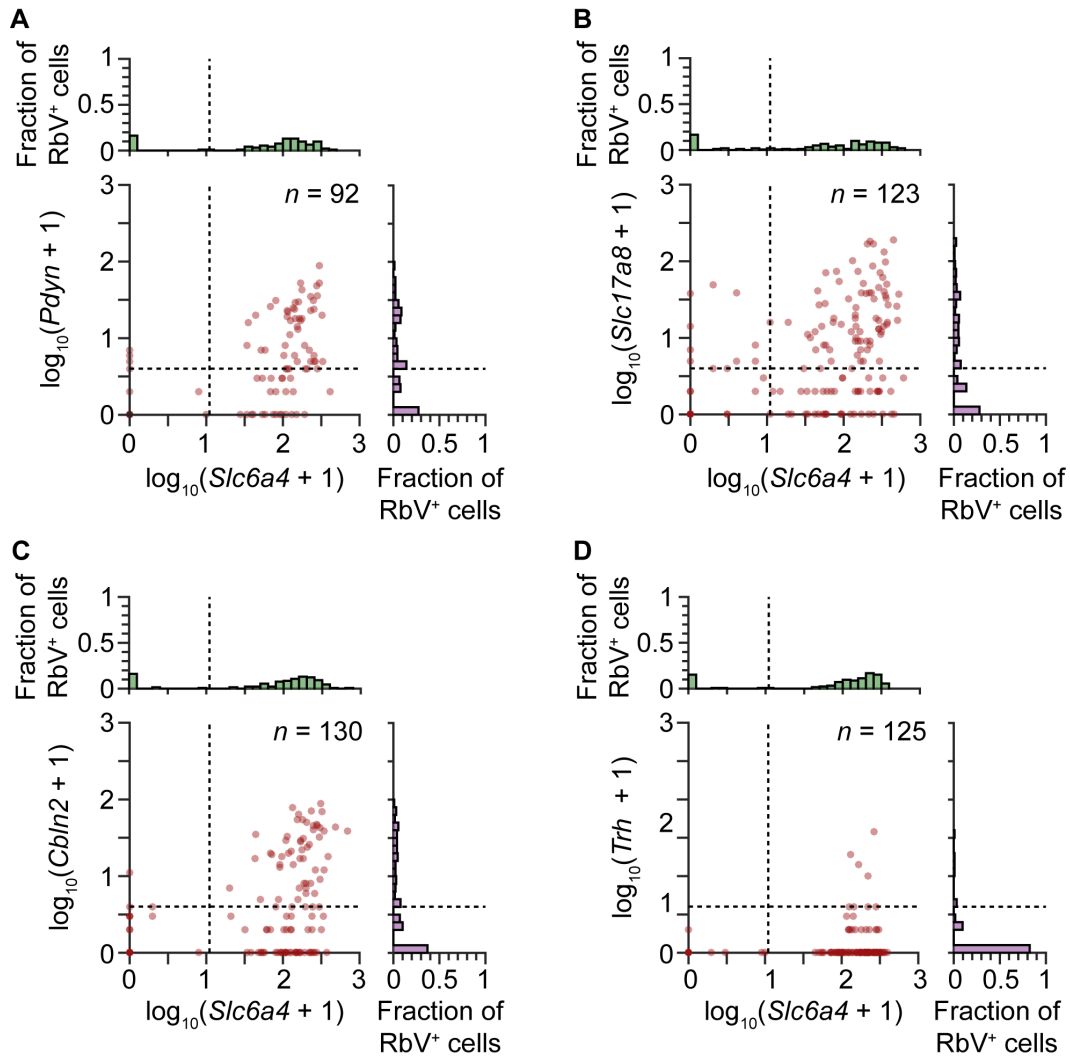


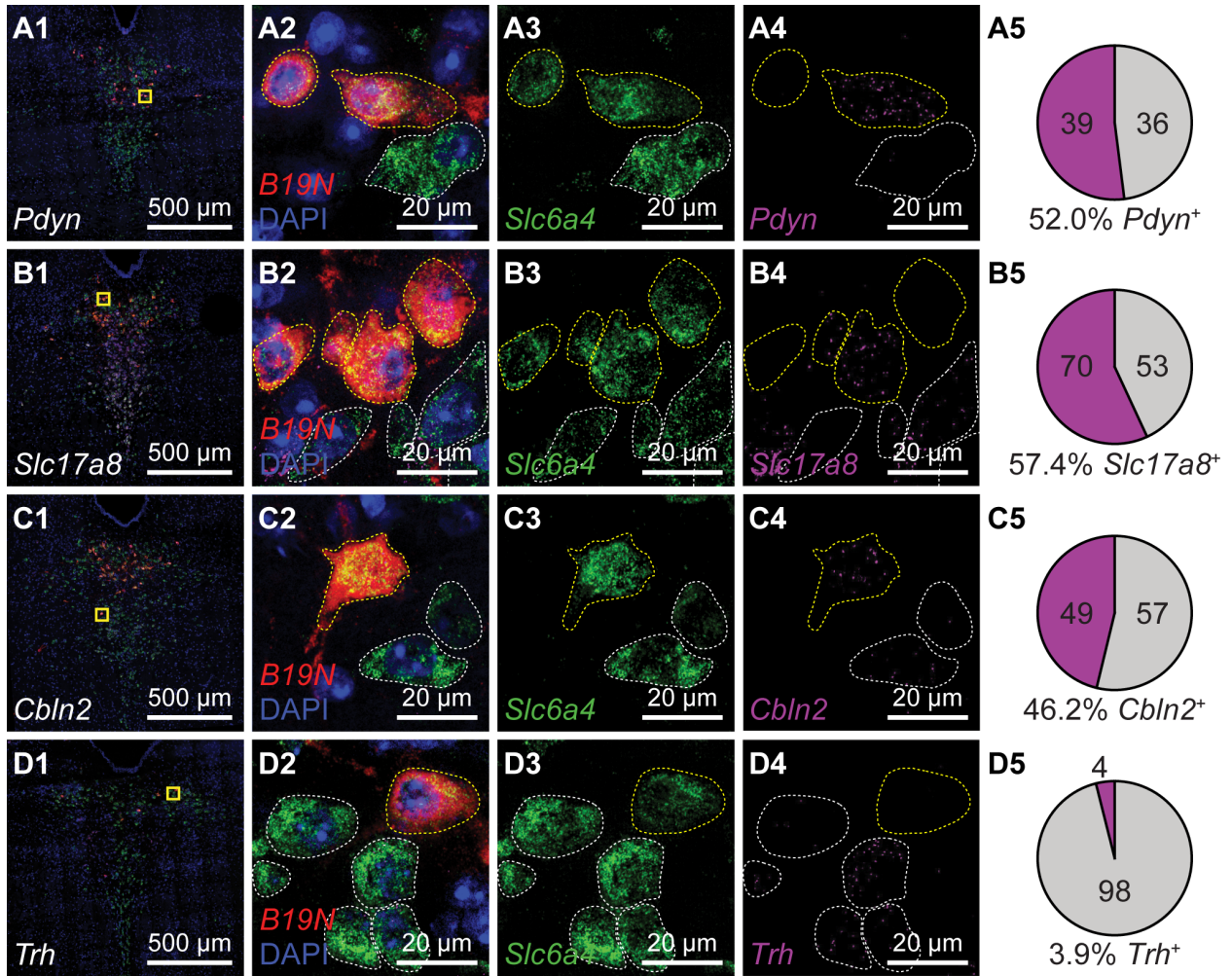
Figure 2.18: Quantification of RNAscope puncta in Str-projecting neurons.

Scatter plots with marginal histograms showing the quantification of the number of single molecule *FISH* puncta (RNAscope) in each Str-projecting cell. Each dot represents a single RbV-labeled cell. RbV-labeled cells were categorized based on expression of *Slc6a4* and one of four 5-HT subtype enriched genes: *Pdyn* (A) for 5-HT-III, *Slc17a8* (B) and *Cbln2* (C) for 5-HT-IV, and *Trh* (D) for 5-HT-I. Dashed lines in the scatter plots and marginal histograms indicate the thresholds used to binarize expression. Separate RNAscope experiments were performed for each 5-HT subtype enriched gene. All RbV-labeled cells in the analyzed images were included, including some cells in the pedunculopontine nucleus, and the number of RbV-labeled cells in each experiment is indicated in the plot.

Figure 2.19: Striatum receives inputs from multiple DRN 5-HT neuron subtypes.

Multiplexed *FISH* was used to identify rabies-infected Str-projecting 5-HT neurons in the DRN and quantify their expression of 5-HT subtype enriched genes. Rabies-infected neurons are identified by expression of the virus transcript *B19N*. Confocal images of the DRN from representative coronal sections are shown in column 1, and regions marked in yellow are expanded and separated by channel in columns 2-4. In columns 2-4, rabies-infected cells (*B19N*⁺) are outlined in yellow, whereas uninfected 5-HT neurons are outlined in white. The proportions of DRN 5-HT neurons that express each subtype-enriched gene are summarized in pie charts in column 5. Approximately half of the Str-projecting 5-HT neurons express the 5-HT-III enriched gene *Pdyn* (row A), and a similar proportion express 5-HT-IV enriched genes such as *Slc17a8* (row B) and *Cbln2* (row C). Most Str-projecting 5-HT neurons do not express the 5-HT-I enriched gene *Trh* (row D).

Figure 2.19 (Continued)



neurons), which is enriched in 5-HT-IV but also expressed in 5-HT-III at lower levels. Few Str-projecting neurons expressed *Trh* (4%, 4 of 102 RbV-labeled 5-HT neurons). This low proportion of *Trh*-expressing neurons is consistent with the low *Trh* expression in a small proportion of *Pdyn*⁺ 5-HT neurons (Figure 2.7H), and suggests that Str-projecting 5-HT neurons are unlikely to be subtype 5-HT-I neurons. Therefore, our results support the hypothesis that the Str-projecting DRN 5-HT neuron subpopulation is molecularly heterogeneous, and is comprised of at least 2 transcriptionally distinct 5-HT neuron subtypes.

Innervation of basal ganglia by a *Pdyn*-expressing 5-HT neuron subtype

The distribution of 5-HT-III subtype neurons overlapped with that of several projection-defined subpopulations that innervated nuclei of the basal ganglia beyond Str. To validate that the 5-HT-III subtype innervates the basal ganglia, we used an intersectional genetic targeting strategy to perform anterograde tracing from this subtype based on its enriched expression of *Pdyn*. We generated *Pet1-Flpe;Pdyn-IRES-Cre;LSL-FSF-ReaChR:mCitrine* mice in which *Pdyn*⁺;*Pet1*⁺ co-expressing neurons and their processes are fluorescently labeled by mCitrine-tagged ReaChR. To compare the innervation patterns of this subtype with that of the full DRN 5-HT neuron population, we also performed anterograde tracing from DRN *Pet1*⁺ neurons by injecting Cre-dependent adeno-associated viruses (AAVs) into the DRN of *Pet1-Cre* mice, labeling *Pet1*⁺ neurons in the dorsal and ventral DRN with EGFP and tdTomato respectively (Figure 2.20A). mCitrine-labeled axons from *Pdyn*⁺;*Pet1*⁺ neurons were found in a subset of regions innervated by DRN *Pet1*⁺ neurons (Figure 2.20B-F, Figure 2.21). Of the regions innervated by both DRN *Pet1*⁺ neurons and *Pdyn*⁺;*Pet1*⁺ neurons, the output nuclei of the basal ganglia, including the ventral pallidum (VP), entopeduncular nucleus (EP), and substantia nigra pars reticulata (SNr),

were most densely innervated by *Pdyn*⁺;*Pet1*⁺ neurons (Figure 8B-D). In contrast, sensory structures, such as the dLGN (Figure 8E), and limbic structures, such as the hypothalamus (Figure 2.20F) were not innervated by *Pdyn*⁺;*Pet1*⁺ neurons, despite receiving dense input from DRN *Pet1*⁺ neurons. These results therefore demonstrate that the *Pdyn*⁺ subtype 5-HT-III neurons broadly but selectively innervate structures that are either a part of or functionally linked to the basal ganglia, and are unlikely to be involved in sensory modulation.

2.4 Discussion

Here we present a transcriptomic map of cell types in and around the DRN, and outline the spatial organization of these cell types based on information contained in their molecular profiles. By overlaying transcriptional and anatomical features onto a common reference atlas, we describe the molecular basis for the organization of DRN 5-HT neurons into distinct subsystems. We uncovered 5 subtypes of DRN 5-HT neurons based on their gene expression profiles and showed that these are organized into distinct spatial domains within the DRN that are segregated along all three major anatomical axes. However, the spatial organization of molecularly defined 5-HT neurons does not conform to anatomical subdivisions as defined by cytoarchitecture of the DRN or the projection targets of 5-HT axons. The overlapping spatial distributions of 5-HT subtypes demonstrate the need for precise molecular and genetic approaches to dissect the function of each subtype. We also define a *Pdyn*-enriched 5-HT neuron subtype that is well-positioned to broadly but specifically alter the input and output of basal ganglia circuits, potentially mediating the modulation of motor control, decision making, and reinforcement learning by internal state.

Figure 2.20: *Pdyn*⁺ 5-HT neurons target basal ganglia circuits.

(A) Conditional anterograde tracing from subsets of 5-HT neurons. Anterograde tracing from *Pet1*⁺ DRN neurons was performed by injecting AAV2/1-CAG-FLEX-EGFP into the dorsal DRN and AAV2/1-CAG-FLEX-tdTomato into the ventral DRN of *ePet1-Cre* mice. A coronal section from the DRN injection site containing *Pet1*⁺ cells expressing either EGFP or tdTomato is shown on the left in (A1). *Pdyn*⁺;*Pet1*⁺ neurons were labeled by intersectional genetic targeting with a Cre- and Flp-dependent reporter line *R26-LSL-FSF-ReaChR:mCitrine* crossed to *Pdyn-IRES-Cre;Pet1-Flpe* mice. *Pdyn*⁺;*Pet1*⁺ expressing ReaChR:mCitrine in the DRN are shown on the right in (A2). 5-HT neurons are labeled by immunostaining for TPH2. (B-F) Axonal projections of *Pdyn*⁺;*Pet1*⁺ neurons were compared to projections of DRN *Pet1*⁺ neurons using separate approaches for conditional anterograde tracing. *Pdyn*⁺;*Pet1*⁺ neurons densely innervate many output nuclei of the basal ganglia, including VP (B2), EP (C2), and SNr (D2), which are also structures innervated by DRN *Pet1*⁺ neurons (B1, C1, and D1). *Pdyn*⁺;*Pet1*⁺ axons were not found in structures that were functionally distant from basal ganglia circuits, such as dLGN (E2) and hypothalamic nuclei (F2), although these structures received dense inputs from DRN *Pet1*⁺ neurons (E1 and F1). Regions outlined in yellow in B1 – F1 are enlarged in the insets showing EGFP⁺ / tdTomato⁺ axon fibers in each region. Abbreviations: DRN – dorsal raphe nucleus. VP – ventral pallidum. EP – entopeduncular nucleus. SNr – substantia nigra pars reticulata. dLGN – dorsal lateral geniculate nucleus. LH – lateral hypothalamus. VMH – ventromedial hypothalamus. All tissue sections are counterstained with fluorescent Neurotrace (Nissl).

Figure 2.20 (Continued)

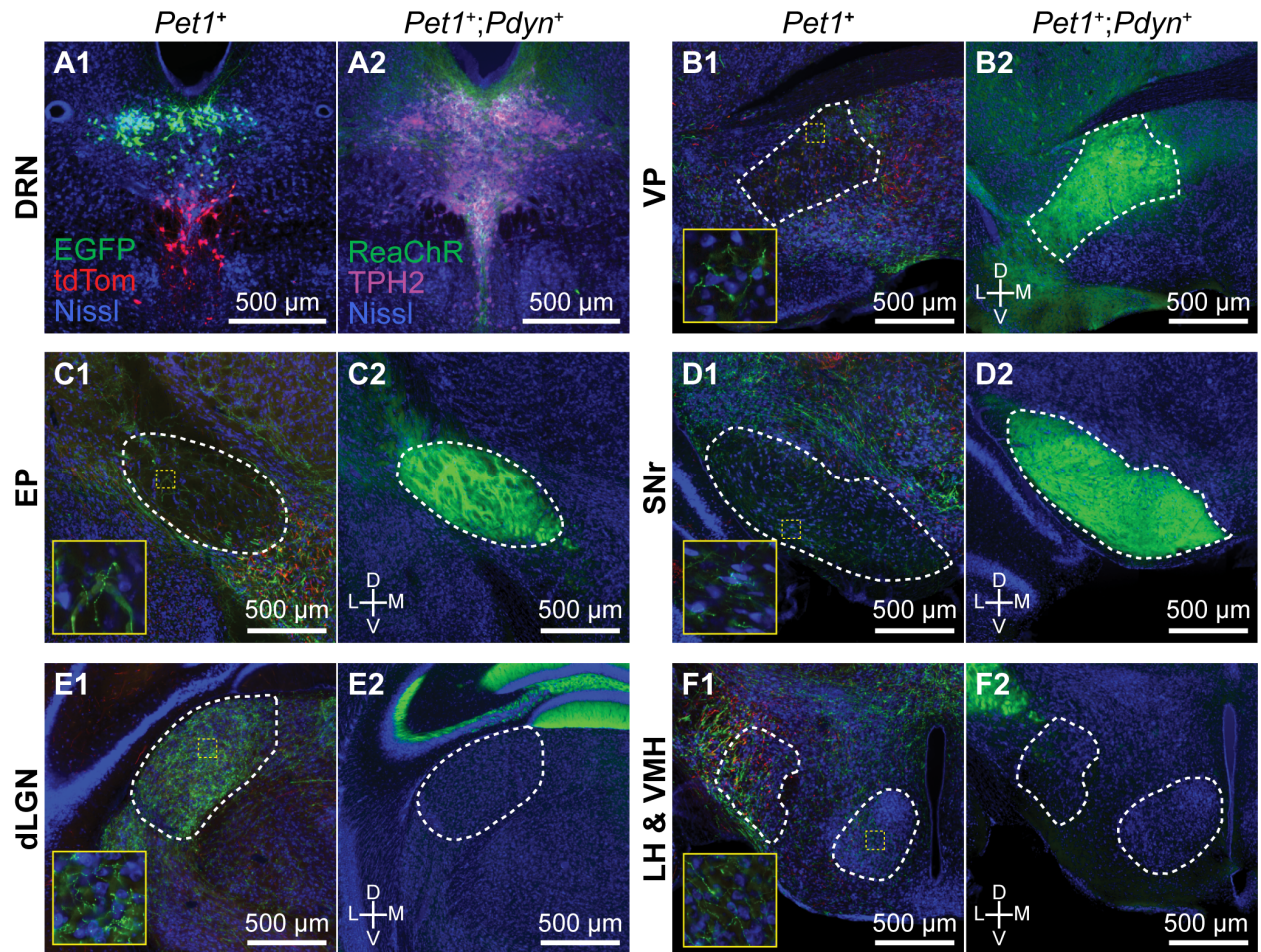
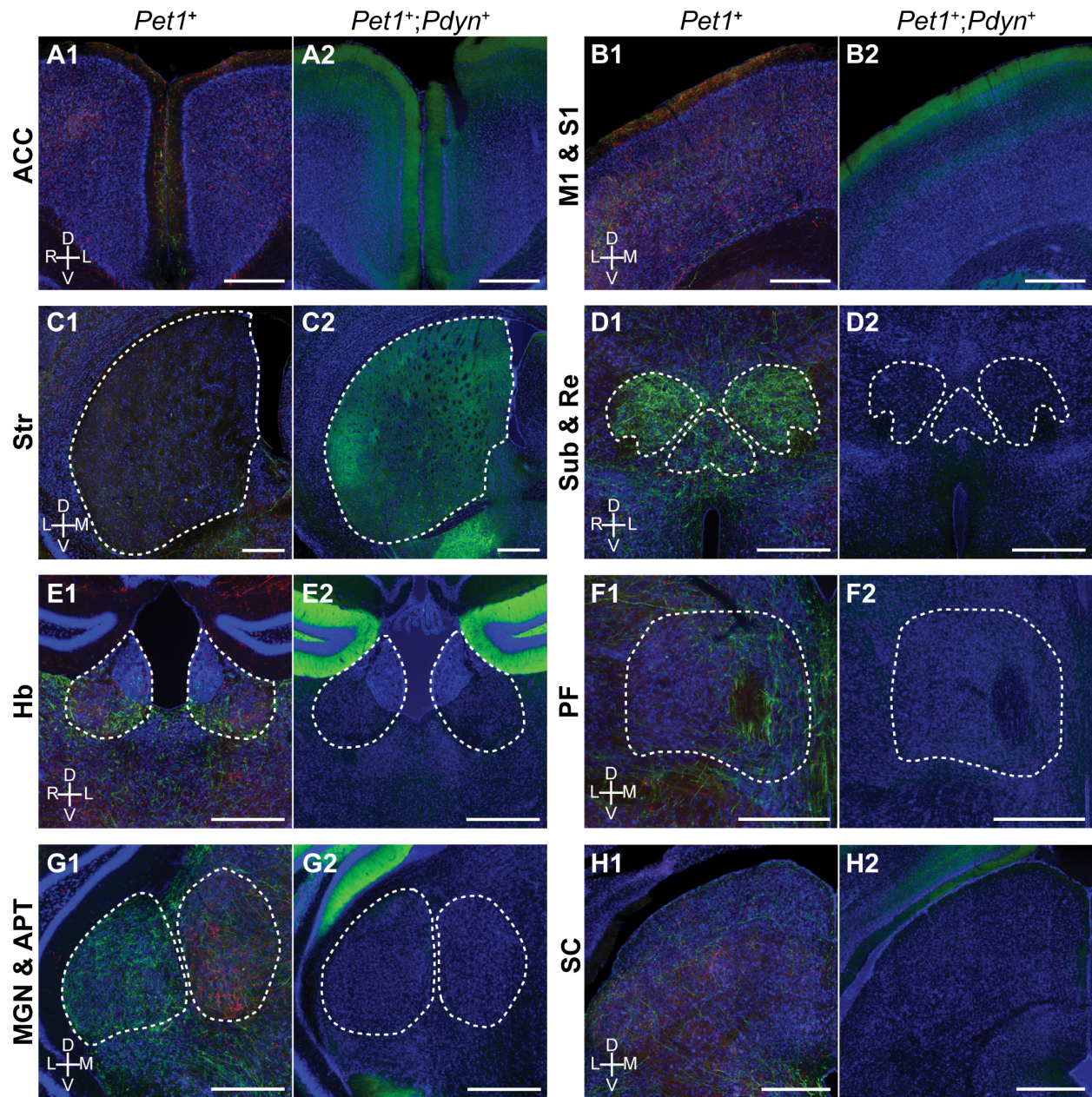


Figure 2.21: *Pet1*⁺;*Pdyn*⁺ neurons innervate a subset of regions targeted by DRN *Pet1*⁺ neurons.

Images of cortical and subcortical regions in the forebrain from conditional anterograde tracing of axons from DRN *Pet1*⁺ neurons and *Pdyn*⁺;*Pet1*⁺ neurons. Axons from *Pdyn*⁺;*Pet1*⁺ neurons were also found in frontal and prefrontal cortical regions (A-B), but were absent from thalamic nuclei that were innervated by DRN *Pet1*⁺ neurons (D-G) and subcortical regions outside of the basal ganglia, such as SC (H). Within Str, *Pdyn*⁺;*Pet1*⁺ axons were not uniformly distributed, with the highest density in the ventrolateral regions of Str. Abbreviations: ACC: anterior cingulate cortex; M1: primary motor cortex; S1: primary somatosensory cortex; Str: striatum; Sub: submedial thalamic nucleus; Re: nucleus reuniens; Hb: habenula; PF: parafascicular thalamic nucleus; MGN: medial geniculate nucleus; APT: anterior pretectal nucleus; SC: superior colliculus. Scale bars: 500 μ m.

Figure 2.21 (Continued)



Anatomical organization of DRN 5-HT neuron subtypes

We present a physical map combining both transcriptional and anatomical features and show that molecularly distinct DRN 5-HT neuron subtypes are spatially segregated into distinct anatomical subdomains and innervate different but overlapping targets. We reconstructed the spatial distribution of each 5-HT subtype using spatial correlation analysis of gene differentially expressed between subtypes and showed that each cytoarchitecturally-defined DRN subregion contains different molecularly-defined 5-HT subtypes. The subregional distribution of 5-HT subtypes relates well to past studies reporting subregion-specific anatomical and molecular differences that are consistent with our integrative map of 5-HT subtype features.

Of the 5 subtypes, the 5-HT-V was the most transcriptionally distinct and spatially restricted, and was found in a tight dorsomedial cluster in the posterior B6 tail of the DRN. Previous reports have suggested that the B6 5-HT neuron cluster is transcriptionally more similar to 5-HT neurons in the median raphe nucleus, despite being a part of the cytoarchitecturally-defined DRN (Commons, 2015). This has led to the proposal that the posterior DRN is an extension of the median raphe nucleus (MRN), although this remains to be validated using single cell transcriptomic profiling of both DRN and MRN 5-HT neurons. At the molecular level, 5-HT-V subtype neurons express a distinct set of receptors compared to the other 4 DRN 5-HT neuron subtypes. The localization of this subtype to the dorsomedial posterior B6 tail of the DRN also suggests that this subtype may innervate ventricular and subventricular regions and the choroid plexus and primarily target non-neuronal cells (Muzerelle et al., 2016). The transcriptomic profile of this subtype we present here will aid in the development of molecular and genetic approaches for targeting this subtype, and may facilitate studies on serotonergic modulation of

adult neurogenesis in the subventricular zone, as well as production and regulation of cerebrospinal fluid (CSF) by cells in the choroid plexus and ependymal lining of the ventricles (Banasr et al., 2004; Fisone et al., 1995; Moskowitz et al., 1979; Young et al., 2011).

The ventral DRN, comprised of the ventromedial subregion (or DRV) and interfascicular subregion (or DRI), contains mostly *Slc17a8*-enriched 5-HT-IV subtype neurons that innervate cortex (Ren et al., 2018). We noted that 5-HT-IV neurons were distributed throughout most of the anterior-posterior extent of the ventral DRN, although it is suggested that there is a topographical organization of cortical projecting 5-HT neurons along this axis. We speculate that this may reflect the broad and divergent cortical projections of individual 5-HT-IV neurons that collectively span most of the cerebral cortex. Alternatively, additional heterogeneity within the 5-HT-IV subtype may explain variation along the anterior-posterior axis that may be revealed with deeper sequencing.

In comparison, the dorsolateral DRN, also called the lateral wings of the DRN (lwDRN) and ventrolateral DRN (DRVL), showed strongly negative correlations with the 5-HT-IV subtype, particularly in the posterior half of the DRN where there is clearer spatial separation of *Tph2*⁺ neurons into medial and lateral compartments. Subtypes 5-HT-I and 5-HT-II were intermingled in this region, which is enriched in *Trh*, a 5-HT-I enriched gene. The dorsolateral subregion innervates many subcortical sensory and hypothalamic nuclei, in addition to motor nuclei in the brainstem (Lee et al., 2008; Muzerelle et al., 2016). We speculate that 5-HT-I and 5-HT-II form the cellular bases for the separation of DRN 5-HT projections to motor/limbic regions versus sensory regions respectively, given the expression of the TRH receptor gene (*Trhr*) in limbic

regions, such as the NAc shell, the bed nucleus of the stria terminalis, and hypothalamus, as well as several brainstem motor nuclei innervated by the DRN, such as the facial motor nucleus (Allen Brain Atlas). Further experiments using retrograde tracing and molecular profiling of DRN 5-HT neurons innervating these structures can be performed to evaluate these hypotheses. Additionally, the close spatial proximity of these 2 subtypes also presents a plausible mechanism for competitive inhibition between these separate subsystems via 5-HT_{1A} receptors and local 5-HT release, which may be relevant to selective sensory modulation by movement or changes in behavioral state (Hall et al., 2010; Yokogawa et al., 2012).

Although we show that 5-HT subtypes have distinct spatial locations, we also found considerable overlaps in their distributions, particularly within the dorsomedial subregion in the anterior DRN that contains many basal ganglia-projecting 5-HT neurons. While the *Pdyn*-expressing 5-HT-III subtype was localized to the dorsomedial subregion, subtypes 5-HT-I and 5-HT-II were also found in this subregion in the anterior third of the DRN despite being distributed to dorsolateral subregions in more posterior sections. Furthermore, a detailed comparison of the 5-HT subtype distributions with cytoarchitecturally-defined subregion boundaries showed that subtype distributions are not confined within these subregion boundaries, especially in the anterior half of the DRN. The poor correspondence between molecularly-inferred and cytoarchitecturally-defined spatial domains cautions against the use of anatomical subregions for targeting 5-HT subsystems.

Molecular organization of DRN 5-HT subsystems

5-HT neurons are organized into discrete subsystems that (i) have distinct and dissociable behavioral functions, and (ii) are comprised of 5-HT neurons possessing unique molecular, physiological, and anatomical properties. However, the complex architecture of the DRN has impeded efforts to understand the interrelationship of these three aspects of 5-HT diversity, as necessary to study the differential properties and functions of each subsystem and its distinct subtype of 5-HT neuron. Given the extensive overlaps in the distribution of different 5-HT neuron subsets at the anatomical level, we were motivated by the hypothesis that a transcriptome-based molecular definition of 5-HT neuron subtypes was required to both understand the organization of heterogeneous 5-HT neuron subtypes as well as to enable their precise targeting for functional analyses. Consistent with this hypothesis, our results suggest that many of the physiological and anatomical differences between 5-HT neuron subtypes are a result of molecular differences specified by expression of overlapping but distinct transcriptional networks.

Some key technical limitations of scRNA-seq, particularly for droplet-based methods such as the inDrop platform used in this study, are the relatively low transcript capture efficiency and low number of reads per cell. The higher occurrence of drop-out events, which are failures in detecting expressed transcripts in a cell, also makes it more difficult to detect low copy transcripts that may be important for distinguishing between highly similar subtypes, such as the 5-HT-I and 5-HT-II subtypes in our study. Thus our study does not seek to present a definitive catalogue of all neuron subtypes present in the DRN, since the techniques used are limited in their ability to resolve finer levels of heterogeneity and differential expression of low copy

transcripts. In spite of these limitations, our study still successfully captures a substantial amount of transcriptional heterogeneity to resolve differences between neuron subtypes that are informative of their diverse morphological and functional features. Furthermore, we find differential expression of transcription factors across subtypes that may underlie many of these molecular differences that are specified during the development of each subtype. The dynamics of these gene expression programs can be further elucidated by future studies that sample multiple time points along the developmental trajectory of the DRN. Further studies incurring a trade-off on cell count and the number of cell types captured for higher sequencing depth may also resolve additional transcriptional heterogeneity between subtypes within specific populations. Eventually these molecular approaches will be well complemented by whole-brain reconstructions of axons of single neurons (Economio et al., 2016; Gong et al., 2016) as well as spatial transcriptomics (Chen et al., 2015; Wang et al., 2018).

Local interactions between DRN cell types

Our scRNA-seq dataset yields predictions about local interactions involving DRN cells, including those with non-neuronal cells, based on the expression patterns of known receptor-ligand pairs. For example, the expression of *Hdc* in ependymal cells suggests that ependymal cells may signal to nearby neurons via non-synaptic release of histamine. Histaminergic paracrine signaling from ependymal cells can exert differential effects on various neuronal subtypes based on proximity to the cerebral aqueduct and differential expression of histaminergic receptors. Notably, the histamine receptors *Hrh1* and *Hrh3* are expressed in 5-HT subtypes 5-HT-I, 5-HT-II, and 5-HT-III, which are all located in dorsal DRN subregions in close proximity to the cerebral aqueduct. In contrast, 5-HT-IV subtype neurons, which are in ventral subregions further

from the aqueduct, do not express detectable levels of *Hrh1* and express *Hrh3* at very low levels. Enrichment of the G_i-coupled *Hrh3* receptor in 5-HT-III further suggests that histamine may inhibit this subtype while increasing the excitability of 5-HT-I and 5-HT-II neurons. Release of peptides such as *Pdyn* from a subset of ependymal cells can also have differential effects dependent on the expression pattern of the κ-opioid receptor. Additionally, ependymal cells may communicate via secretion of these transmitters and peptides into the CSF. Transmitters and peptides released into the ventricular system can have long range effects facilitated by the flow of CSF and signal to neuronal cells extending processes to the ventricular walls, including some 5-HT neurons, as well as non-neuronal cells including ventricular immune cells and choroid plexus cells.

We also found that pvMΦs within or in close proximity to the DRN express the G_i-coupled *Htr1b* receptor, unlike pvMΦs in brain regions that do not contain 5-HT neurons. This suggests that pvMΦs in different brain regions may be specialized via differential expression of neurotransmitter receptors to be specifically tuned to monitor their local environment and respond to changes in neuronal activity. Activation of G_i-coupled pathways on pvMΦs via 5-HT_{1B} receptors is also a potential mechanism for the regulation of macrophage polarization and inflammatory responses by tonic 5-HT release within the DRN, which may be relevant to the increasing importance of neuroinflammatory pathways in the etiology of psychiatric disorders (Brisch et al., 2017; Howerton et al., 2014; Watkins et al., 2014).

The diversity of neuronal subtypes in and around the DRN also highlights the importance of elucidating local circuitry with knowledge of the molecular identity of both pre- and post-

synaptic neurons. For direct signaling between 5-HT neurons, somatodendritic release of 5-HT and activation of inhibitory 5-HT_{1A} receptors on adjacent 5-HT neurons is likely to mediate lateral inhibition between the 5-HT neurons of the same subtype, due to the spatial clustering of the subtypes. However, GABAergic and/or glutamatergic neurons may be excited by adjacent 5-HT neurons via activation of their 5-HT_{2C} and 5-HT₇ receptors to mediate indirect interactions between 5-HT neuron subtypes. These interactions may be either synergistic if mediated by glutamatergic neurons innervating other 5-HT subtypes, or antagonistic in a form of lateral inhibition via GABAergic interneurons. Subtype-specific connections between 5-HT neurons and local GABAergic and glutamatergic neurons can mediate interactions between different subsystems and may contribute to the contrasting and opposing functions ascribed to the DRN as a whole. Although 5-HT neurons have been reported to form local connections (Weissbourd et al., 2014), it is currently unknown how the 18 neuronal subtypes we have described are organized into local circuits. To generate models of these local circuits, the connectivity between DRN and ventrolateral PAG neurons will need to be mapped with subtype-level molecular resolution. This will likely require the use of retrograde tracing techniques with improved specificity for targeting neuronal subtypes in combination with spatial transcriptomic methods that are compatible with the large volume of the DRN. These methods can also be extended to examine the interactions between larger networks of 5-HT subsystems distributed across the raphe nuclei, which have been shown to be interconnected based on conditional anterograde tracing using intersectional targeting of 5-HT neurons originating from different embryonic rhombomeres (Bang et al., 2012).

A 5-HT subsystem targeting basal ganglia circuits

The transcriptomic information we obtained on DRN 5-HT neuron subtypes allowed us to access a specific 5-HT subsystem that innervates circuits of the basal ganglia. We showed that the subsystem comprised of the *Pdyn*-enriched subtype 5-HT-III sends broad projections to both input and output nuclei of the basal ganglia, while avoiding other sensory and limbic structures, which have distinct functions from the basal ganglia and are likely to receive inputs from other DRN 5-HT neuron subtypes. Although we also showed that the basal ganglia receives inputs from multiple 5-HT neuron subtypes, particularly in the case of the Str-projecting subpopulation, the dense innervation of basal ganglia output nuclei by 5-HT-III neurons suggests that this 5-HT subsystem has a prominent role in the regulation of motor output and action selection through its effects on the activity of basal ganglia output nuclei. We also speculate that 5-HT release from this subsystem may have different effects on distinct output channels of the basal ganglia, given the differential expression of 5-HT receptors on distinct subpopulations of SNr and EP projection neurons (Saunders et al., 2018; Wallace et al., 2017). The targeting of distinct channels or subcircuits within the basal ganglia may also be consistent with the innervation of the striatum by multiple 5-HT neuron subtypes given the topographical arrangement of convergent cortical inputs into distinct domains within the striatum (Hintiryan et al., 2016), since it is plausible that distinct striatal domains are each innervated by a different but functionally related 5-HT neuron subtype. Subcircuit-specific effects of 5-HT within the basal ganglia would also have implications on models for the function of 5-HT in decision-making and motor control (Migueluez et al., 2014; Reed et al., 2013), although further work is needed to elucidate the structural and functional organization of these subcircuits in the basal ganglia (Calabresi et al., 2014).

Our results provide a resource for the design of intersectional strategies for the functional dissection of DRN cell types. The *LSL-FSF-ReaChR:mCitrine* intersectional reporter line that we used for conditional anterograde tracing will also be suitable for optogenetic perturbation experiments *in vivo* to investigate the circuit and behavioral functions of these distinct 5-HT subsystems. Greater spatial specificity can be achieved through the use of tapered optic fibers for site-specific light delivery (Pisanello et al., 2014), intersectional viral constructs (Fenno et al., 2014) optimized for expression in cell types of interest, and the development of additional Cre and Flp recombinase driver lines with improved specificity to increase the number of subtypes and subsystems that can be accessed through genetic and molecular approaches. The functional studies facilitated by the development of these additional tools will provide further mechanistic insights into the coordinated action of distinct cell types and subsystems of the DRN in the regulation of behavior.

2.5 Materials and Methods

Mice

The following mouse strains/lines were used in this study: C57BL/6J (The Jackson Laboratory, Stock # 000664), *Pet1-Cre* (The Jackson Laboratory, Stock # 012712), *Pet1-Flpe* (from the lab of Susan Dymecki [Jensen et al., 2008]), *Pdyn-IRES-Cre* (The Jackson Laboratory, Stock # 027958), and *R26-LSL-FSF-ReaChR:mCitrine* (The Jackson Laboratory, Stock # 024846).

Animals were kept on a 12:12 regular light/dark cycle under standard housing conditions. All procedures were performed in accordance with protocols approved by the Harvard Standing Committee on Animal Care following guidelines described in the U.S. National Institutes of Health Guide for the Care and Use of Laboratory Animals.

Adeno-Associated Viruses (AAVs)

Recombinant AAVs used for anterograde tracing experiments (AAV2/1-CAG-FLEX-EGFP, AAV2/1-CAG-FLEX-tdTomato) were commercially obtained from the Penn Vector Core. Virus aliquots were stored at -80 °C, and were injected at a concentration of approximately 10^{12} GC/ml.

Rabies Viruses

Rabies viruses used for retrograde tracing (B19G-SADΔG-EGFP, B19G-SADΔG-tdTomato) were generated in-house (Osakada and Callaway, 2013; Wickersham et al., 2010). Virions were amplified from existing stocks in several rounds of low-MOI passaging through BHK-B19G cells by transferring filtered supernatant, with 3 to 4 days between passages a maximum of 3 passages. Cells were grown at 35 °C and 5% CO₂ in DMEM with GlutaMAX (Thermo

Scientific, #10569010) supplemented with 5% heat-inactivated FBS (Thermo Scientific #10082147) and antibiotic-antimycotic (Thermo Scientific #15240-062). Media containing virions were collected at the end of the last passaging round and incubated with benzonase nuclease (1:1000, Millipore #70664) at 37°C for 30 min, followed by filtration through a 0.22 µm PES filter. Filtered supernatant was transferred to ultracentrifuge tubes (Beckman Coulter #344058) with 2 ml of a 20% sucrose in dPBS cushion and ultracentrifuged at 20,000 RPM (Beckman Coulter SW 32 Ti rotor) at 4°C for 2 hours. The supernatant was discarded and the pellet was resuspended in dPBS for 6 hours on an orbital shaker at 4 °C before aliquots were prepared and frozen for long-term storage at -80 °C. Unpseudotyped rabies virus titers were estimated using a serial dilution method counting infected HEK 293T cells and quantified as infectious units per ml (IU/ml).

Stereotaxic Surgeries

Mice were initially anesthetized with 5% isoflurane (80% oxygen) and maintained at 1-2.5% isoflurane after placement on the stereotaxic frame (David Kopf Instruments, Model 1900 Stereotaxic Alignment System). The scalp was cleaned and sterilized before an incision was made to expose the skull, and sterile ophthalmic ointment was applied to the eyes. For leveling the horizontal plane, a stereotaxic alignment tool (David Kopf Instruments, Model 1905) was used to zero the relative dorsoventral displacement of Bregma and Lambda, as defined in the Paxinos & Franklin Mouse Brain Atlas (Paxinos and Franklin, 2001), for adjusting tilt of the anterior-posterior axis, and of two points equidistant to the left and right of Bregma for adjusting the tilt of the medial-lateral axis. Craniotomies were prepared using a mounted drill (David Kopf Instruments, Model 1911) with careful removal of the bone flap and overlying dura using forceps

and a fine needle tip, and were covered with sterile 0.9% saline before and during the injection to prevent desiccation. Viruses were front-filled into a pulled glass pipette (Drummond Scientific, #5-000-2005) filled with mineral oil (Millipore Sigma, M3516) and connected to a 5 μ l Hamilton syringe (Hamilton #84850) via polyethylene tubing filled with mineral oil. Glass pipettes were pulled to obtain a tip size of approximately 40-60 μ m on a pipette puller (Sutter Instrument Co., P-97). Viruses were infused into target regions at approximately 100 nl/min using a syringe pump (Harvard Apparatus, #883015), and pipettes were slowly withdrawn ($< 10 \mu\text{m/s}$) at least 10 min after the end of the infusion. Following wound closure, mice were placed in a cage with a heating pad until their activity was recovered before returning to their home cage. Mice were given pre- and post-operative oral carprofen (MediGel CPF, 5mg/kg/day) as an analgesic, and monitored daily for at least 4 days post-surgery.

Stereotaxic Injection Coordinates and Volumes

All coordinates are relative to Bregma along the anterior-posterior axis and medial-lateral axis, and relative to the pial surface along the dorsoventral axis. “BL” denotes the distance between Bregma and Lambda (as defined in the Paxinos mouse brain atlas). Angles for DV coordinates are relative to the dorsoventral axis along the sagittal plane, with 0° being a straight vertical approach and negative values denoting a posterior-to-anterior approach. Dorsal raphe nucleus (DRN): AP = $-(6.25 * \text{BL} / 4.35)$ mm, ML = 0.00 mm, DV = -3.33 mm at -40°, 200-300 nl. Ventrolateral striatum (vlStr): AP = +0.40 mm, ML = ± 2.45 mm, DV = -3.10 mm at 0°, 300 nl. Dorsal lateral geniculate nucleus (dLGN): AP = $-(2.00 * \text{BL} / 4.20)$ mm, ML = ± 2.25 mm, DV = -3.00 mm at 0°, 150 nl. Globus pallidus, external (GPe): AP = +0.14 mm, ML = ± 2.34 mm, DV = -3.90 mm at 0°, 200 nl. Lateral hypothalamic area (LHA): AP = -1.46 mm, ML = ± 1.10 mm,

DV = -5.10 mm at 0°, 150 nl. Habenula (Hb): AP = $-(1.30 * BL / 4.2)$ mm, ML = ± 0.43 mm, DV = -2.80 mm at 0°, 50 nl. Nucleus accumbens core (NAcc): AP = +1.54 mm, ML = ± 1.10 mm, DV = -4.00 mm at 0°, 300 nl. Primary motor cortex (M1), 6 sites: AP = {+2.10 mm, +1.60 mm, +1.10 mm}, ML = { ± 1.75 mm, ± 1.60 mm, ± 1.60 mm}, DV = {[-1.20 mm, -0.60 mm], [-1.10 mm, -0.50 mm], [-1.00 mm, -0.40 mm]} at 0°, 150 nl per site. Medial prefrontal cortex (mPFC), 4 sites: AP = {+2.4 mm, +1.8 mm}, ML = ± 0.40 mm, DV = {-1.65 mm, -1.25 mm} at 0°, 150 nl per site.

Single Cell Dissociation and RNA Sequencing

8- to 10-week old C57BL/6J mice were pair-housed in a regular 12:12 light/dark cycle room prior to tissue collection. Mice were transcardially perfused with an ice-cold choline cutting solution containing neuronal activity blockers (110 mM choline chloride, 25 mM sodium bicarbonate, 12 mM D-glucose, 11.6 mM sodium L-ascorbate, 10 mM HEPES, 7.5 mM magnesium chloride, 3.1 mM sodium pyruvate, 2.5 mM potassium chloride, 1.25 mM sodium phosphate monobasic, 10 μ M (R)-CPP, 1 μ M tetrodotoxin, saturated with bubbling 95% oxygen/5% carbon dioxide, pH adjusted to 7.4 using sodium hydroxide). Brains were rapidly dissected out and sliced into 250 μ m thick coronal sections on a vibratome (Leica Biosystems, VT1000) in a chilled cutting chamber filled with choline cutting solution. Coronal slices containing the DRN were then transferred to a chilled dissection dish containing a choline-based cutting solution for microdissection. Fiber tracts were used for guiding the microdissection but were excluded from the collected tissue chunk. Dissected tissue chunks were transferred to cold HBSS-based dissociation media (Thermo Fisher Scientific Cat. # 14170112, supplemented to final content concentrations: 138 mM sodium chloride, 11 mM D-glucose, 10 mM HEPES, 5.33

mM potassium chloride, 4.17 mM sodium bicarbonate, 2.12 mM magnesium chloride, 0.9 mM kynurenic acid, 0.441 mM potassium phosphate monobasic, 0.338 mM sodium phosphate monobasic, 10 μ M (R)-CPP, 1 μ M tetrodotoxin, saturated with bubbling 95% oxygen/5% carbon dioxide, pH adjusted to 7.35 using sodium hydroxide) supplemented with an additional inhibitor cocktail (10 μ M triptolide, 5 μ g/ml actinomycin D, 30 μ g/ml anisomycin) and kept on ice until dissections were completed. Dissected tissue chunks for each sample were pooled into a single tube for the subsequent dissociation steps. Tissue chunks were first mixed with a digestion cocktail (dissociation media, supplemented to working concentrations: 20 U/ml papain, 1 mg/ml pronase, 0.05 mg/mL DNase I, 10 μ M triptolide, 5 μ g/ml actinomycin D, 30 μ g/ml anisomycin) and incubated at 34 °C for 90 min with gentle rocking. The digestion was quenched by adding dissociation media supplemented with 0.2% BSA and 10 mg/ml ovomucoid inhibitor (Worthington Cat. # LK003128), and samples were kept chilled for the rest of the dissociation procedure. Digested tissue was collected by brief centrifugation (5 min, 300 g), re-suspended in dissociation media supplemented with 0.2% BSA, 1 mg/ml ovomucoid inhibitor, and 0.05 mg/mL DNase I. Tissue chunks were then mechanically triturated using fine-tip plastic micropipette tips of progressively decreasing size. The triturated cell suspension was filtered in two stages using a 70 μ m cell strainer (Miltenyi Biotec Cat # 130-098-462) and 40 μ m pipette tip filter (Bel-Art Cat. # H136800040) and washed in two repeated centrifugation (5 min, 300 g) and re-suspension steps to remove debris before a final re-suspension in dissociation media containing 0.04% BSA and 15% OptiPrep (Sigma D1556). Cell density was calculated based on hemocytometer counts and adjusted to approximately 100,000 cells/ml. Single-cell encapsulation and RNA capture on the InDrop platform was performed at the Harvard Medical School ICCB Single Cell Core using v3 chemistry hydrogels based on previously described protocols (Zilionis

et al., 2017). Suspensions were kept chilled until the cells were flowed into the microfluidic device. Libraries were prepared and indexed following the protocols referenced above, and sequencing-ready libraries were stored at -80 °C. Libraries from different samples were pooled and sequenced on an Illumina NextSeq 500 (High Output v2 kits).

Sequencing Data Processing

NGS data was processed using previously a published pipeline in Python available at <https://github.com/indrops/indrops> (Klein et al., 2015). Briefly, reads were filtered by expected structure and sorted by the corresponding library index. Valid reads were then demultiplexed and sorted by cell barcodes. Cell barcodes containing fewer than 250 total reads were discarded, and remaining reads were aligned to a reference mouse transcriptome (Ensembl GRCm38 release 87) using Bowtie 1.2.2 ($m = 200$, $n = 1$, $l = 15$, $e = 100$). For alignment, the mouse transcriptome was modified with the addition of genes from the SAD B19 rabies viruses and transgenes (*B19N*, *B19P*, *B19M*, *B19L*, *EGFP*, *tdTomato*, *AmCyan1*). Aligned reads were then quantified as UMI-filtered mapped read (UMIFM) counts. UMIFM counts and quantification metrics for each cell were combined into a single file sorted by library and exported as a gunzipped TSV file.

Pre-Clustering Filtering and Normalization

Analysis of the processed NGS data was performed in R (version 3.4.4) using the *Seurat* package (version 2.3.1) (Butler et al., 2018; Satija et al., 2015). A custom R script was used to combine the expression data and metadata from all libraries corresponding to a single batch, and cells with fewer than 500 UMIFM counts were removed. The expression data matrix (Genes x Cells) was filtered to retain genes with > 5 UMIFM counts, and then loaded into a *Seurat* object along with

the library metadata for downstream processing. The percentage of mitochondrial transcripts for each cell (*percent.mito*) was calculated and added as metadata to the *Seurat* object. Cells in the object were further filtered using the following parameters: *Reads* – *min.* 20000, *max.* *Inf*; *nUMI* – *min.* 500, *max.* 18000; *nGene* – *min.* 200, *max.* 6000; *percent.mito* – *min.* *-Inf*, *max.* 0.1. Low quality libraries identified as outliers on scatter plots of quality control metrics (e.g. unusually low gradient on the nGene vs. nUMI) were also removed from the dataset. Filtered *Seurat* objects were then log-normalized at 10,000 transcripts per cell. Effects of latent variables (*nUMI*, *percent.mito*, *Sex*, *orig.ident*) were estimated and regressed out using a GLM (*ScaleData* function, *model.use* = “*linear*”), and the scaled and centered residuals were used for dimensionality reduction and clustering.

Dimensionality Reduction and Batch Effect Correction

Canonical correlation analysis (CCA) was used for dimensionality reduction and mitigation of batch effects. We used the union of the top 2000 highly variable genes from each batch dataset (3341 genes) and used the *RunCCA* function in *Seurat* to calculate 50 canonical variates (CVs). After inspection of the CVs, the first 35 CVs were used for subspace alignment when merging datasets from different batches into a single *Seurat* object. Cells with expression profiles not well explained by CVs (*var.ratio.pca* < 0.5) were removed from the dataset before clustering.

Cell Clustering and Cluster Identification

Initial clustering was performed on the merged and CCA-aligned dataset using the first 35 CVs, and t-SNE was used only for data visualization. Clustering was run using the SNN-based *FindClusters* function using the SLM algorithm and 10 iterations. Clustering was performed at varying resolution values, and we chose a final value of 2 for the resolution parameter for this stage of clustering. Clusters were assigned preliminary identities based on expression of combinations of known marker genes for major cell classes and types. A list genes used for identifying major cell classes and types is provided in Supplementary File 1. Low quality cells were identified based on a combination of low gene/UMIFM counts and high levels of mitochondrial and nuclear transcripts (e.g. *Malat1*, *Meg3*, *Kcnq1ot1*) typically clustered together and were removed. Following assignment of preliminary identities, cells were divided into data subsets as separate Seurat objects (neurons, astrocytes, ependymal cells, vascular cells, immune cells, oligodendrocytes and polydendrocytes) for further subclustering. The expression matrix for each data subset was further filtered to include only genes expressed by the cells in the subset (minimum cell threshold of 0.5% of cells in the subset). Subclustering was performed iteratively on each data subset to resolve additional cell types and subtypes. Briefly, clustering was run at high resolution, and the resulting clusters were ordered in a cluster dendrogram built using the Ward2 method in *hclust* using cluster-averaged gene expression for calculating the Euclidean distance matrix. Putative doublets/multiplets were identified based on co-expression of known marker genes for different cell types (e.g. neuronal and glial markers, or endothelial cell and pericyte markers). Putative doublets tended to separate from other cells and cluster together, and these clusters were removed from the dataset. Cluster separation was evaluated using the *AssessNodes* function and inspection of differentially expressed genes at each node. Clusters

with poor separation, based on high OOBE scores and differential expression of mostly housekeeping genes, were merged to avoid over-separation of the data. The dendrogram was reconstructed after merging or removal of clusters, and the process of inspecting and merging or removing clusters was repeated until all resulting clusters could be distinguished based on a set of differentially expressed genes that we could validate separately. For small clusters that were previously identified in preliminary analysis of the separate batches, such as the *Met*-expressing 5-HT neuron subtype, or expected clusters based on existing literature, such as the *Slc17a8⁺;Fev⁻* neurons, manual identification and clustering was performed if these cells were not separated by the clustering algorithm.

Differential Expression Tests

Tests for differential gene expression were performed using *MAST* version 1.4.1 (Finak et al., 2015) through the *FindMarkersNode* function in *Seurat* (*logfc.threshold* = 0.25, *min.pct* = 0.1). P values were corrected using the Benjamini-Hochberg method and filtered a 5% false discovery rate ($Q < 0.05$).

Gene Ontology Term Enrichment Tests

GO term enrichment tests were performed using the *goseq* package version 1.30.0 in R (Young et al., 2010). Genes differentially expressed between 5-HT neuron subtypes were used as the target list, and all genes expressed in the 5-HT neuron dataset were used for the background list. Enrichment scores were calculated using the Wallenius approximation method in *goseq*, and terms were filtered using Q values at a 5% false discovery rate (Benjamini-Hochberg correction).

Spatial Correlation Analysis

Spatial correlation analysis was performed in MATLAB (MathWorks, R2016b and R2018b). A spatial expression matrix for the differentially expressed (DE) genes was constructed using *in situ* hybridization images from the Allen Brain Atlas. Only DE genes with coronal imaging data were included in the matrix to achieve sufficient resolution along the dorsal-ventral and medial-lateral axes. For each gene, *ISH* images spanning the DRN were downsampled by a factor of 2 before registration and expression quantification using a custom MATLAB script. The midline of each slice was vertically aligned and centered, and images were and cropped to retain a region spanning approximately 1 mm across the midline containing the DRN. Cropped images were each assigned to a position along the anterior-posterior axis corresponding to a coronal section from the Allen Brain Atlas averaged coronal template (100 μm intervals). Expression was binarized by thresholding the image, and positive cells were detected using a Laplacian-of-Gaussian spot detection algorithm. Spatial expression patterns were obtained from two-dimensional histograms (bin size = 50 μm x 50 μm) of positive cells counts in each slice. Fine alignment of each 2D histogram along the dorsal-ventral axis was adjusted manually using *Tph2* *ISH* images as the reference. Anatomical landmarks visible in the Nissl or background stain, such as the cerebral aqueduct and fiber tracts, were used for the fine adjustment. Aligned histograms were cropped to retain a square region (36 bins x 36 bins) containing the DRN. Cropped 2D histograms were averaged with the left-right reflection, and the *ISH* count data for each experiment (36 bins x 36 bins x 12 sections) was unrolled into a row vector. Row vectors for the same gene were averaged, ignoring NaN values from missing *ISH* data, to obtain a single row vector for each gene. Row vectors for each gene were concatenated to generate the spatial expression matrix. The spatial expression matrix (Genes x Bins) was further filtered in two

stages: bins with no *Tph2* expression were removed, and genes were filtered based on total expression and mean-normalized variance (Figure 5–Figure Supplement 1). Pearson correlation coefficients were calculated between the averaged gene expression of each 5-HT neuron subtype cluster from the scRNA-seq dataset and each spatial bin in the filtered spatial expression matrix.

Histology for Anatomical Tracing

Mice were deeply anesthetized with isoflurane and transcardially perfused with 5-10 ml chilled 0.1 M PBS, followed by 10-15 ml chilled 4% paraformaldehyde in 0.1 M PBS. Brains were dissected out and post-fixed overnight at 4 °C, followed by incubation in a storing/cryoprotectant solution of 30% sucrose and 0.05% sodium azide in 0.1 M PBS for at least 1-2 days to equilibrate. 50 µm coronal slices were prepared on a freezing microtome (Leica Biosystems, SM2010 R). Slices were either immunostained (see section on Immunohistochemistry), or counterstained using Neurotrace 435 (ThermoFisher Scientific N21479) at a concentration of 1:100 in 0.1 M PBS with 0.5% Triton X-100. Slices were mounted in VectaShield mounting media (Vector Labs, H-1000) and imaged on an Olympus VS120 slide scanning microscope. Confocal images were taken on an Olympus FV1000 or FV1200 confocal microscope for assessing co-localization.

Immunohistochemistry

50 µm thick free-floating tissue sections were rinsed 3 x 5 min with 0.1 M PBS containing 0.5% Triton X-100 (PBST) and blocked in a PBST-based solution containing 6% normal goat serum for 1 hour at room temperature. The blocking solution was then removed, and slices were incubated overnight at 4 °C in a PBST-based antibody carrier solution containing 3% normal

goat serum and rabbit anti-TPH2 primary antibodies (Millipore, ABN60) diluted 1:1000. After incubation in the primary antibody carrier solution, slices were rinsed 4 x 5 min with PBST, and then incubated in carrier solution containing goat anti-rabbit Alexa Fluor 647 at 1:500 (ThermoFisher Scientific, A-21244) and Neurotrace 435 at 1:100 for 2 hours at room temperature. Slices were then rinsed 2 x 5 min in PBST and 2 x 5 min in PBS before mounting with VectaShield mounting media (Vector Labs, H-1000).

Fluorescent *In Situ* Hybridization (FISH)

Animals were deeply anesthetized with isoflurane before decapitation. Brains then were rapidly removed, frozen on dry ice, and embedded in tissue freezing media (Tissue-Tek O.C.T. compound). 20 µm coronal sections were prepared on a cryostat (Leica Biosystems, CM1950) and mounted onto SuperFrost Plus glass slides (VWR) at 100 µm intervals between slices in a set. Slices were rapidly refrozen once mounted, and stored at -80 °C before staining. Multiplexed fluorescent *in situ* hybridization was performed using the ACDBio RNAscope V1 reagents and protocols. Briefly, slices were fixed in 4% paraformaldehyde at 4 °C for 15 minutes and dehydrated through washing steps in ethanol at increasing concentrations (50%, 70%, 100%) before protease digestion (Protease III, 10 minutes at room temperature). Probes and amplification/detection reagents were applied to the tissue sections and incubated under conditions stated in the V1 detection protocol provided by ACDBio. Sections were counterstained using DAPI provided in the V1 detection reagent kits and mounted in ProLong Gold mounting media (ThermoFisher Scientific P36934). Single-plane tiled images covering the DRN were scanned using a confocal microscope (Leica SP8X, 1.40 NA 63X magnification oil

immersion objective). Tile merging was performing in the Leica LAS X software, with a 10% tile overlap and statistical blending.

FISH Image Analysis

Confocal images were first processed in Fiji. A custom macro was written to convert Leica image files (.lif format) into TIFF format for downstream analysis steps. Channels in the merged tile images were processed separately. For each channel, a median filter (1 pixel radius) was applied before images were cropped and downsampled by a factor of 2 with bicubic interpolation. A rolling ball background subtraction (50 pixel radius) was then applied before images for each channel was saved as a separate 8-bit TIFF file. A pixel classifier run in Ilastik (version 1.2.2) was applied on the output TIFF files to generate probability maps of *B19N*-expressing cell bodies for automated segmentation of rabies-infected cells. Cell segmentation and RNAscope puncta quantification was performed using a custom pipeline in CellProfiler (version 3.1.5). Puncta counts were exported as TSV files for further analysis and data visualization using custom scripts written in R and MATLAB.

Data Availability

The sequencing datasets generated in this study are available on the NCBI Gene Expression Omnibus (accession number: GSE134163). R data files containing the processed and annotated scRNA-seq data in the form of Seurat objects are also available on the Harvard Dataverse (<https://dataverse.harvard.edu/dataset.xhtml?persistentId=doi:10.7910/DVN/QB5CC8>).

Chapter 3:
**Single-Cell Analysis of Antiviral Neuroinflammatory Responses in the Dorsal Raphe
Nucleus**

Kee Wui Huang and Bernardo L. Sabatini

This chapter is adapted from a manuscript in preparation.

Author Contributions:

K.W.H. performed the experiments and data analysis. K.W.H. and B.L.S. designed the experiments and wrote the manuscript.

3.1 Abstract

Neuroinflammatory processes have been implicated in both neurodegenerative and psychiatric diseases. However, the specific functions of each cell type in mediating immune responses in the brain have yet to be elucidated. Here we used single-cell RNA sequencing to assess both global and cell type-specific transcriptional responses in the mouse dorsal raphe nucleus following long-range infection by rabies viruses (RbVs). We analyzed 60,212 single-cell transcriptomes from both RbV-injected and uninjected control animals to reveal several transcriptionally diverse infiltrating leukocyte populations that are distinct from resident immune cells. RbV transcripts were detected in both serotonergic projection neurons and microglia despite the sparse detection of infected neurons. Pathway analyses based on differential gene expression between RbV-injected and uninjected controls revealed a down-regulation of metabolic processes and neurotransmission following infection of neurons by RbVs. Assessment of cell type-specific cytokine expression showed that antiviral transcriptional responses were largely orchestrated by Type I and Type II interferon signaling by microglia and CD4⁺ T cells respectively. Detailed sub-clustering analysis further revealed transcriptionally distinct states of microglia along an activation trajectory that may serve different functions, including lipid metabolism, antigen presentation, and cytokine secretion. We also describe changes in the inferred structure of cell type-specific intercellular interactions during the antiviral inflammatory response. Our study uncovers the cellular and molecular heterogeneity of immune cells that mediate inflammatory responses in the brain, and provides additional insights into the distinct contributions of various cell types in mediating different facets of the immunological response.

3.2 Introduction

Neuroinflammatory processes are increasingly recognized for their importance in the etiology of many neurological and psychiatric disorders. Recent studies have found significant associations between genes with known immune functions and diseases that include Alzheimer's Disease and schizophrenia (Henstridge et al., 2019; Kunkle et al., 2019; Mathys et al., 2019; Sekar et al., 2016). Microglia, the predominant resident immune cells of the central nervous system (CNS), express many of these disease-associated genes, and undergo transcriptional changes and diversification in both acute and chronic models of inflammation and neurodegeneration (Hammond et al., 2019; Jordão et al., 2019; Li et al., 2019; Mrdjen et al., 2018). However, the functions of these transcriptionally distinct microglial subsets and the interactions that trigger these changes during microglial activation have yet to be elucidated.

Immune responses in the brain also limit the use of viruses as gene delivery vectors in the CNS. There has been great interest in the development and use of viral vectors for their applications in clinical gene therapy, including recently engineered variants of adeno-associated viruses (AAVs) that cross the blood-brain barrier with high efficiency (Chan et al., 2017). A wide variety of other viruses have been exploited as tools that have been essential for advances in basic neuroscience research, including single-stranded RNA viruses such as vesicular stomatitis virus (VSV), and rabies virus (RbV) (Ghanem and Conzelmann, 2016; Mundell et al., 2015; Wickersham et al., 2007). However, immune responses elicited by these viral tools have not been fully characterized. Additionally, the utility of many viruses are limited by their toxicity in neurons, as well as the clearance of both virions and virus-infected cells by the immune system.

Understanding the various mechanisms by which the immune system and CNS respond to these viruses may facilitate the design of improved tools and strategies to circumvent these caveats.

Here we used high-throughput single-cell RNA sequencing (scRNA-seq) and assessed changes in gene expression and cell type composition of the mouse dorsal raphe nucleus (DRN) following long-range infection of DRN neurons by glycoprotein-deleted rabies viruses (RbVs). Analysis of 60,212 single-cell transcriptomes from both RbV-injected and uninjected control mice revealed several types of infiltrating leukocytes in the DRN that are recruited by chemokines released from several glial cell types. Analysis of the transcriptional changes by cell type also revealed both global and cell type-specific gene sets and pathways that underlie the antiviral defense response. Additionally, we identified transcriptionally distinct subsets of microglia that may represent different functional states along an activation trajectory. Our results provide further insights into the shared and unique functions performed by various CNS cell types to mediate different facets of the immunological response.

3.3 Results

Recruitment of circulating leukocytes into the DRN following rabies virus infection

Inflammatory responses were induced in the DRN by long-range infection of DRN neurons using glycoprotein-deleted RbVs of the SAD Δ G B19 strain, which are frequently used as tools for retrograde tracing to map neural connectivity (Wickersham et al., 2007; Ghanem and Conzelmann, 2016). Retrograde infection of DRN neurons by RbVs permitted the physical separation of the injection site from the location of the infected neuronal cell bodies, and reduced the effects of physical tissue damage. Responses in the DRN were studied since pro-

inflammatory signaling and immunological perturbations in the DRN have been implicated in behavioral and mood disorders that include impulsivity, major depressive disorder, and bipolar disorder (Baumann et al., 2002; Brisch et al., 2017; Howerton et al., 2014; Mahmood and Silverstone, 2001; Matthews and Harrison, 2012).

Tissue containing the DRN was collected from RbV-injected animals (4 mice – 2 male, 2 female) 7 days post-injection. RbVs were injected into a pair of brain regions that were both innervated by DRN neurons, and included the striatum (Str), dorsal lateral geniculate nucleus (dLGN), nucleus accumbens (NAc), and substantia nigra (SN) (Figure 3.1A). Tissue chunks were dissociated into live whole cell suspensions, and single-cell RNA-seq (scRNA-seq) libraries were prepared using the inDrop v3 platform (Klein et al., 2015; Zilionis et al., 2017). Inhibitors of neural spiking activity, transcription, and translation were included to reduce the effects of tissue dissociation on gene expression (Hrvatin et al., 2018). Single-cell transcriptomes from RbV-injected animals were analyzed together with cells collected from uninjected animals (Huang et al., 2019), and datasets were merged using CCA-based dataset alignment methods (Butler et al., 2018). Low-quality cells and putative multiplets were manually identified and discarded prior to analysis of differential gene expression (see Methods). Our final merged dataset contained a total of 60,212 cells – 20,581 cells in the RbV group (10,065 male, 10,516 female), and 39,631 cells in the Control group (17,496 male, 22,135 female). Cells were sequenced to a mean read depth of 62,061 reads/cell (min. = 20,001; median = 47,823; IQR = 43,294; max. = 870,064), 2,603 UMI-filtered mapped reads (UMIFMs) (min. = 501; median = 2,093; IQR = 1,849; max. = 17,997) and mean gene detection rate of 1,027 genes/cell (min. = 201; median = 896; IQR = 706; max. = 5,518). Separation of the cells by condition showed that

Figure 3.1: Recruitment of leukocytes in response to viral infection.

(A) Experiment schematic. Unpseudotyped SAD Δ G B19 rabies viruses (RbV) were injected into 8-10 week old C57BL/6J mice. Each animal received a pair of injections into two different regions innervated by DRN 5-HT neurons. Tissue containing the DRN was dissected 7 days post-injection and dissociated into whole cell suspensions. scRNA-seq libraries were generated using the microfluidic-based inDrop platform. Age-matched uninjected animals were used as the Control group. **(B)** UMAP plot of merged dataset containing 60,212 cells. Control and RbV datasets were merged using CCA-based dataset alignment methods. Individual points representing single cells are color-coded by cell class/type. **(C)** UMAP plot of merged dataset with cells color-coded by condition (RbV or Control). Clusters corresponding to lymphocytes and non-resident myeloid cells (Non-Res. Myeloid) were almost entirely comprised of cells from RbV but not Control group. **(D)** Stacked bar plot showing the relative proportion of each cell type in RbV and Control groups. Cell class/type categories are color-coded following the same scheme as panel (B). **(E) Left:** Dendrogram with cell class/type labels corresponding to the cluster labels in (B). **Right:** Dot plot showing expression of several example genes (columns) used for identifying the major cell classes/types (rows). The color of each dot represents the average log-scaled expression of each gene across all cells in a given cluster, and the size of the dot represents the fraction of cells in the cluster in which transcripts for that gene were detected. Each cluster was identified using combinations of genes, including many other genes not included in this plot.

Figure 3.1 (Continued)

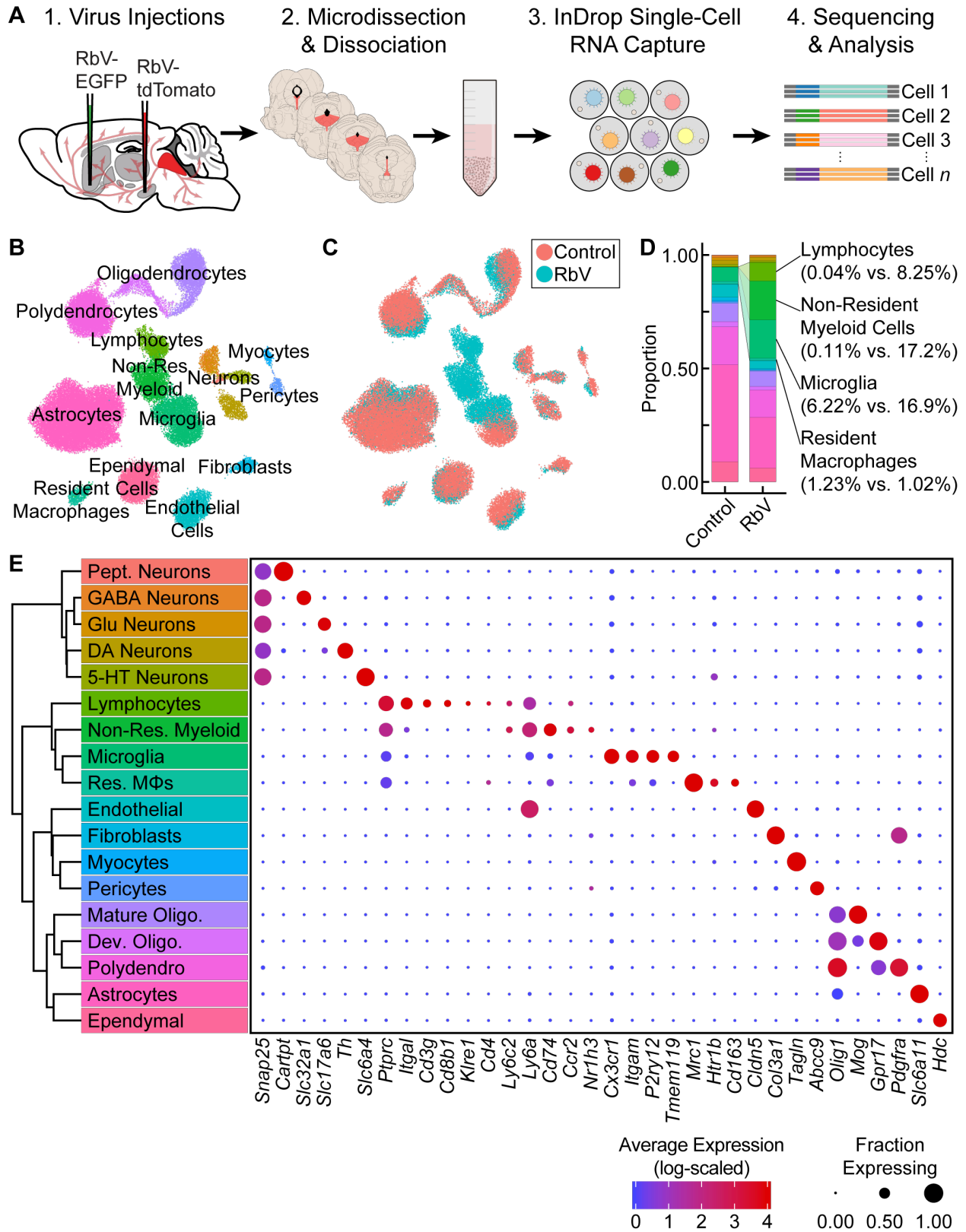
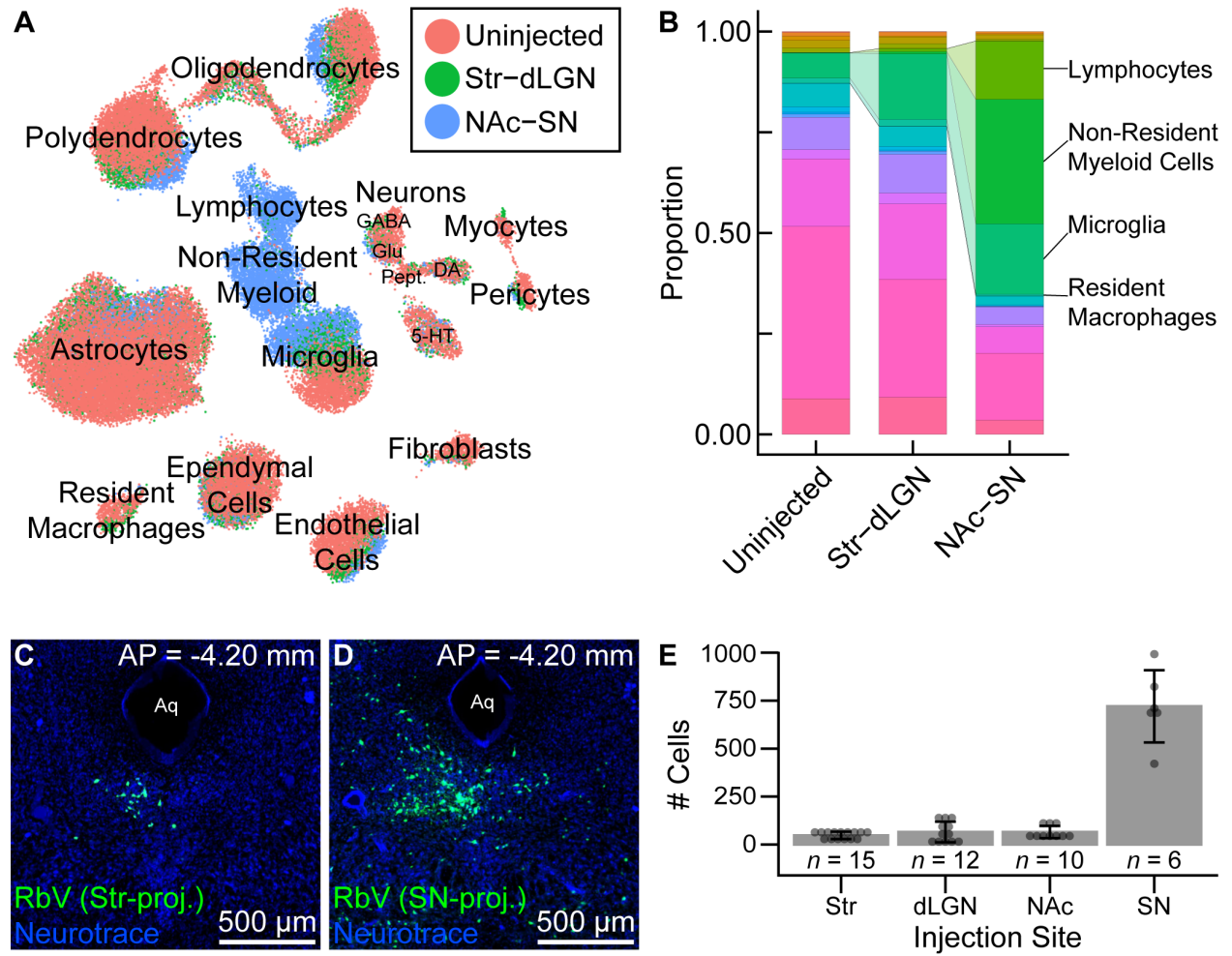


Figure 3.2: Leukocyte recruitment varies with infection magnitude.

(A) UMAP plot of merged dataset with each cell color-coded by the injection site grouping. Specific neuron types are indicated and labeled by their primary neurotransmitter. (B) Stacked bar plot showing the relative proportion of each cell class/type in each of the injection site groups. The microglia population was expanded in both the Str-dLGN injection group and NAc-SN group compared to the Uninjected (Control) group. Lymphocytes and non-resident myeloid cells were expanded in the NAc-SN injection group but not Str-dLGN group compared to Controls. Resident macrophages showed the least change across all groups. (C) Fluorescence image of a representative coronal section showing DRN neurons infected by RbV injected into the ipsilateral Str. (D) Fluorescence image showing neurons in the DRN and vIPAG infected by RbV injected into the ipsilateral SN. (E) Bar plots showing the mean number RbV labeled cells for different injection sites. Counts from individual mice are represented as points, and the height of each bar indicates the mean for each group. Error bars are S.E.M. Injections targeting SN ($n = 6$ mice) infected approximately 10-fold more neurons than injections targeting Str ($n = 15$ mice), dLGN ($n = 12$ mice), or NAc ($n = 10$ mice). All injections sites were targeted in the right hemisphere. Injection volumes and virus titers were matched across injection sites. Abbreviations: Aq – cerebral aqueduct. dLGN – dorsal lateral geniculate nucleus. NAc – nucleus accumbens. SN – substantia nigra. Str – striatum. Scale bars: 500 μm . All coronal sections were counterstained with Neurotrace 435.

Figure 3.2 (Continued)



each group was sequenced to comparable read depths with the RbV group having a higher mean (Control: 1st quartile = 30,670, median = 45,709, mean = 58,359, 3rd quartile = 69,928; RbV 1st quartile = 34,090, median = 52,542, mean = 69,191, 3rd quartile = 85,428). However, the UMIFM count (Control 1st quartile = 1,574, median = 2,338, mean = 2,856, 3rd quartile = 3,499; RbV 1st quartile = 1,082, median = 1,649, mean = 2,117, 3rd quartile = 2,605) and gene detection rates (Control 1st quartile = 741, median = 1,041, mean = 1,173, 3rd quartile = 1,446; RbV 1st quartile = 420, median = 612, mean = 745.8, 3rd quartile = 942) were slightly lower in the RbV group compared to the Control group.

Cells in the merged dataset were clustered using a graph-based clustering algorithm in the CCA-aligned space (see Methods). Inspection of genes enriched in each cell cluster showed that all of the resident cell types that we previously identified in the reference dataset were present in the RbV group (Figure 3.1B, E). However, there was a significant expansion in the proportion of immune cells in the RbV group (Figure 3.1C-D). This included an increase in the proportion of microglia ($n = 5,949$ cells, 16.9% of RbV vs. 6.2% of Control), but not resident macrophages (Res. MΦs) ($n = 698$ cells, 1.02% RbV vs. 1.23% of Control). We also identified both myeloid and lymphoid cell clusters that were not previously found in the uninjected Control group. A large cluster of myeloid cells that are distinct from microglia and resident MΦs formed a significant proportion of the cells in the RbV-injected group ($n = 3,575$ cells, 17.2% of RbV vs. 0.11% of Control), and the proportion of lymphocytes was also greatly increased in the RbV-injected group ($n = 1,714$ cells, 8.25% of RbV vs. 0.04% of Control). The appearance of these non-resident immune cells is likely due to the infiltration of the brain parenchyma by circulating leukocytes, since blood was removed from the brain via transcatheter perfusion prior to tissue

collection. A comparison of the proportion of immune cells in groups sorted by RbV injection sites suggested that leukocyte infiltration scales with infection magnitude, which was assessed as the mean number of RbV-infected neurons labeled by each injection (Figure 3.2A-E). While samples collected from mice that received a pair of RbV injections into the Str and dLGN showed an increase in the proportion of microglia compared to Control/Uninjected animals (Uninjected = 6.2%; Str-dLGN = 16.3%; NAc-SN = 17.5%), animals that received SN injections had a larger increase in the proportion of lymphocytes (Uninjected = 0.04%; Str-dLGN = 0.75%; NAc-SN = 14.5%) and non-resident myeloid cells (Uninjected = 0.11%; Str-dLGN = 0.55%; NAc-SN = 30.9%) (Figure 3.2A-B). Histological analyses quantifying the number of RbV-infected neurons in the DRN and surrounding ventrolateral PAG with varying injection targets showed that injection of RbV into SN infected an order of magnitude more neurons than Str NAc, or dLGN injections (Figure 3.2C-E).

Rabies virus transcripts are detected in both neurons and microglia

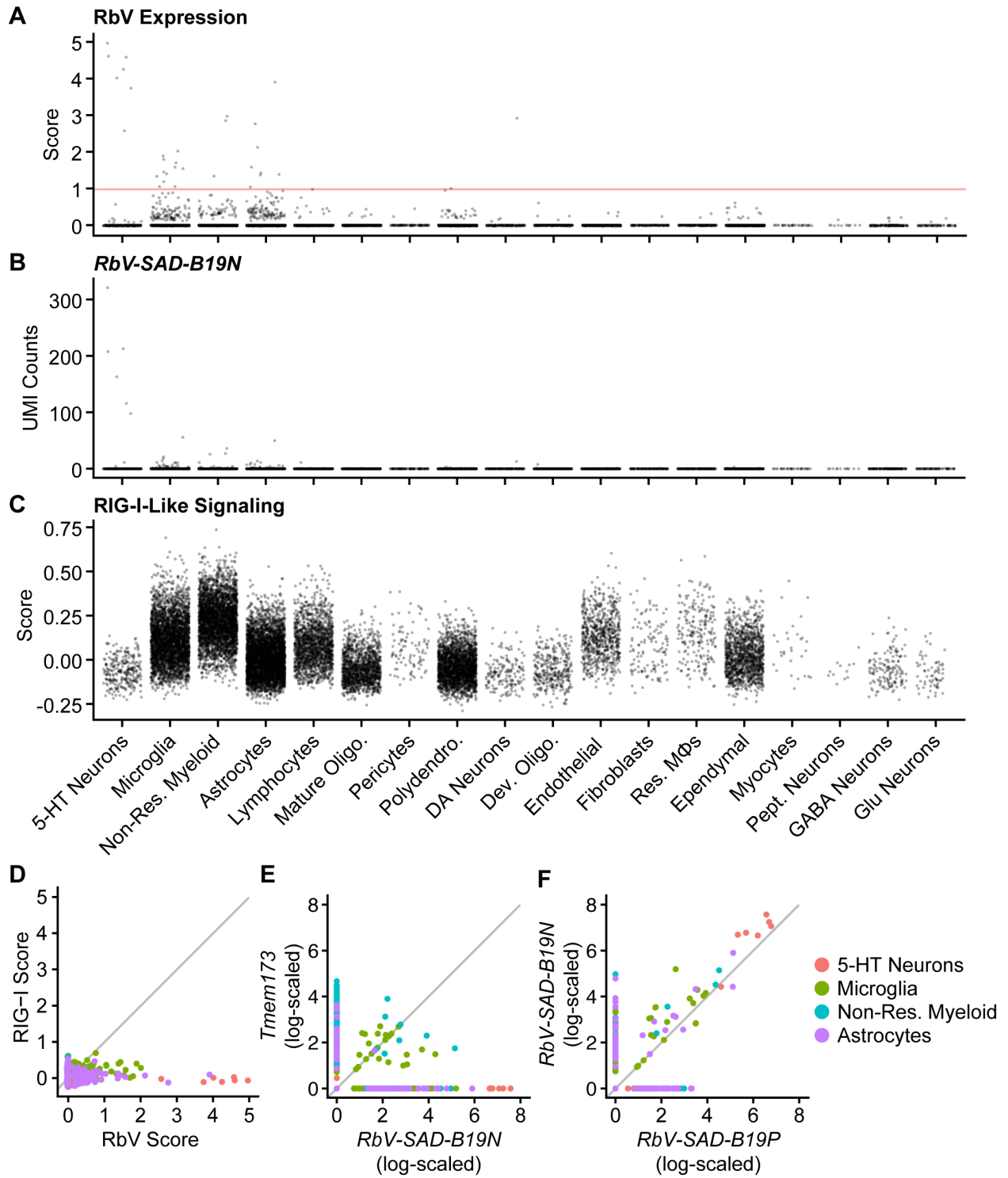
To identify projection neurons that are infected by RbVs, we calculated RbV gene set expression scores for each cell (see Methods) and examined the distribution of RbV gene transcripts in each cell type in the RbV group (Figure 3.3). As expected from the innervation of the injection sites by 5-HT neurons, the 5-HT neuron cluster ($n = 275$ cells in RbV group) had the highest average RbV expression scores. However, the rate of detecting cells containing RbV transcripts was low. The low yield of RbV-infected neurons could be due to the following: (i) since cells were not sorted during tissue dissociation, only a small fraction of RbV-infected neurons were captured during the cell encapsulation and mRNA capture given the typical capture efficiency of 30-50%; (ii) RbV-infected neurons may have poor survival during the tissue digestion and dissociation

Figure 3.3: RbV transcripts are detected in neurons and phagocytic cells.

(A-C) Dot plots showing the RbV gene set expression scores (A), *RbV-SAD-B19N* transcript counts (B), and RIG-I-Like signaling gene set expression scores (C) for individual cells grouped by cell class/type.

Only cells from the RbV group are displayed. Cell classes/types (columns) are ordered horizontally by the average RbV expression score. 5-HT neurons have the highest RbV expression scores, followed by microglia, non-resident myeloid cells, and astrocytes. Most other cell types do not have scores above the threshold denoted by the horizontal red line. 5-HT neurons also have the highest UMI counts for RbV genes such as *RbV-SAD-B19N*. RbV transcripts were also detected in microglia, non-resident myeloid cells, and astrocytes at lower levels. Expression of genes involved in RIG-I and RIG-I-like signaling (C) is highest in non-resident myeloid cells and microglia, whereas neurons have the lowest scores for genes in this pathway. (D-F) Scatter plots for gene set expression scores (D) and log-scaled gene expression (E-F) in cells from the 4 cell types with the highest average RbV gene set expression scores. Points are single cells color coded by cell. No correlation was observed between the RIG-I-like signaling gene set expression score and RbV gene set expression score (D). Expression of *Tmem173* (STING) was highest in non-resident myeloid and microglia, but was low in 5-HT neurons even in cells with high expression of the *RbV-SAD-B19N* (E). Expression of genes within the RbV gene set, such as *RbV-SAD-B19N* and *RbV-SAD-B19P* were correlated (F). *RbV-SAD-B19N* expression was also higher compared to all other RbV genes, as previously described. Gray lines in D-F indicate the line of unity ($x = y$).

Figure 3.3 (Continued)



and were therefore relatively depleted from the whole cell suspensions; (iii) given the relatively low read depths and the lack of enrichment for RbV transcripts during library preparation, there are likely to be transcripts from RbV-infected cells that were not sequenced (drop-outs in scRNA-seq); (iv) few RbV-infected neurons were labeled due to the low labeling efficiency of the viruses. Despite the low detection rate, the RbV-infected cells that were identified retained sufficient transcriptional information for clustering and assignment of cell class/type identity.

RbV transcripts were also detected in non-neuronal cells: microglia ($n = 3,483$ cells in RbV group), non-resident myeloid cells ($n = 3,530$ cells in RbV group), and astrocytes ($n = 4,605$ cells in RbV group) showed the next 3 highest average RbV expression scores and had more than 1 cell above the score threshold (red line in Figure 3.3A). These cells are unlikely to have been directly infected by RbV, given the tropism of RbVs, the lack of transsynaptic spread by the glycoprotein-deleted RbVs used, and the long distance of the DRN from the injection sites. A comparison of RbV transcript counts between 5-HT neurons, predicted to be the cells directly infected by RbVs, and the other 3 non-neuronal cell types showed that maximum number of RbV transcript counts in these non-neuronal cells was at least an order of magnitude lower than 5-HT neurons (Figure 3.3B). We hypothesize that the detection of RbV transcripts in these cells are due to their phagocytosis of mRNA-containing material released from infected neurons. The non-zero background counts of RbV transcripts that we observed in other cells may also be due to the capture of free-floating RbV transcripts released from the physical disruption of some RbV-infected cells during tissue digestion and dissociation.

RNA viruses can be recognized via pattern recognition receptors that include RIG-I and RIG-I-like receptors (e.g. MDA5), which detect foreign RNA. Since RIG-I and RIG-I-like pathways are thought to be the primary means of detecting infection by RNA viruses, we calculated the per cell expression score of genes in the KEGG RIG-I-like signaling pathway gene set (Figure 3.3C). All neuron cell types had low scores for expression of genes involved in RIG-I-like signaling. Surprisingly, we did not observe a positive correlation between the RIG-I signaling gene set expression score and the RbV gene set expression score (RbV group, all cells, Pearson R = 0.02) (Figure 3.3D), whereas a positive correlation was observed between RbV genes despite the occurrence of drop outs (RbV group, all cells, Pearson R = 0.57) (Figure 3.3F). Genes downstream of RIG-I, such as *Tmem173* (STING) were also low even in 5-HT neurons with high expression of RbV transcripts (Figure 3.3E). However, previous studies have shown that RbV components that are still expressed by the glycoprotein-deleted mutants we used, such as the P protein, may inhibit interferon signaling in infected neurons (Brzózka et al., 2006; Faul et al., 2009; Scott and Nel, 2016). The low expression of interferon stimulated genes (e.g. *Isg15*) and low RIG-I-like signaling gene set expression scores across neuronal types may also indicate an underlying difference in the function of neurons versus glia in innate immunity – astrocytes and microglia, which form close associations with synapses and neurons, may serve more prominent roles in the detection of pathogens and neuronal infection due to the suppression of these pathways in neurons.

Identification of global and cell type-specific transcriptional changes

To assess the population-level transcriptional responses to RbV infection, we first performed differential expression (DE) tests on simulated “bulk” RNA-seq samples separated into RbV and Control groups (Figure 3.4A). “Bulk” samples were simulated by averaging UMI counts for each gene across all cells in a group regardless of cell type. Many genes involved in antiviral immune responses that were expressed at low levels in the Control group were strongly up-regulated in the RbV group. These included interferon response genes such as *Isg15*, major histocompatibility complex (MHC) genes such as *H2-Aa* and *H2-D1*, and genes that are highly expressed by infiltrating leukocytes such as *Ptprc*. Gene set enrichment analysis (GSEA) using the MSigDB Hallmark gene sets (Liberzon et al., 2015; Subramanian et al., 2005) showed that genes involved in type I and type II interferon responses were highly up-regulated, as well as various signaling pathways such as complement, IL-2, IL-6, and TNF α (Figure 3.4B). Genes involved in cell division were also up-regulated, consistent with the proliferation and clonal expansion of microglia and T cells upon activation. Our results are also consistent with prior studies that have used bulk tissue profiling methods to evaluate transcriptional changes in the CNS following exposure to RbVs (Prosniak et al., 2001; Zhao et al., 2011; Zhao et al., 2018).

We next assessed the transcriptional changes in resident cell types by performing DE tests and gene set enrichment analysis (GSEA) separately for each cell type/class (see Methods). Most DE genes that were strongly up- or down-regulated (388 genes with Q value < 0.01, absolute log₂ fold-change > 1) were found to be differentially expressed in only 1 of the 12 resident cell types (Figure 3.4C), and were considered cell type-specific DE genes (204 of 388 genes). Several genes were differentially expressed in 9 or more cell types and were considered part of a

“global” response program (35 of 388 genes). These genes included many of the interferon stimulated genes such as *Isg15* and other genes involved in the inflammatory response. Pathway analysis using GSEA on Reactome pathway gene sets showed that the cell types varied in their responses. Neurons had the most number of down-regulated pathways (28 up-regulated, 148 down-regulated), whereas microglia had the highest number of up-regulated pathways (96 up-regulated, 61 down-regulated) (Figure 3.4D). Reactome pathways that were globally up-regulated included cytokine signaling and the adaptive immune system, whereas globally down-regulated pathways were mostly related to metabolism, such as translation, oxidative phosphorylation/electron transport, lipid metabolism, and mRNA metabolism (Figure 3.4E). The down-regulation of these pathways may be driven by the antiviral response in an attempt to inhibit viral replication and spread, and may also relate to the reduction in the UMIFM and gene detection rate in the RbV group relative to the Control group.

Several pathways were enriched in only a subset of cell types but not found to be cell type-specific. Genes involved in apoptosis were up-regulated in resident immune cells, fibroblasts, and astrocytes, but were down-regulated in neurons. mRNA splicing was also up-regulated in microglia and mature oligodendrocytes while being down-regulated in other glial cell types including developing oligodendrocytes. Genes involved in neurotransmission were also down-regulated in neurons and glial cell types that express neurotransmitter receptors or are involved in the regulation of synaptic transmission, including astrocytes and polydendrocytes. A reduction in neurotransmission may contribute to the host defense by limiting the spread of neurotropic viruses across synapses, and has been suggested to be induced by IFN γ signaling (Kim et al., 2002).

Figure 3.4: Rabies infection induces both global and cell type-specific transcriptional changes.

(A) Simulated “bulk” RNA-seq – scatter plot of \log_2 -transformed mean transcript counts for each gene comparing averaged expression in RbV versus Control groups. UMI counts for each gene were averaged across all cells in each group. Several of the most differentially expressed genes that are enriched in the RbV group are labeled in red. Gray line indicates the line of unity ($x = y$). **(B)** Dot plot of the top MSigDB hallmark gene sets that were significantly enriched and up-regulated in the RbV group (5% FDR, Benjamini-Hochberg correction, Normalized Enrichment Score > 0). Most of the significantly up-regulated genes are involved in immune response pathways such as interferon signaling and inflammation. **(C)** Bar plot showing the number of DE genes that were significantly changed (388 DE genes with Q value < 0.01 and $|\log_2$ fold-change| > 1). DE genes were either a part of global response programs (35 genes significant in ≥ 9 resident cell types) or cell type-specific responses (204 genes significant in 1 of 12 resident cell types). **(D)** Number of Reactome pathways that are either up-regulated (blue) or down-regulated (red) in the RbV group compared to controls. Microglia showed the largest number of up-regulated pathways (96 up-regulated, 61 down-regulated). Most cell types exhibited a net down-regulation of gene expression, with the largest down-regulation in neurons (28 up-regulated, 148 down-regulated). **(E)** Dot plot showing Reactome pathways that are altered in resident cell types. The size of each dot represents the number of genes in each cell type (columns), and the color of each dot indicates the normalized enrichment score of each pathway (rows). Pathways that were not significantly enriched (Q value ≥ 0.05 , Benjamini-Hochberg correction) are not displayed.

Figure 3.4 (Continued)

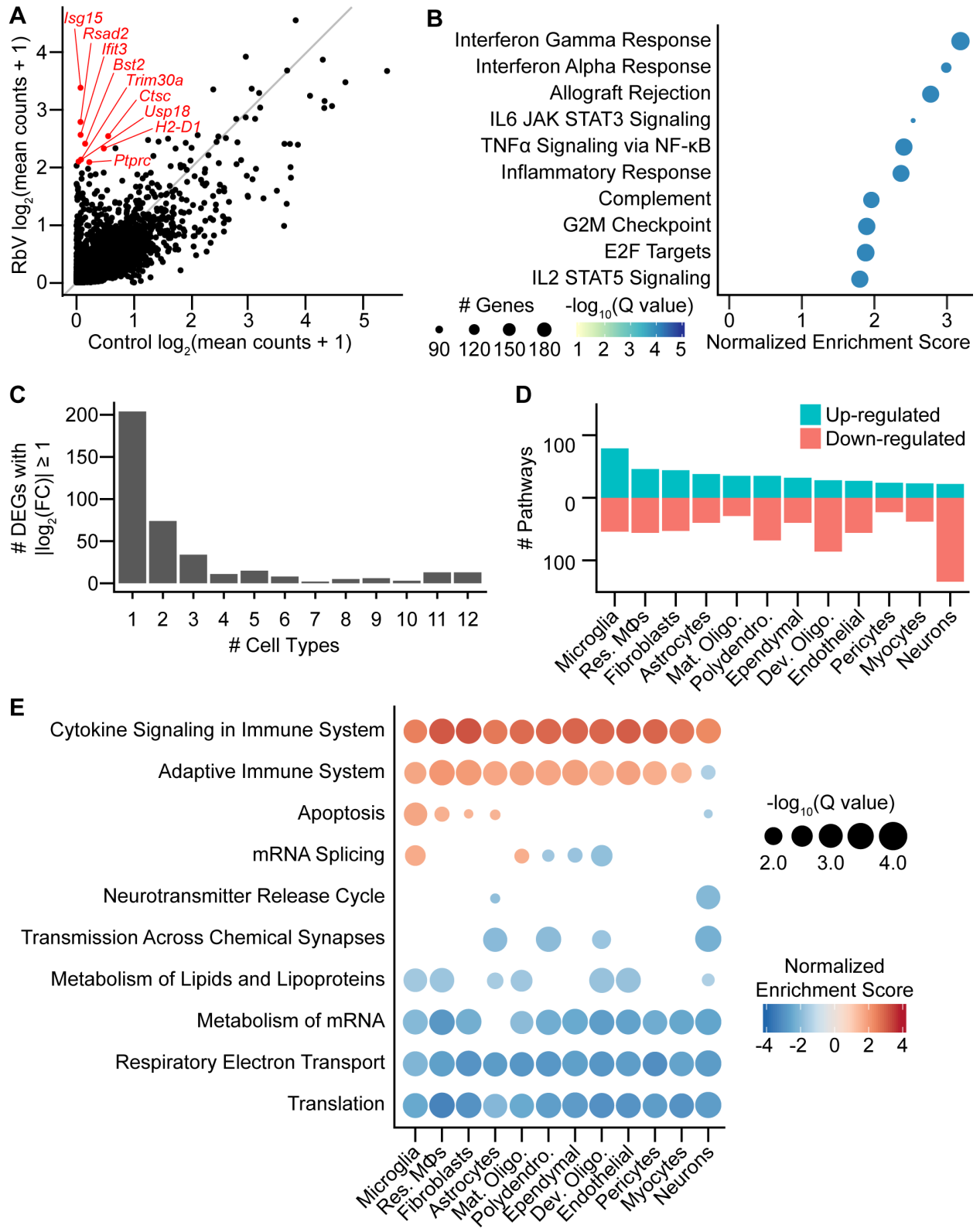
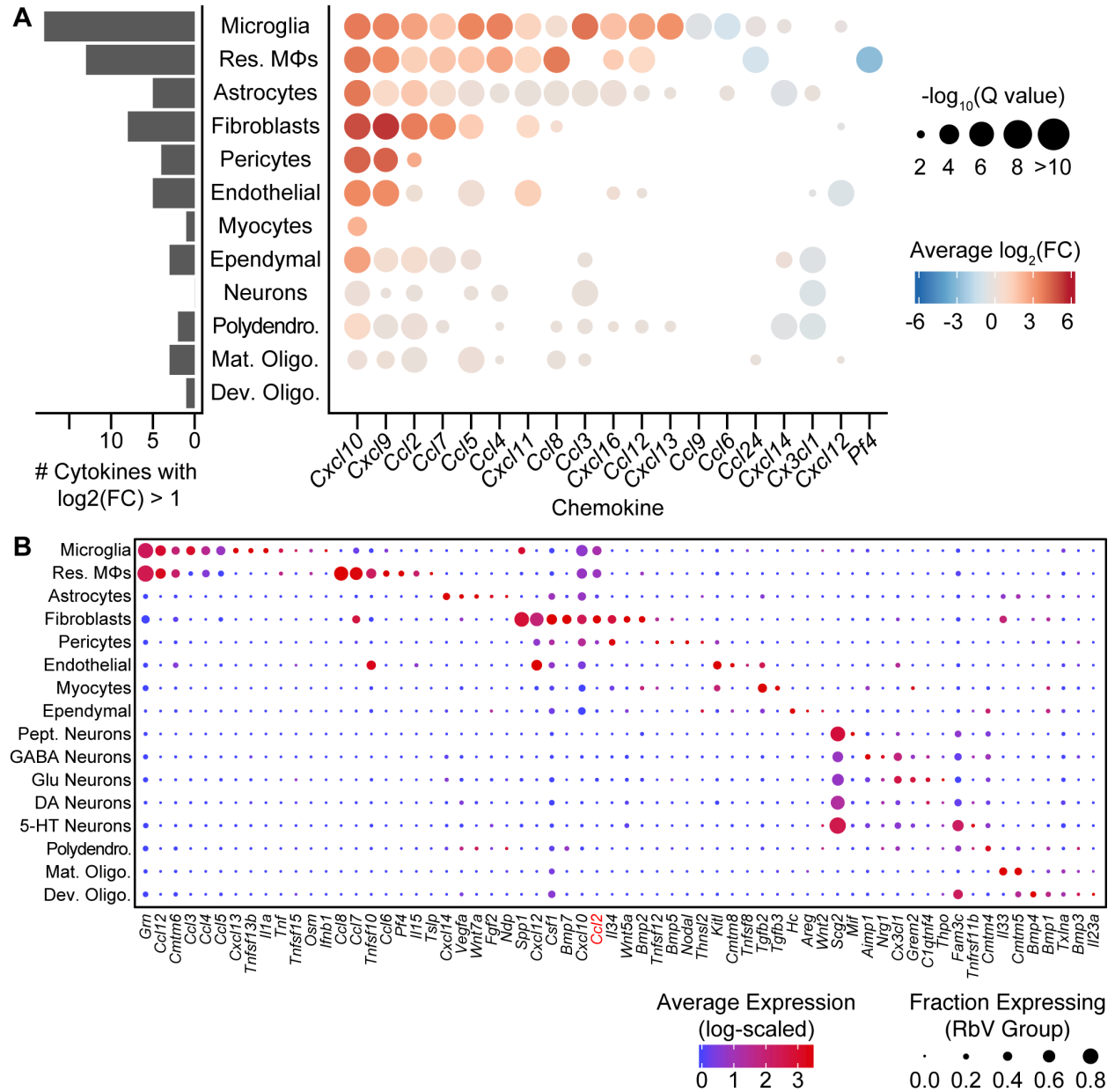


Figure 3.5: Cell type-specific expression of cytokines.

(A) Left: Bar plot showing the number of significantly up-regulated cytokines (average \log_2 fold-change > 1) in each resident cell type. Microglia and Res. M Φ s show the largest increase in cytokine release, whereas neurons and oligodendrocytes show the least increase in cytokine production. **Right:** Dot plot showing the cell type-specific changes in differentially expressed chemokines. The color of each dot represents the average \log_2 fold-change for each cell type cluster, and the size of the dot is scaled by the negative \log_{10} of the adjusted P values (Q values, Benjamini-Hochberg correction). Points in which a gene was not considered differentially expressed for a given cell type (Q value ≥ 0.01) are not displayed.

(B) Dot plot showing expression of selected cytokine genes (columns) by cell type (rows). The color of each dot represents the average log-scaled expression of each gene in a given cell type, and the size of each dot represents the fraction of cells of that type in which transcripts for that gene were detected.

Figure 3.5 (Continued)



To identify the cell types and signaling molecules mediating the recruitment of infiltrating leukocytes, we sorted DE genes based on their gene ontology annotations to find differentially expressed cytokines and chemokines. Microglia and resident MΦs showed the highest increase in cytokine expression compared to other resident cell types (Figure 3.5A). Cell types of the neurovascular unit, which include endothelial cells, astrocytes, pericytes, and fibroblasts/fibroblast-like cells, and ependymal cells at the interface with the ventricular system showed the next highest increase in cytokine production. Neurons showed the least increase in cytokine release. Several pro-inflammatory chemokines, such as *Cxcl9*, *Cxcl10*, *Ccl2*, *Ccl5*, and *Ccl7*, were released by multiple cell types. Most cell types in the RbV group released a distinct set of cytokines (Figure 3.5B), with fibroblasts expressing the largest set of cytokines. In contrast to a recent study using a “viral déjà vu” model (Di Liberto et al., 2018), we did not detect *Ccl2* expression in neurons (Figure 3.5B, highlighted in red). We speculate that this may be due to a difference in the models used – our study examines changes that occur during the primary responses on first encounter with the virus, whereas the “viral déjà vu” model is suited for investigating secondary responses.

Infiltrating leukocytes are transcriptionally diverse

To identify the types of immune cells involved in the response to RbV infection, we performed subclustering on the immune cell subset (Figure 3.6A, Figure 1.1A). Infiltrating leukocytes were separated into two main groups that were of either myeloid or lymphoid lineage. Iterative subclustering resolved the lymphoid cell cluster into at least 3 distinct types. T cells (*Cd3g*, *Cd3e*) were comprised of both CD8⁺ effector T cells (*Cd8a*, *Cd8b1*, *Tcf7*, *Prf1*, *Gzma*), and a smaller number of CD4⁺ helper T cells (*Cd4*, *Il2ra*, *Ctla4*). Natural killer (NK) cells were also

present in the lymphoid group and were identified by their expression of genes such as *Klre1*, *Prfl*, and *Gzma*. Non-resident myeloid cells were transcriptionally heterogeneous, and were comprised of several populations that were distinct from both of the resident myeloid cell types (Figure 3.7A-I). The majority of non-resident myeloid cells were monocytes (*Ccr2*, *Fn1*, *Plac8*, *Lyz2*, *Ly6c2*^{lo/mid}) and monocyte-derived macrophages (moMΦs) (*Ly6c2*^{hi}, *Nr1h3*, *Ly6a*, *H2-Aa*, *Ms4a6d*, *Cd74*). Several distinct clusters of dendritic cells (DCs) were also identified, which included monocyte-derived dendritic cells (moDCs) (*Il1b*, *Il1dr1*, *H2-Aa*, *Cd74*, *Ifitm1*), conventional dendritic cells (cDCs) (*Ccr7*, *Il4i1*, *Cd74*, *Cacnb3*), and plasmacytoid dendritic cells (pDCs) (*Ly6d*, *Siglech*, *Irf8*, *Runx2*).

Since genes involved in immune processes are increasingly associated with Alzheimer's Disease (AD), we assessed the expression of several AD-associated genes by cell type (Figure 3.7J). While several genes such as *App* were enriched in neurons, AD-associated genes involved in immune processes were expressed in specific cell types. *Trem2* was specifically expressed in microglia, whereas genes in the *Ms4a* family (e.g. *Ms4a7*, *Ms4a6c*) were primarily expressed by both resident MΦs and infiltrating moMΦs. *Ms4a4b* was also expressed in infiltrating lymphocytes. Resident MΦs also expressed high levels of *ApoE* in addition to astrocytes. Several AD-associated genes were also differentially expressed between the RbV and Control groups. We observed a decrease in *Trem2* and *Cd33* expression in response to RbV infection, whereas expression of MHC class I genes (*H2-Eb1*) and *Ms4a* genes were increased.

Figure 3.6: Type I interferon responses are induced by IFN β from microglia.

(A) UMAP plot of the immune cell subset. Individual points represent single cells, which are color coded by their assigned cell type identity. (B) UMAP feature plot showing *Ifnb1* expression, where the color of each cell represents the log-scaled UMI counts. *Ifnb1* transcripts are only detected in a small subset of microglia. (C) UMAP feature plot for *Ifng* expression. CD4⁺ T cells are the primary source of *Ifng*. (D) Dot plot showing the expression of selected cytokine genes (columns) in each immune cell type (rows). The dot color represents the average log-scaled expression of each gene in a given cell cluster, and the size of the dot represents the fraction of cells in that cluster in which transcripts for that gene were detected. Many cytokines are released by specific cell types. Monocytes/moMΦs, moDCs, and cDCs showed similarities in expression of several cytokines including *Ccl5*, *Cxcl9*, and *Cxcl10*. *Ifnb1* (microglia), which is expressed in a small subset of microglia, and *Ifng* (CD4⁺ T cells) are highlighted in red.

Figure 3.6 (Continued)

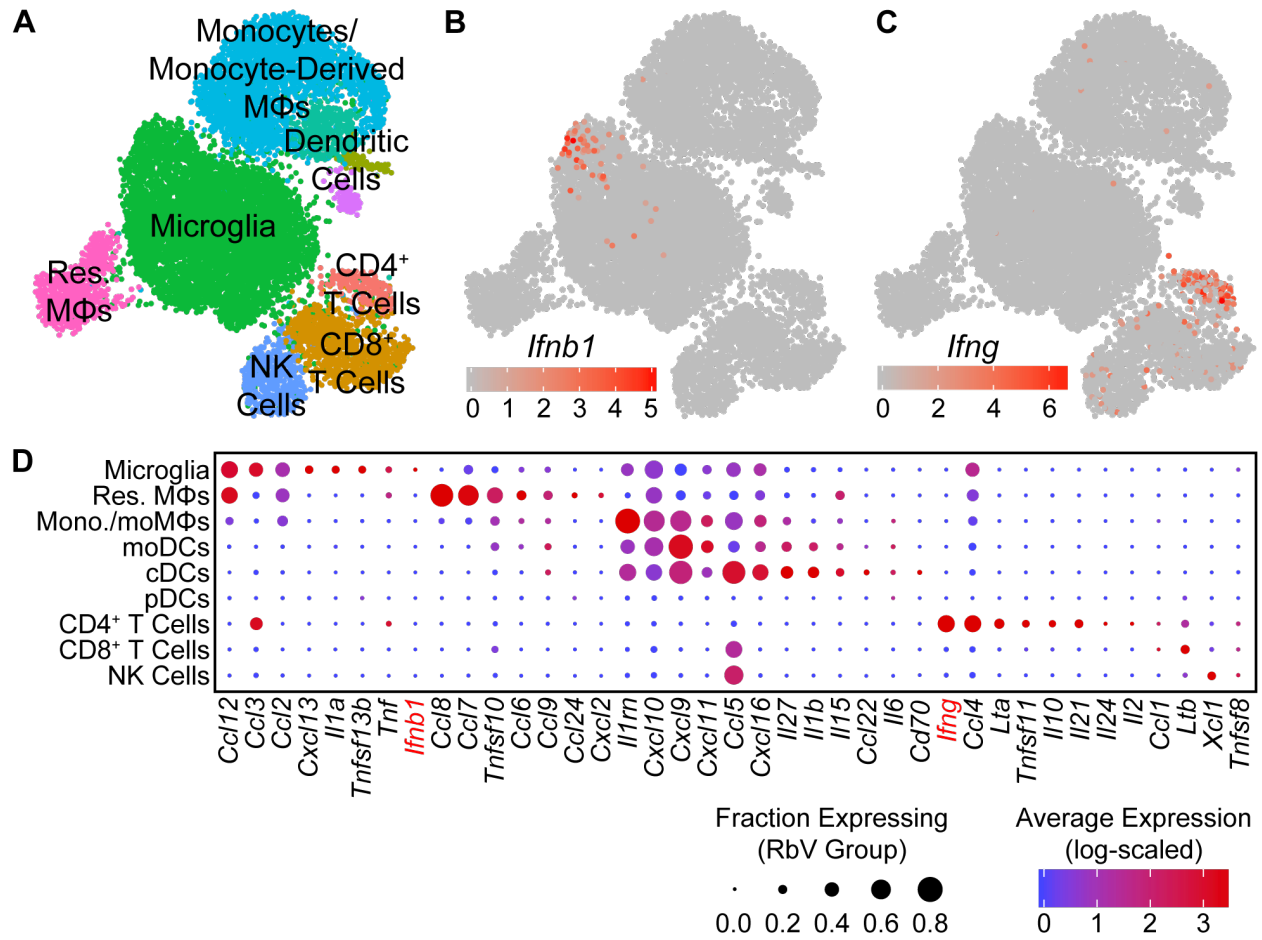


Figure 3.7: Identification of immune cell clusters.

(A) Dot plot showing expression of several example genes (rows) used for identifying immune cell clusters (columns). Combinations of several genes were used to identify each cell type given the overlaps and continuous variation in expression of many genes between different immune cell types. **(B-I)** UMAP feature plots showing the expression of several genes that are differentially expressed between non-resident myeloid cell types. Each cell is color-coded by its log-scaled expression for the indicated gene. **(J)** Paired dot plot showing expression of several genes associated with Alzheimer's Disease (rows), separating by cell type (columns) and condition (sub-columns: C – Control; R – RbV). *ApoE* expression was enriched in astrocytes and resident MΦs, while *Trem2* is specifically expressed in microglia. Resident MΦs and monocytes/moMΦs showed the highest expression of genes in the *Ms4a* gene group. *Trem2* expression decrease in microglia in the RbV group relative to Control, while expression of most *Ms4a* genes, except for *Ms4a7*, increase in the RbV condition.

Type I interferon responses are mediated by release of IFN β from microglia

To identify the primary mediators of the antiviral transcriptional responses, we assessed expression of interferons in each cell type. Of the genes encoding type I or II interferons, only transcripts for *Ifnb1* and *Ifng* were detected in our dataset. *Ifnb1* expression was restricted to a small subset of microglia (Figure 3.6B), while *Ifng* was expressed at high levels by CD4⁺ T cells, and at lower levels by CD8⁺ T cells (Figure 3.6C). Surprisingly, genes for IFN α were not detected in any cells, despite the presence of pDCs that are typically the main source of type I interferons in the periphery (Fitzgerald-Bocarsly et al., 2008). These results are consistent with previous reports of IFN β production from microglia to limit viral spread (Drokhlyansky et al., 2017). However, our results contrast with previous reports that identified astrocytes as the primary source of IFN β (Pfefferkorn et al., 2016), which may be due to differences in the methods used to identify IFN β -producing cells. Given the low rate in which RbV-infected cells were detected, we are unable to rule out expression of IFN α/β from infected neurons.

In addition to interferons, many other cytokines were also differentially expressed between immune cell types (Figure 3.6D). The pro-inflammatory cytokine *Il1a* was expressed specifically in microglia, whereas *Il1b* was expressed in cDCs and moDCs. Infiltrating myeloid cells expressed high levels of several pro-inflammatory cytokines, including *Ccl5* and *Cxcl9*. Microglia, resident M Φ s, and CD4⁺ T cells also expressed *Tnf*, which may facilitate leukocyte infiltration via its effects on neurovascular cells and the blood brain barrier (Chen et al., 2019; Shrestha et al., 2008). Other members of the TNF superfamily were also expressed in a different cell types, including *Tnfsf10* in resident M Φ s and monocytes/monocyte-derived cells, *Ltb* in T cells, and *Tnfsf11* in CD4⁺ T cells. Several anti-inflammatory cytokines were also expressed by

specific cell types: *Il10* was expressed specifically in CD4⁺ T cells, whereas the IL-1 receptor antagonist gene *Il1rn* was expressed by microglia and several infiltrating myeloid cell types.

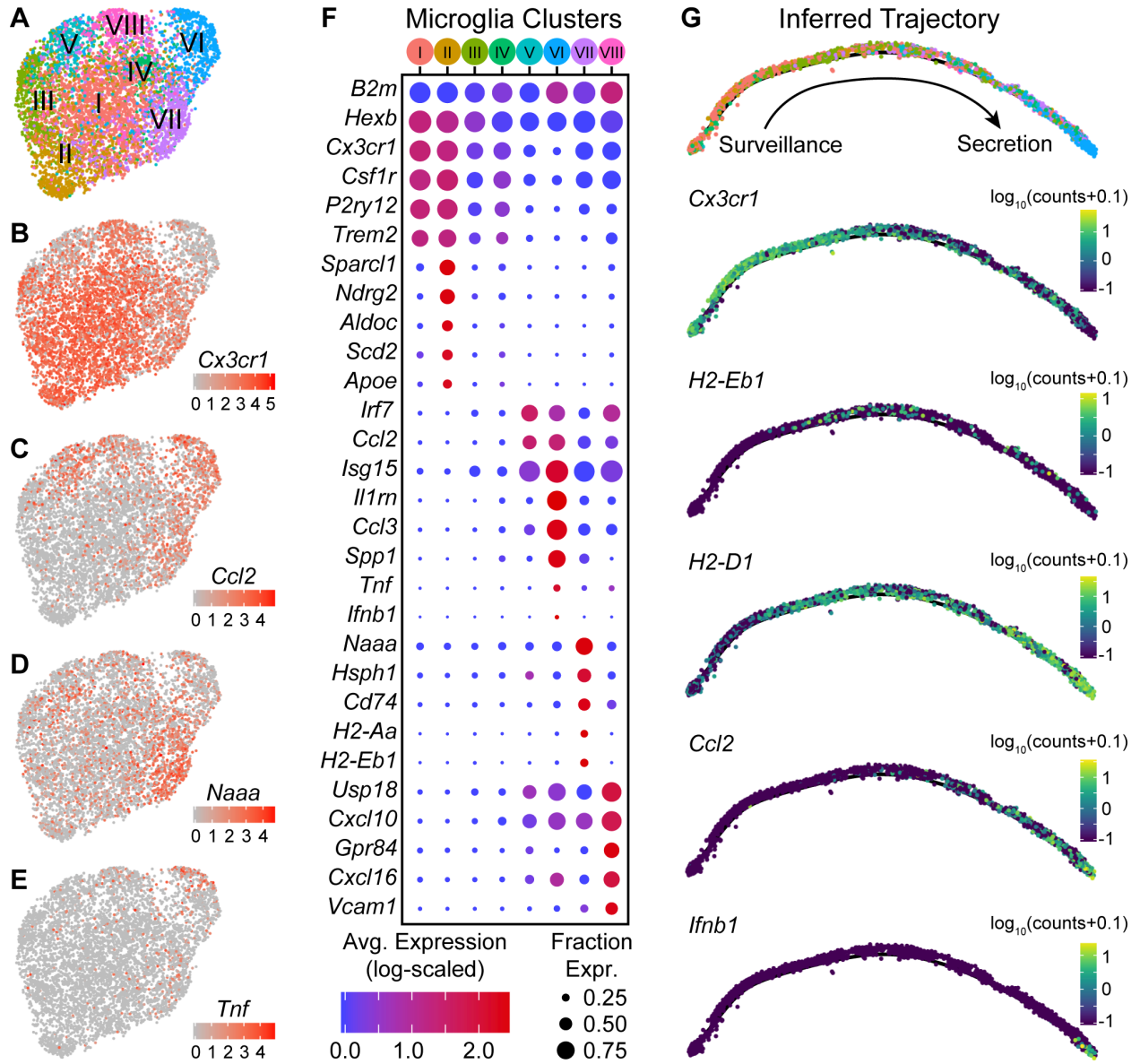
Microglia occupy distinct states along an activation trajectory

Since microglia had the highest number of up-regulated DE genes and pathways in response to the RbV infection, we performed subclustering on the microglial subset to determine if there are transcriptionally distinct states or subtypes of activated microglia. Subclustering using algorithms based on the shared nearest-neighbors (SNN) graph divided microglia into at least 7 distinct subclusters (Figure 3.8A). Subclusters differed in their proportion of cells from groups separated by condition (RbV / Control) and injection sites (Uninjected / Str-dLGN / NAc-SN). Subclusters that had a higher proportion of cells from the Control group included subclusters I (77.0% in Uninjected; 12.5% in Str-dLGN; 10.4% in NAc-SN) and subcluster II (79.5% in Uninjected; 14.5% in Str-dLGN; 6.0% in NAc-SN). Subclusters with microglia primarily from the RbV group included subclusters V (1.0% in Uninjected; 22.4% in Str-dLGN; 76.6% in NAc-SN), VI (0.3% in Uninjected; 3.2% in Str-dLGN; 96.4% in NAc-SN), VII (0.5% in Uninjected; 12.0% in Str-dLGN; 87.5% in NAc-SN), and VIII (0.3% in Uninjected; 91.6% in Str-dLGN; 8.1% in NAc-SN). Subcluster III (13.2% in Uninjected; 69.8% in Str-dLGN; 17.0% in NAc-SN) and subcluster IV (59.3% in Uninjected; 6.5% in Str-dLGN; 34.2% in NAc-SN) showed intermediate proportions between RbV and Control groups.

Figure 3.8: Microglia are found in distinct transcriptional states along an activation trajectory.

(A) UMAP plot showing sub-clusters of microglia found using SNN graph-based clustering (see Methods). Points are single cells color-coded by sub-cluster assignment. (B-E) UMAP feature plots showing expression of genes that are differentially expressed between microglia sub-clusters. Cells are color-coded by their log-scaled UMI counts for a given gene. (F) Dot plot showing expression of several genes (rows) that are differentially expressed between microglia sub-clusters (columns – color-coded according to Panel A1). Genes expressed across all sub-clusters include *Hexb* and *B2m*. Genes commonly used to identify “resting” microglia, such as *Cx3cr1* and *Csf1r*, are down-regulated in several sub-clusters and anti-correlated with expression of interferon-stimulated genes, such as *Isg15*, and chemokine genes, such as *Ccl2* and *Cxcl10*. Sub-clusters V-VIII that are high in *Isg15* expression showed differential expression of several genes including MHC I genes (*H2-Aa*, *H2-Eb1*) and cytokines (*Tnf*, *Ifnb1*), suggestive of functional differences between sub-clusters of activated microglia. (G) Inferred trajectory of microglial activation. Genes that were differentially expressed between microglia sub-clusters were used for constructing the minimum spanning tree (see Methods). The inferred graph was comprised of 2 nodes connected by a single edge/trajectory along which the cells are arranged (individual points). **Top:** Cells are color-coded by sub-clusters, following the color scheme in Panel A1. Cells from sub-clusters I-II are on the left-most end of the trajectory, while cells from sub-cluster VI are on the opposite end. The remaining sub-clusters were distributed along the middle of the inferred trajectory. **Middle/Bottom:** Inferred graphs with cells color-coded by their log₁₀-transformed expression of several genes that are differentially expressed between microglia sub-clusters.

Figure 3.8 (Continued)



Differential expression tests between subclusters showed that they differ in expression of various genes that include genes that are typically used as “markers” for microglia such as *Cx3cr1*, *Csf1r*, *P2ry12*, and *Trem2* (Figure 3.8B-F). Subclusters I and II had the highest expression of these canonical “marker” genes, and are likely to be microglia in a “resting” or surveillance state. Expression of these canonical “marker” genes was lower in the remaining subclusters and anti-correlated with expression of interferon-stimulated genes such as *Isg15* (all microglia, *Cx3cr1* vs. *Isg15*, Pearson R = -0.56). Subclusters VII, VIII, V, and VI express progressively lower levels of *Cx3cr1* (in the stated order), and instead expressed *Isg15*, *Irf7*, and *Ccl2* at higher levels. Between subclusters V-VIII, genes involved in different immunological processes such as antigen presentation (e.g. *Cd74*, *H2-Aa*, *H2-Eb1*) and cytokine secretion (e.g. *Ifnb1*, *Tnf*) are differentially expressed, suggesting that these subclusters are functionally distinct.

To assess whether subclusters V-VIII reflect distinct states or subtypes of microglia, we used trajectory inference methods based on the genes that are differentially expressed between the subclusters (Trapnell et al., 2014; Qiu et al., 2017). We hypothesized that branch points in the inferred trajectory/graph would suggest that these subclusters define distinct activation endpoints for microglia and diversification of activated microglia, whereas an unbranched trajectory with a single edge/path would instead suggest that the subclusters define discrete states along a continuous trajectory and describe the transitional states that can be occupied through several stages of microglial activation. The graph that was constructed from the microglia transcriptomic data suggested that the subclusters lie along an unbranched trajectory (Figure 3.8G). Subclusters I and II that express high levels of *Cx3cr1* and *P2ry12* were enriched on one extreme of the inferred trajectory, and describe the “resting” or surveilling state of microglia. Subcluster VIII

cells that re enriched for genes involved in antigen presentation, such as *Cd74* and *H2-Eb1*, were densest in the middle of the trajectory where there is also an increase in expression of interferon response genes such as *Isg15*. Subcluster VI cells, which are enriched in expression of cytokines such as *Ccl2*, *Tnf*, and *Ifnb1*, was found at the other extreme of the trajectory, and describe a secretory state. Given the higher abundance of infiltrating lymphocytes in the NAc-SN group (majority of subcluster VI microglia) compared to the Str-dLGN (majority of subcluster VIII microglia), we speculate that the transition of microglia from an antigen presentation state the middle of the inferred activation trajectory to the secretory state may be mediated by interactions between microglia and T cells.

RbV infection alters the structure of intercellular interactions in the DRN

To assess changes in intercellular communication between specific cell types induced by the immune response, we used *cellphoneDB* to predict significant interactions between the various cell types from our scRNA-seq data (Vento-Tormo et al., 2018; Efremova et al., 2019).

Significant interactions were assessed for RbV and Control groups separately (Figure 3.9), and the difference between the two was used to infer changes in intercellular interactions (Figure 3.10). Interactions among resident cell types under control conditions were highest between fibroblasts and cells of the neurovascular unit, although we anticipate that the number of interactions we infer here is likely to be an underestimate since the analysis package may not include interactions mediated by neurotransmitter release. A comparison of interactions between RbV and Control groups showed an overall decrease in intercellular communication between most resident cell types. Interactions with infiltrating cell types, such as monocytes and dendritic

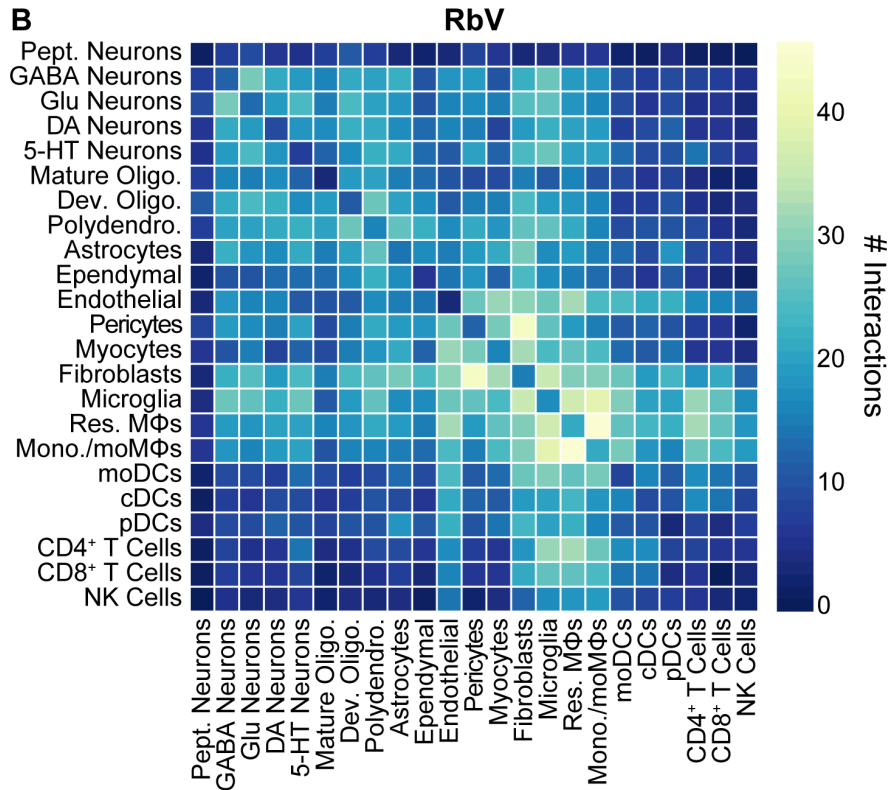
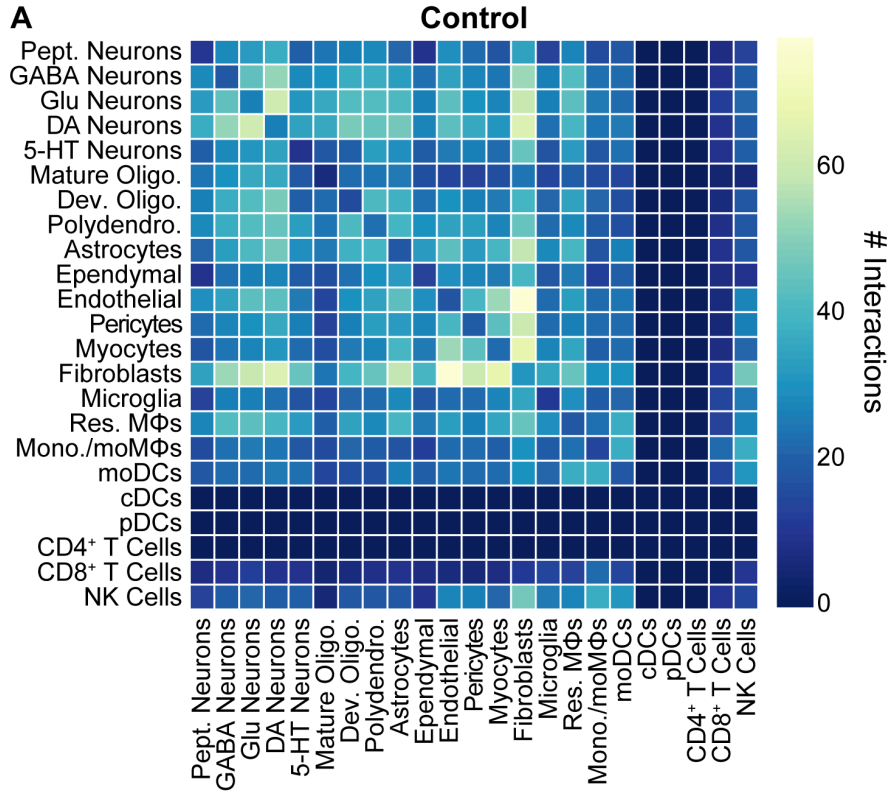
Figure 3.9: Number of inferred interactions between cell types by condition.

(A) Heatmap showing the number of inferred interactions between cell types in the control group.

Fibroblasts have the highest number of interactions with other cells, consistent with the high number of cytokines expressed by these cells (Figure S3B). The color range is scaled to the maximum number of interactions between a pair of cell types in the Control group. Interaction counts are non-directional, and not weighted by cell type abundance. Interactions for cell types not present in the Control group (e.g.

dendritic cells) are at 0. **(B)** Heatmap showing the number of inferred interactions between cell types in the RbV group. Antigen-presenting cells, comprised of microglia, monocytes/moMΦs, and DCs, had the highest number of interactions. The color range is scaled to the maximum number of interactions between a pair of cell types in the RbV group.

Figure 3.9 (Continued)



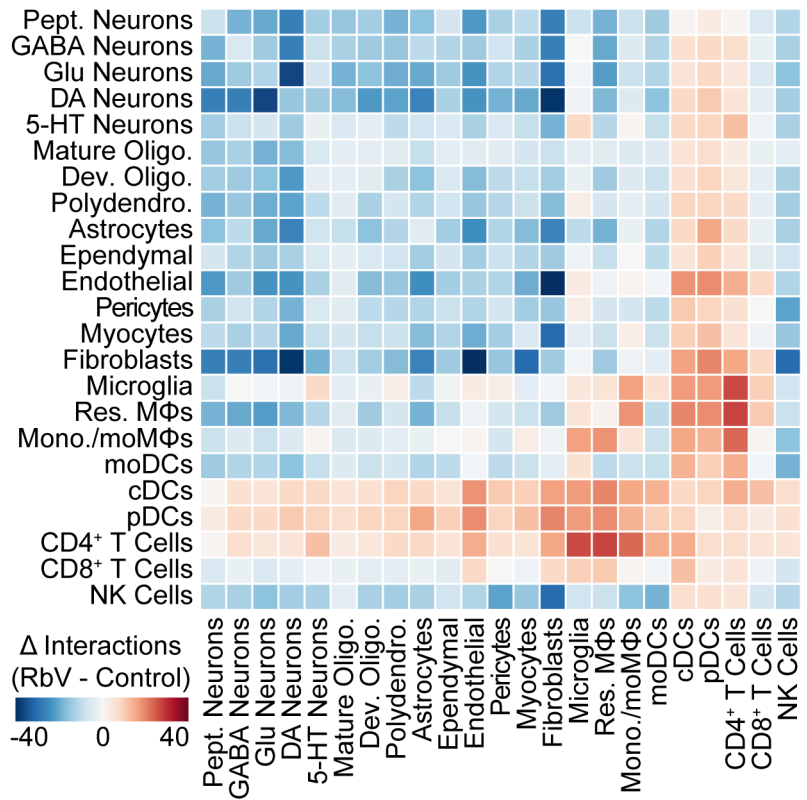


Figure 3.10: The structure of intercellular interactions is altered by the immune response.

Heatmap showing the change in the number of interactions between cell types (RbV - Control). Interactions were inferred from single cell expression data using *cellphoneDB*. Red colors indicate an increase in the number of interactions between a pair of cell types in the RbV group relative to Control, whereas blue colors indicate a decrease in the number of interactions. There was an overall decrease in interactions between resident cell types in the RbV group relative to Control group. Among neuronal types, 5-HT neurons showed the largest increase in interactions with microglia and CD4⁺ T cells. Resident MΦs and microglia had the highest number of interactions with CD4⁺ T cells.

cells, showed a large increase as expected from their relative absence in the Control group. Among the resident cell types, microglia and resident MΦs had the highest increase in interactions. In particular, microglia increased in their interactions with CD4⁺ T cells, consistent with our hypothesis that microglia-T cell interactions may be involved in the progression of microglia along the activation trajectory. Microglia also increased in the number of inferred interactions with 5-HT neurons relative to the other neuron types. We hypothesize that this may be indicative of increased interactions between microglia and RbV-infected neurons.

3.4 Discussion

Here we characterize both global and cell type-specific transcriptional responses in the CNS following neuronal infection by RbVs. We reveal the transcriptional diversity of both resident and infiltrating immune cells populations that mediate distinct aspects of the host antiviral defense mechanisms. These results also suggest that microglia and infiltrating T cells serve key roles in orchestrating the antiviral response via Type I and Type II interferon signaling. Our data also shows that cytokine signaling induced by viral infection leads to the down-regulation of metabolic processes and neurotransmission that may limit the spread of neurotropic viruses. We also describe transcriptionally distinct subsets of microglia that are likely to represent discrete transitional states along an activation trajectory during the progression of the immune response. Additionally, we outline the changes in cell type-specific intercellular interactions involved in different aspects of the multifaceted response, which led to our prediction that helper T cells may mediate the progression of microglia along an activation trajectory. Our study provides additional insights into the distinct immunological functions of various cell types in the brain, and presents several testable models and hypotheses for experimental validation in future studies.

Transcriptional heterogeneity among resident and infiltrating immune cells

An advantage of using scRNA-seq in this study has been the use of the transcriptome to assign and identify cells into distinct classes, types, and states. Despite the relatively low sequencing depth that we incur with the use of high-throughput droplet-based methods, our dataset captures variations across more dimensions than “conventional” techniques such as immunolabeling and *in situ* hybridization. The use of the transcriptome along with careful cross-referencing of gene expression signatures in cell clusters with well-validated studies also reduces biases in cell type identification or selection that may be introduced by the choice of markers. Consistent with other recent scRNA-seq studies, our results highlight potential biases introduced when using genes such as *Cx3cr1* for identifying microglia, since several of these genes are down-regulated in activated or disease-associated microglia (Jordão et al., 2019; Li et al., 2019; Masuda et al., 2019; Mrdjen et al., 2018).

In addition to resolving transcriptional differences between different immune cell types, our study also finds distinguishing gene expression features between distinct subclusters of microglia. While our results suggest that these subclusters represent discrete states along a single activation trajectory, we do not rule out the possibility of distinct activation endpoints for microglia in a branching trajectory. It is possible that these differences may emerge when comparing across a variety of stimuli (e.g. “viral déjà vu”, LPS, AD transgenic models, experimental autoimmune encephalomyelitis) that may trigger different response pathways and a distinct set of activation trajectories from what we have observed in our study. Additionally, our study only examines transcriptional changes at a single time point after initial exposure to the

virus, and may only capture a segment of microglial activation before the emergence of distinct endpoints. Future studies that systematically explore a full range of time points will help resolve the dynamics of these transcriptional responses. These studies will also clarify if the difference in leukocyte infiltration that we found to be correlated with the infection magnitude reflects a difference in the immune response, or a change in the time course of a shared response. Deeper sequencing and datasets containing a larger collection of microglia may also help resolve finer levels of heterogeneity among lower-expressing genes.

Spatial specificity and inter-regional variability in immune responses

While our study describes transcriptional changes in CNS resident cells, it is also plausible that immune responses in various brain regions may exhibit differences. These could be due to the varying composition of resident cells, even among closely related types. For instance, resident MΦs in the DRN express the serotonin receptor *Htr1b*, which was not detected in resident MΦs in the cortex, striatum, or ventral midbrain (Huang et al., 2019; Saunders et al., 2018).

Interregional variation in immune signaling may also result from differences in the proximity of different locations to neurovascular or ventricular features. The DRN is also situated in close proximity to the cerebral aqueduct, as well as larger blood vessels in the ventrolateral periaqueductal gray that run along the anterior-posterior axis. Future studies comparing the responses in various regions (e.g. frontal cortex versus DRN) may reveal shared immune mechanisms across the CNS, and may also identify specific brain regions that are particularly susceptible to immunological insults that may subsequently trigger profound and long-lasting behavioral changes. Studies profiling these responses in different brain regions from the same animal may also distinguish systemic from local or region-specific effects. Although the

injection sites in our study are over 1 mm away from the DRN, previous studies have shown increases in ISG expression in the cerebellum following infection of the olfactory bulb (van den Pol et al., 2014). This also provides a plausible reason for the absence of IFN α -expressing cells in our dataset. Since this study does not examine changes occurring at the injection sites or in regions devoid of RbV-infected neurons, we are unable to distinguish the effects of systemic signaling on the transcriptional responses that we describe here.

Identification of virally labeled neurons with scRNA-seq

Many recent studies have used scRNA-seq to build a detailed atlas of the diverse cell types that exist in the CNS. Relating the molecular profile of each cell type to its anatomical location and axonal projections remains one of the main challenges in placing each of these cell types into neural circuits for functional studies, with the lower throughput of most anatomical tracing techniques being a major limiting factor. Methods for combining next-generation sequencing with connectivity mapping have therefore been of great interest, and several recently developed methods have used neurotropic viruses to either label cells for sorting and enrichment of transcripts from a projection-defined neuronal population (Ekstrand et al., 2014; Tasic et al., 2018), or the introduction of barcodes for reconstruction of neuronal connectivity from sequencing data (Kebschull et al., 2016; Oyibo et al., 2018). RbVs have been valuable tools in the study of neural connectivity since they can be used for cell type-specific transsynaptic retrograde tracing, which provides more specificity in the identity of the postsynaptic cell than conventional tracers (Wickersham et al., 2007). While our study provides evidence further cautioning against the use of the SAD B19 strain for functional studies as previously described (Reardon et al., 2016; Chatterjee et al., 2018), we find that cells with high expression of RbV

transcripts still retain sufficient transcriptional information for their classification into a specific cell type. Our results therefore support the feasibility of the use of RbVs for connectivity mapping between single cells using high-throughput sequencing methods. Although the detection of RbV-infected neurons was sparse in our dataset, limitations in the yield of RbV-labeled neurons for connectivity inference and network reconstruction can be overcome through the addition of methods to enrich for both RbV-labeled cells, such as FACS, and RbV transcripts during library preparation. Future studies comparing the immune responses elicited by different viruses or virus strains used for neuroscience research will also provide crucial insights into the effects of these tools on the physiological properties of the cell types and neural circuits of interest.

3.5 Materials and Methods

Mice

C57BL/6J (The Jackson Laboratory, Stock # 000664) were kept on a 12:12 regular light/dark cycle under standard housing conditions. All procedures were performed in accordance with protocols approved by the Harvard Standing Committee on Animal Care following guidelines described in the U.S. National Institutes of Health Guide for the Care and Use of Laboratory Animals.

Rabies Viruses

Unpseudotyped rabies viruses (B19G-SADΔG-EGFP, B19G-SADΔG-tdTomato) were generated in-house using procedures based on published protocols (Wickersham et al., 2010; Osakada and Callaway, 2013). Virions were amplified from existing stocks in three rounds of low-MOI passaging through BHK-B19G cells by transfer of filtered supernatant, with 3 to 4 days between passages. Cells were grown at 35 °C and 5% CO₂ in DMEM with GlutaMAX (Thermo Scientific, #10569010) supplemented with 5% heat-inactivated FBS (Thermo Scientific #10082147) and antibiotic-antimycotic (Thermo Scientific #15240-062). Virions were concentrated from media from dishes containing virion-generating cells by first collecting and incubating with benzonase nuclease (1:1000, Millipore #70664) at 37°C for 30 min, followed by filtration through a 0.22 μm PES filter. The filtered supernatant was transferred to ultracentrifuge tubes (Beckman Coulter #344058) with 2 ml of a 20% sucrose in dPBS cushion and ultracentrifuged at 20,000 RPM (Beckman Coulter SW 32 Ti rotor) at 4°C for 2 hours. The supernatant was discarded and the pellet was resuspended in dPBS for 6 hours on an orbital shaker at 4 °C before aliquots were prepared and frozen for long-term storage at -80 °C.

Unpseudotyped rabies virus titers were estimated based on a serial dilution method counting infected HEK 293T cells, and quantified as infectious units per ml (IU/ml).

Stereotaxic Surgeries

Mice were initially anesthetized with 5% isoflurane (80% oxygen) and maintained at 1-2.5% isoflurane after placement on the stereotaxic frame (David Kopf Instruments, Model 1900 Stereotaxic Alignment System). The scalp was cleaned and sterilized before an incision was made to expose the skull, and sterile ophthalmic ointment was applied to the eyes. For leveling the horizontal plane, a stereotaxic alignment tool (David Kopf Instruments, Model 1905) was used to zero the relative dorsoventral displacement of Bregma and Lambda, as defined in the Paxinos Brain Atlas (Paxinos and Franklin, 2001), for adjusting tilt of the anterior-posterior axis, and of two points equidistant to the left and right of Bregma for adjusting the tilt of the medial-lateral axis. Craniotomies were prepared using a mounted drill (David Kopf Instruments, Model 1911) with careful removal of the bone flap and overlying dura using forceps and a fine needle tip, and were covered with sterile 0.9% saline before and during the injection to prevent desiccation. Viruses were front-filled into a pulled glass pipette (Drummond Scientific, #5-000-2005) filled with mineral oil (Millipore Sigma, M3516) and connected to a 5 μ l Hamilton syringe (Hamilton #84850) via polyethylene tubing filled with mineral oil. Glass pipettes were pulled to obtain a tip size of approximately 40-60 μ m on a pipette puller (Sutter Instrument Co., P-97). Viruses were infused into target regions at approximately 100 nl/min using a syringe pump (Harvard Apparatus, #883015), and pipettes were slowly withdrawn (< 10 μ m/s) at least 10 min after the end of the infusion. Following wound closure, mice were placed in a cage with a heating pad until their activity was recovered before returning to their home cage. Mice were

given pre- and post-operative oral carprofen (MediGel CPF, 5mg/kg/day) as an analgesic, and monitored daily for at least 4 days post-surgery.

Stereotaxic Injection Coordinates and Volumes

All coordinates are relative to Bregma along the anterior-posterior axis and medial-lateral axis, and relative to the pial surface along the dorsoventral axis. “BL” denotes the distance between Bregma and Lambda. All injections used a straight vertical approach parallel to the DV (Z) axis. All injections were placed in the right hemisphere (positive ML values). Striatum (Str): AP = +0.40 mm, ML = ± 2.45 mm, DV = -3.10 mm, 300 nl. Dorsal lateral geniculate nucleus (dLGN): AP = $-(2.00 * BL / 4.20)$ mm, ML = +2.25 mm, DV = -3.00 mm, 150 nl. Substantia Nigra (SN): AP = $-(3.00 * BL / 4.20)$ mm, ML = +1.32 mm, DV = -4.60 mm, 150 nl.

Histology

Mice were deeply anesthetized with isoflurane and transcardially perfused with 5-10 ml chilled 0.1 M PBS, followed by 10-15 ml chilled 4% paraformaldehyde in 0.1 M PBS. Brains were dissected out and post-fixed overnight at 4 °C, followed by incubation in a storing/cryoprotectant solution of 30% sucrose and 0.05% sodium azide in 0.1 M PBS for at least 1-2 days to equilibrate. 50 μ m coronal slices were prepared on a freezing microtome (Leica Biosystems, SM2010 R). 50 μ m thick free-floating tissue sections were rinsed 3 x 5 min with 0.1 M PBS containing 0.5% Triton X-100 (PBST) before counterstaining with Neurotrace 435 (ThermoFisher Scientific N21479) at a concentration of 1:100 in 0.1 M PBS with 0.5% Triton X-100 for 1 hour at room temperature. Slices were rinsed 4 x 5 min with 0.1 M PBS before they were mounted on glass slides in VectaShield mounting media (Vector Labs, H-1000).

Fluorescence images were taken on an Olympus VS120 slide scanning microscope with a 10X air objective.

Single Cell Dissociation and RNA Sequencing

8- to 10-week old C57BL/6J mice were pair-housed in a regular 12:12 light/dark cycle room prior to tissue collection. Mice were transcardially perfused with an ice-cold choline cutting solution containing neuronal activity blockers (110 mM choline chloride, 25 mM sodium bicarbonate, 12 mM D-glucose, 11.6 mM sodium L-ascorbate, 10 mM HEPES, 7.5 mM magnesium chloride, 3.1 mM sodium pyruvate, 2.5 mM potassium chloride, 1.25 mM sodium phosphate monobasic, 10 μ M (R)-CPP, 1 μ M tetrodotoxin, saturated with bubbling 95% oxygen/5% carbon dioxide, pH adjusted to 7.4 using sodium hydroxide). Brains were rapidly dissected out and sliced into 250 μ m thick coronal sections on a vibratome (Leica VT1000) with a chilled cutting chamber filled with choline cutting solution. Coronal slices containing the dorsal raphe were then transferred to a chilled dissection dish containing a choline-based cutting solution for microdissection. Dissected tissue chunks were transferred to cold HBSS-based dissociation media (Thermo Fisher Scientific Cat. # 14170112, supplemented to final content concentrations: 138 mM sodium chloride, 11 mM D-glucose, 10 mM HEPES, 5.33 mM potassium chloride, 4.17 mM sodium bicarbonate, 2.12 mM magnesium chloride, 0.9 mM kynurenic acid, 0.441 mM potassium phosphate monobasic, 0.338 mM sodium phosphate monobasic, 10 μ M (R)-CPP, 1 μ M tetrodotoxin, saturated with bubbling 95% oxygen/5% carbon dioxide, pH adjusted to 7.35 using sodium hydroxide) supplemented with an additional inhibitor cocktail (10 μ M triptolide, 5 μ g/ml actinomycin D, 30 μ g/ml anisomycin) and kept on ice until dissections were completed. The remaining tissue was fixed in 4% paraformaldehyde in

phosphate-buffered saline for histological verification. Dissected tissue chunks for each sample were pooled into a single tube for the subsequent dissociation steps. Tissue chunks were first mixed with a digestion cocktail (dissociation media, supplemented to working concentrations: 20 U/ml papain, 1 mg/ml pronase, 0.05 mg/mL DNase I, 10 μ M triptolide, 5 μ g/ml actinomycin D, 30 μ g/ml anisomycin) and incubated at 34 °C for 90 min with gentle rocking. The digestion was quenched by adding dissociation media supplemented with 0.2% BSA and 10 mg/ml ovomucoid inhibitor (Worthington Cat. # LK003128), and samples were kept chilled for the rest of the dissociation procedure. Digested tissue was collected by brief centrifugation (5 min, 300 g), re-suspended in dissociation media supplemented with 0.2% BSA, 1 mg/ml ovomucoid inhibitor, and 0.05 mg/mL DNase I. Tissue chunks were then mechanically triturated using fine-tip plastic micropipette tips of progressively decreasing size. The triturated cell suspension was filtered in two stages using a 70 μ m cell strainer (Miltenyi Biotec Cat # 130-098-462) and 40 μ m pipette tip filter (Bel-Art Cat. # H136800040) and washed in two repeated centrifugation (5 min, 300 g) and re-suspension steps to remove debris before a final re-suspension in dissociation media containing 0.04% BSA and 15% OptiPrep (Sigma D1556). Cell density was calculated based on hemocytometer counts and adjusted to approximately 100,000 cells/ml. Single-cell encapsulation and RNA capture on the InDrop platform was performed at the Harvard Medical School ICCB Single Cell Core using v3 hydrogels based on previously described protocols (Zilionis et al., 2017). Suspensions were kept chilled and gently agitated until the cells were flowed into the microfluidic device. Libraries were prepared and indexed following the protocols referenced above, and sequencing-ready libraries were stored at -80 °C. Libraries were pooled and sequenced on an Illumina NextSeq 500 (High Output v2 kits).

Sequencing Data Processing

NGS data was processed using previously a published pipeline in Python available at [<https://github.com/indrops/indrops>] (Klein et al., 2015). Briefly, reads were filtered by expected structure and sorted by the corresponding library index. Valid reads were then demultiplexed and sorted by cell barcodes. Cell barcodes containing fewer than 250 total reads were discarded, and remaining reads were aligned to a reference mouse transcriptome (Ensembl GRCm38 release 87) using Bowtie 1.2.2 ($m = 200, n = 1, l = 15, e = 100$). For alignment, the mouse transcriptome was modified with the addition of genes from the SAD B19 rabies viruses and transgenes (*B19N*, *B19P*, *B19M*, *B19L*, *EGFP*, *tdTomato*, *AmCyan1*). Aligned reads were then quantified as UMI-filtered mapped read (UMIFM) counts. UMIFM counts and quantification metrics for each cell were combined into a single file sorted by library and exported as a gunzipped TSV file.

Pre-Clustering Filtering and Normalization

Analysis of the processed NGS data was performed in R version 3.4.4 using the *Seurat* package version 2.3.1 (Satija et al., 2015; Butler et al., 2018). A custom R script was used to combine the expression data and metadata from all libraries corresponding to a single batch, and cells with fewer than 500 UMIFM counts were removed. The expression data matrix (Genes x Cells) was filtered to retain genes with > 5 UMIFM counts, and then loaded into a *Seurat* object along with the library metadata for downstream processing. The percentage of mitochondrial transcripts for each cell (*percent.mito*) was calculated and added as metadata to the *Seurat* object. Cells were further filtered prior to dimensionality reduction (*Reads* – *min.* 20000, *max.* *Inf*; *nUMI* – *min.* 500, *max.* 18000; *nGene* – *min.* 200, *max.* 6000; *percent.mito* – *min.* *-Inf*, *max.* 0.1). Low quality libraries identified as outliers on scatter plots of quality control metrics (e.g. unusually low

gradient on the nGene vs. nUMI) were also removed from the dataset. Expression values were then scaled to 10,000 transcripts per cell and log-transformed. Effects of latent variables (*nUMI*, *percent.mito*, *Sex*) were estimated and regressed out using a GLM (*ScaleData* function, *model.use = "linear"*), and the scaled and centered residuals were used for dimensionality reduction and clustering.

Dimensionality Reduction and Batch Effect Correction

Canonical correlation analysis (CCA) was used for dimensionality reduction and mitigation of batch effects. We used 2,412 genes that were highly variable in at least 2 datasets to calculate canonical variates (CVs) using the *RunMultiCCA* function in *Seurat*. After inspection of the CVs, the first 21 CVs were used for subspace alignment using the *AlignSubspace* function to merge datasets into a single object.

Cell Clustering and Cluster Identification

Initial clustering was performed on the merged and CCA-aligned dataset using the first 21 aligned CVs. UMAP was used only for data visualization. Clustering was run using the *FindClusters* function using the SLM algorithm and 10 iterations. Clustering was performed at varying resolution values, and we chose a value of 2 for the resolution parameter for the initial stage of clustering. Clusters were assigned preliminary identities based on expression of combinations of known marker genes for major cell classes and types. Low quality cells were identified based on a combination of low gene counts, low UMIFM counts, high fraction transcripts from mitochondrial genes, and a high fraction of nuclear transcripts (e.g. *Malat1*, *Meg3*, *Kcnq1ot1*). These cells typically clustered together and were removed manually.

Following assignment of preliminary identities, cells were divided into data subsets as separate *Seurat* objects (neurons; astrocytes; ependymal cells; endothelial cells, pericytes, fibroblasts, and myocytes; immune cells; oligodendrocytes and polydendrocytes) for further subclustering.

Subclustering

Subclustering was performed iteratively on each data subset to resolve additional cell types and subtypes. For immune cell types with proliferating cell populations (microglia, lymphocytes), cell cycle scores were calculated and regressed out using the *ScaleData* function in *Seurat*.

Briefly, clustering was run at high resolution, and the resulting clusters were ordered in a cluster dendrogram built using the Ward2 method in *hclust* using cluster-averaged gene expression for calculating the Euclidean distance matrix. Putative doublets/multiplets were identified based on expression of known marker genes for different cell types not in the cell subset (e.g. neuronal and glial markers). Putative doublets tended to separate from other cells and cluster together, and these clusters were removed from the dataset. Cluster separation was evaluated using the *AssessNodes* function and inspection of differentially expressed genes at each node. Clusters with poor separation, based on high OOBE scores and differential expression of mostly housekeeping genes, were merged to avoid over-separation of the data. The dendrogram was reconstructed after merging or removal of clusters, and the process of inspecting and merging or removing clusters was repeated until all resulting clusters could be distinguished based on a set of differentially expressed genes that we could validate separately.

Differential Expression Tests and Gene Set Enrichment Analysis (GSEA)

Tests for differential expression (DE) were performed using *MAST* version 1.4.1 (Finak et al., 2015). P values were corrected using the Benjamini-Hochberg method and filtered a 5% false discovery rate ($Q < 0.05$). GSEA was performed using the *fgsea* package version 1.4.1 in R (Sergushichev, 2016). Genes were ordered by Z scores from MAST DE tests on either the MSigDB mouse Hallmark gene sets or Reactome pathways separately. Combined Z scores were used for most genes, and discrete component Z scores were used for genes in which the continuous component was returned as NA (e.g. gene was not expressed in one of the two comparison groups). Enrichment scores were calculated using *fgsea* ($nperm = 100000$, $maxSize = Inf$). P values were corrected in *fgsea* using the Benjamini-Hochberg method. Gene sets and pathways were obtained using the *msigdb* package version 6.2.1.

Trajectory Inference

Trajectory inference was performed using *monocle* version 2.6.4 (Trapnell et al., 2014; Qiu et al., 2017). Raw count data from the *Seurat* microglia object was converted to a *CellDataSet* object using the *importCDS* function in *monocle*. Genes that were differentially expressed between microglial subclusters ($Q \text{ value} < 0.01$, $|\text{average log}_2 \text{ fold change}| \geq 1$) were set as the ordering genes. The minimum spanning tree was constructed using the *reduceDimensions* function ($reduction_method = "DDRTree"$, $num_dim = 10$, $norm_method = "log"$, $residualModelFormula = "~BatchID + nUMI + percent.mito"$, $relative_expr = TRUE$, $scaling = TRUE$).

Inference of Intercellular Interactions

Intercellular interactions were inferred using the *cellphoneDB* version 2.0 package in Python (Efremova et al., 2019; Vento-Tormo et al., 2018). A custom R script was used to export the single cell gene expression data from the curated *Seurat* object into a counts text file and metadata text file as recommended by the developers. Only genes with human orthologs were used, and mouse gene symbols were converted to the human ortholog gene symbols before data export using data from the *e!Ensembl* web portal. Data was processed in *cellphoneDB* with statistical analysis (default parameters, iterations = 1000, no sub-sampling). Data visualizations were made using *ph heatmap* and *ggplot2* in R based on the plotting functions provided in the *cellphoneDB* package.

Data Availability

Sequencing data from rabies-injected animals generated in this study will be available at NCBI GEO (Accession Number pending). The control dataset from uninjected animals was described in an earlier publication (Huang et al., 2019), and is available at NCBI GEO (accession number: GSE134163).

Chapter 4:
Conclusions & Future Directions

4.1 Resolving Subtypes and States from Transcriptional Heterogeneity

A major focus of this dissertation has been to understand the extensive degree of molecular heterogeneity between cells in the DRN. In Chapter 2, we began with charting a detailed map that describes the composition and organization of cells in the DRN. We showed that both neuronal and non-neuronal cell types in the DRN are comprised of many closely related but distinct subtypes that have different molecular and anatomical properties with functional implications. In Chapter 3, we leveraged on our molecular map of the DRN to examine the transcriptional changes that are coordinated across different cell types in response to viral infection. By profiling the gene expression profiles across over 60,000 single cells, we were able to distinguish between different types of immune cells despite the extensive overlaps in their gene expression patterns, and identified the cell types that may serve central roles in orchestrating the complex immune response. We also showed that activated microglia can exist in several transcriptionally distinct states along an activation trajectory. Using gene expression to infer intercellular interactions, we propose that interactions between microglia and T cells are important for transitions between these microglial activation states.

An important distinction between the work presented in Chapter 2 and Chapter 3 is the description of subtypes versus states. The main distinguishing feature between the two relates to the timescales of the underlying transcriptional dynamics. Here we define transcriptional states, such as the activation states that we described for microglia in Chapter 3, as being stable points along a dynamic process, whereby cells readily transition between different states under the appropriate conditions and stimuli. Subtypes on the other hand are not static, but describe endpoints along the branched trajectory of developmental processes occurring over longer

timescales. Unlike states, cells do not readily transition between subtype identities. The increase in stability or “rigidity” and resistance to transitions may be induced by changes that affect transcription such as chromatin modifications, as well as physical or morphological changes to the extracellular environment that alter the signals received by these cells. However, the “space” of gene expression defining a subtype may also encompass several states within them. Such transitions can be dependent on fast processes such as neuronal activity, cytokine signaling, or other stimuli that can trigger rapid transcriptional responses (Hrvatin et al., 2018; Okaty et al., 2019; Saunders et al., 2018).

While we have used both “subtypes” and “states” to describe different subclusters for various cell types, we recognize that scRNA-seq data provides a static snapshot of the gene expression in the brain that makes it difficult to distinguish between subtypes and states. Various methods have been used to infer dynamics and trajectories from scRNA-seq data (Saelens et al., 2019). However, theoretical limits faced by many of these methods still prevent them from fully resolving certain aspects of gene expression dynamics (Weinreb et al., 2018). Other methods are also being developed to recover information about dynamics by inferring the direction of transcriptional changes based on the kinetics of mRNA splicing and degradation (La Manno et al., 2018). Future studies examining gene expression dynamics will serve to place the findings from both chapters of this thesis in a larger context. In the case of Chapter 2, a study of the transcriptional dynamics along the developmental trajectory of the DRN and 5-HT neuron subtypes may provide insights into the mechanisms by which R1-derived DRN 5-HT neuron progenitors diverge as they are specified to form different subtypes. Such a study will also help to relate the subtypes that we describe in this study to other 5-HT neuron subsets described by

other studies, since some 5-HT neuron subsets continue to increase in abundance with age well beyond the age range that our study have examined (Niederkofler et al., 2016). One possibility is that the two closely related subtypes 5-HT-I and 5-HT-II may diverge further with age, with one of these subtypes increasing in its expression of the dopamine receptor *Drd2*. Studies comparing across a wider age range have also revealed aging-related changes in both transcriptional profiles and cell type composition in the brain (Dulken et al., 2019; Hammond et al., 2019; Mrdjen et al., 2018), which may be informative of mechanisms underlying aging-related cognitive decline. As we have discussed in Chapter 3, an important next-step for our study of the antiviral response is the reconstruction of the full response time course. Since our study only samples a single time point, follow-up experiments that sample across multiple time points may also reveal additional cell types that were not captured in our study, such as B cells, that may be involved in other phases of the immune response.

In addition to future work on transcriptional dynamics, comparative studies will also greatly complement our work on the mouse DRN. While we may expect a large degree of similarity across species since the serotonergic system is highly conserved, comparative studies will directly identify cell types in humans and their homologs in various model organisms. These studies will impact the design and interpretation of translational studies reliant on the use of these model organisms. Such comparative studies will be facilitated by the recent development of improved tools for the integrated analyses of datasets across both platforms and species (Welch et al., 2019; Stuart et al., 2019).

4.2 Functional Dissection of DRN Subcircuits – A Focus on the Basal Ganglia

In Chapter 2, we described several 5-HT neuron subtypes that form the cellular bases for distinct DRN 5-HT subcircuits. Additionally, our data suggests several intersectional approaches to begin dissecting the functions of several of these subtypes. At least 3 of the 5 subtypes that we have described are readily accessible using existing genetic driver lines: 5-HT-I (*Trh-IRES-Cre*), 5-HT-III (*Pdyn-IRES-Cre*), and 5-HT-IV (*VGluT3-IRES-Cre*). Furthermore, we demonstrated the feasibility of one of these approaches to access the *Pdyn*-enriched subtype 5-HT-III, which is well-positioned to modulate circuits of the basal ganglia.

The basal ganglia are a collection of subcortical structures that have important roles in the control of voluntary movements (Graybiel et al., 1994), habit formation (Everitt and Robbins, 2005; Dolan and Dayan, 2013), and decision-making (Ding and Gold, 2013). Several of these functions have also been attributed to DRN 5-HT neurons, suggesting that interactions between the basal ganglia and DRN 5-HT neurons are involved in these processes. The basal ganglia have also been implicated in many psychiatric disorders, including obsessive-compulsive disorder (OCD) (Graybiel and Rauch, 2000; Schilman et al., 2010), autism (Di Martino et al., 2011), depression (Buyukdura et al., 2011) and schizophrenia (Guillin et al., 2007; Shepherd, 2013).

Essentially all nuclei of the basal ganglia receive inputs from DRN 5-HT neurons, and approximately a third of all DRN 5-HT neurons innervate structures of the basal ganglia (Parent et al., 2011; Steinbusch et al., 1981). This is consistent with our finding that the striatum, the main input nucleus of the basal ganglia, receives inputs from multiple DRN 5-HT neuron subtypes. Additionally, our intersectional anterograde tracing showed that 5-HT-III neurons send

collaterals to multiple basal ganglia nuclei. This suggests that the 5-HT-III neurons are capable of modulating activity of basal ganglia inputs and outputs simultaneously, and that they perform their functions through their coordinated effects on all of their targets in the intact network, rather than its components in isolation. These features point in favor of using *in vivo* approaches to investigate the function of 5-HT-III neurons. Follow-up experiments are likely to include *in vivo* recordings of the neural spiking activity in multiple basal ganglia nuclei while stimulating 5-HT-III neurons using the Cre- and Flp-dependent ReaChR reporter line.

The effects of stimulating 5-HT neurons on the activity of the basal ganglia are complex given the organization of the basal ganglia. The basal ganglia is further comprised of subcircuits that are topographically organized into distinct cortico-basal ganglia-thalamic loops (Hintiryan et al., 2016; Mandelbaum et al., 2019). The striatum is also subdivided into distinct patch/striosome and matrix compartments that have different molecular, physiological, and anatomical properties (Banghart et al., 2015; Desban et al., 1993; Donoghue and Herkenham, 1986; Gerfen, 1984; Goldman-Rakic, 1982; Graybiel and Ragsdale, 1978). Many 5-HT receptors are expressed in different cell types throughout the basal ganglia, and these receptors can act on different subcellular compartments (Cavaccini et al., 2018), as well as distinct inputs to the striatum (Migueluez et al., 2014). Differential expression of 5-HT receptors can also have opposite effects on the same cell type in different regions of the striatum (Virk et al., 2016).

Our intersectional anterograde tracing results showed that the output nuclei of the basal ganglia are densely and uniformly innervated by *Pdyn*-expressing 5-HT-III neurons. Given the expression of G_i-coupled 5-HT_{1B} receptors at the axon terminals of striatal projection neurons

(Heiman et al., 2008) and a reduction in corticostriatal drive by 5-HT (Tassone et al., 2011; Mathur et al., 2011), we may expect an overall increase in the activity of basal ganglia output neurons resulting from a suppression of inhibitory inputs. Several possible behavioral outcomes of this disinhibition would be an overall suppression of motor output, which may manifest itself as a decrease in locomotion in an open field chamber (Correia et al., 2017), or an apparent improvement in performance on action restraint tasks (Miyazaki et al., 2014).

However, there are several reasons to expect that 5-HT-III neurons will exert effects on specific basal ganglia subcircuits rather than a generalized disinhibition of basal ganglia output.

Differential expression of G_q-coupled HTR2C receptor in the SNr (Allen Brain Atlas; Saunders et al., 2018) might lead to a preferential increase in the excitability of specific SNr output pathways and the inhibition of specific motor programs. 5-HT-III axons in the striatum are also not distributed uniformly (Figure 2.21), and are densest in the ventrolateral region of the dorsal striatum that is likely to regulate movements of the tongue and jaw (Hintiryan et al., 2016).

Additionally, distinct cell types in separate output pathways of the entopeduncular nucleus (EP; also referred to as the GPi) express different 5-HT receptors – habenula-projecting EP neurons express the inhibitory 5-HT1B receptors at their axon terminals in the lateral habenula (Shabel et al., 2012; Wallace et al., 2017), which is not innervated by 5-HT-III neurons. This output pathway of the basal ganglia is therefore under the modulatory control of a different DRN 5-HT neuron subtype, which we speculate to be either 5-HT-I or 5-HT-II.

Our results also showed that the VGluT3-enriched 5-HT-IV neurons form a separate subcircuit from the DRN to the basal ganglia. Other studies performing intersectional anterograde tracing

of VGluT3-expressing DRN 5-HT neurons, likely corresponding to our 5-HT-IV cluster, showed that these neurons innervate frontal cortical areas, which are the main source of excitatory drive to the striatum (Ren et al., 2018; Ren et al., 2019). VGluT3-expressing 5-HT neurons are also likely to send collaterals to the VTA where they can increase the activity of dopaminergic inputs to the striatum and nucleus accumbens (Wang et al., 2019; Liu et al., 2014), whereas 5-HT-III neurons send much weaker projections to the VTA and SNc. The distinct innervation of different elements of the cortico-basal ganglia network by 5-HT-III and 5-HT-IV suggests that these two distinct DRN subsystems may modulate separate functions of the basal ganglia. We speculate that 5-HT-IV neurons may have functions in modulating both activity and plasticity in cortico-basal ganglia circuits that mediate reinforcement learning, whereas 5-HT-III neurons serve to modulate basal ganglia-dependent action selection, initiation, and execution.

Few models of basal ganglia circuits have incorporated the DRN and its projections to the basal ganglia. Most of these consider the function of 5-HT in the context of a Parkinsonian disease state and L-DOPA administration since it has been suggested that striatal 5-HT afferents can uptake L-DOPA and release DA as a false transmitter (Huot and Fox, 2013; Politis and Niccolini, 2014; Reed et al., 2013). Other models have proposed that 5-HT has functions in reinforcement learning and decision making through its interactions with other neuromodulatory systems, such as the DA system (Balasubramani et al., 2014; Boureau and Dayan, 2011; Cools et al., 2011; Doya, 2002). Evaluating the proposed functions of 5-HT neuron subtypes in each of these models will require recording either the activity of specific subtypes or their release of 5-HT in their terminal fields while animals are engaged in a flexible decision-making task, such as a probabilistic choice switching task. Tasks with block designs may also be suitable for

identifying shifts in the strategies undertaken by each animal following changes in either the external environment, such as a change in reward probabilities, or the internal state of the animal, such as motivational drive.

4.3 From Transcriptional Types to Behavioral States

In Chapter 1, we reviewed several morphological and anatomical features of DRN 5-HT neurons that make them well-suited for mediating long timescale behavioral changes, or behavioral states, driven by fluctuations in internal state. 5-HT neurons signal broadly to networks of functionally related regions, and receive inputs from many regions that are likely to convey information about internal state. The activity of 5-HT neurons are known to track changes across multiple timescales (Cohen et al., 2015), and most 5-HT receptors, being G protein-coupled receptors, act on the order of seconds to minutes that are compatible with the timescale of changes in internal and behavioral states.

To assess if 5-HT neuron subtypes mediate distinct state-dependent changes in behavior through its effects on basal ganglia output, a framework for monitoring neural activity while tracking changes in internal and/or behavioral state will be needed. However, most studies of internal and behavioral states have depended largely on qualitative definitions; apart from sleep states, most experimentally induced states are described in binary modes, such as hunger/thirst versus satiety (Lowell, 2019; Sternson et al., 2013), depressive versus manic states (Kato et al., 2016), and active versus quiet waking (Fu et al., 2014; McGinley et al., 2015). The simultaneous measurement of both neural activity with internal state is still an outstanding challenge, since internal state is comprised of a large number of physiological variables (e.g. hormone levels) that

can be difficult or impractical to measure directly in awake behaving animals. More abstract aspects of internal state such as social rank, emotional states, and belief states, which are likely to have a distributed neural representation rather than a low dimensional physiological correlate, are also challenging to define in objective and quantifiable ways. Methods for estimating internal state from measurable variables such as behavior will need to be developed. One possible approach is to estimate internal state from measurements of behavioral variables and the dynamics of behavioral changes (Markowitz et al., 2018; Wiltschko et al., 2015). While quantitative analysis of behavior is not a direct measurement of the physiological substrates of internal state changes, factors reflective of internal state processes may be estimated or modeled as latent variables influencing the dynamics of behavioral and neural activity. Structural changes in behavior on longer timescales can also be identified and used as proxies for the underlying changes in internal state that drive them. Improved methods for elucidating the intrinsic structure of behavior across species and individuals and the development of detailed behavioral reference maps will greatly complement existing cell type census efforts towards understanding how the structure of the brain gives rise to its diverse functions.

References

- Agnoli, L., and Carli, M. (2012). Dorsal-striatal 5-HT_{2A} and 5-HT_{2C} receptors control impulsivity and perseverative responding in the 5-choice serial reaction time task. *Psychopharmacology* 219, 633–645.
- Azmitia, E.C. (2010). Evolution of Serotonin: Sunlight to Suicide. In *Handbook of the Behavioral Neurobiology of Serotonin*, C.P. Müller, and B.L. Jacobs, eds. (Elsevier).
- Azmitia, E.C., and Segal, M. (1978). An autoradiographic analysis of the differential ascending projections of the dorsal and median raphe nuclei in the rat. *J Comp Neurol* 179, 641–667.
- Balasubramani, P.P., Chakravarthy, V.S., Ravindran, B., and Moustafa, A.A. (2014). An extended reinforcement learning model of basal ganglia to understand the contributions of serotonin and dopamine in risk-based decision making, reward prediction, and punishment learning. *Front Comput Neurosci* 8, 47.
- Banasr, M., Hery, M., Printemps, R., and Daszuta, A. (2004). Serotonin-induced increases in adult cell proliferation and neurogenesis are mediated through different and common 5-HT receptor subtypes in the dentate gyrus and the subventricular zone. *Neuropsychopharmacology* 29, 450–460.
- Bang, S.J., Jensen, P., Dymecki, S.M., and Commons, K.G. (2012). Projections and interconnections of genetically defined serotonin neurons in mice. *Eur J Neurosci* 35, 85–96.
- Banghart, M.R., Neufeld, S.Q., Wong, N.C., and Sabatini, B.L. (2015). Enkephalin Disinhibits Mu Opioid Receptor-Rich Striatal Patches via Delta Opioid Receptors. *Neuron* 88, 1227–1239.
- Bari, A., and Robbins, T.W. (2013). Inhibition and impulsivity: behavioral and neural basis of response control. *Prog. Neurobiol.* 108, 44–79.
- Baumann, B., Bielau, H., Krell, D., Agelink, M.W., Diekmann, S., Wurthmann, C., Trübner, K., Bernstein, H.G., Danos, P., and Bogerts, B. (2002). Circumscribed numerical deficit of dorsal raphe neurons in mood disorders. *Psychol Med* 32, 93–103.
- Boureau, Y.-L., and Dayan, P. (2011). Opponency revisited: competition and cooperation between dopamine and serotonin. *Neuropsychopharmacology* 36, 74–97.
- Brisch, R., Steiner, J., Mawrin, C., Krzyżanowska, M., Jankowski, Z., and Gos, T. (2017). Microglia in the dorsal raphe nucleus plays a potential role in both suicide facilitation and prevention in affective disorders. *Eur Arch Psychiatry Clin Neurosci* 267, 403–415.
- Bromberg-Martin, E.S., Hikosaka, O., and Nakamura, K. (2010). Coding of task reward value in the dorsal raphe nucleus. *J Neurosci* 30, 6262–6272.
- Brzózka, K., Finke, S., and Conzelmann, K.-K. (2006). Inhibition of interferon signaling by rabies virus phosphoprotein P: activation-dependent binding of STAT1 and STAT2. *J Virol* 80, 2675–2683.

- Butler, A., Hoffman, P., Smibert, P., Papalexi, E., and Satija, R. (2018). Integrating single-cell transcriptomic data across different conditions, technologies, and species. *Nat. Biotechnol.*
- Buyukdura, J.S., McClintock, S.M., and Croarkin, P.E. (2011). Psychomotor retardation in depression: biological underpinnings, measurement, and treatment. *Prog Neuropsychopharmacol Biol Psychiatry* *35*, 395–409.
- Calabresi, P., Picconi, B., Tozzi, A., Ghiglieri, V., and Di Filippo, M. (2014). Direct and indirect pathways of basal ganglia: a critical reappraisal. *Nat Neurosci* *17*, 1022–1030.
- Calizo, L.H., Akanwa, A., Ma, X., Pan, Y.-Z., Lemos, J.C., Craige, C., Heemstra, L.A., and Beck, S.G. (2011). Raphe serotonin neurons are not homogenous: electrophysiological, morphological and neurochemical evidence. *Neuropharmacology* *61*, 524–543.
- Cavaccini, A., Gritti, M., Giorgi, A., Locarno, A., Heck, N., Migliarini, S., Bertero, A., Mereu, M., Margiani, G., Trusel, M., et al. (2018). Serotonergic Signaling Controls Input-Specific Synaptic Plasticity at Striatal Circuits. *Neuron* *98*, 801–816.e807.
- Chan, K.Y., Jang, M.J., Yoo, B.B., Greenbaum, A., Ravi, N., Wu, W.-L., Sánchez-Guardado, L., Lois, C., Mazmanian, S.K., Deverman, B.E., et al. (2017). Engineered AAVs for efficient noninvasive gene delivery to the central and peripheral nervous systems. *Nat Neurosci* *20*, 1172–1179.
- Chatterjee, S., Sullivan, H.A., MacLennan, B.J., Xu, R., Hou, Y., Lavin, T.K., Lea, N.E., Michalski, J.E., Babcock, K.R., Dietrich, S., et al. (2018). Nontoxic, double-deletion-mutant rabies viral vectors for retrograde targeting of projection neurons. *Nat Neurosci* *4*, 1–16.
- Chen, A.-Q., Fang, Z., Chen, X.-L., Yang, S., Zhou, Y.-F., Mao, L., Xia, Y.-P., Jin, H.-J., Li, Y.-N., You, M.-F., et al. (2019). Microglia-derived TNF- α mediates endothelial necroptosis aggravating blood brain-barrier disruption after ischemic stroke. *Cell Death Dis* *10*, 487.
- Chen, K.H., Boettiger, A.N., Moffitt, J.R., Wang, S., and Zhuang, X. (2015). Spatially resolved, highly multiplexed RNA profiling in single cells. *Science* *348*, aaa6090.
- Cho, J.R., Treweek, J.B., Robinson, J.E., Xiao, C., Bremner, L.R., Greenbaum, A., and Gradinaru, V. (2017). Dorsal Raphe Dopamine Neurons Modulate Arousal and Promote Wakefulness by Salient Stimuli. *Neuron* *94*, 1205–1219.e1208.
- Cohen, J.Y., Amoroso, M.W., and Uchida, N. (2015). Serotonergic neurons signal reward and punishment on multiple timescales. *Elife* *4*, 463.
- Colgan, L.A., Cavolo, S.L., Commons, K.G., and Levitan, E.S. (2012). Action potential-independent and pharmacologically unique vesicular serotonin release from dendrites. *J Neurosci* *32*, 15737–15746.
- Commons, K.G. (2015). Two major network domains in the dorsal raphe nucleus. *J Comp Neurol* *523*, 1488–1504.

- Cools, R., Nakamura, K., and Daw, N.D. (2011). Serotonin and dopamine: unifying affective, activational, and decision functions. *Neuropsychopharmacology* 36, 98–113.
- Cools, R., Roberts, A.C., and Robbins, T.W. (2008). Serotonergic regulation of emotional and behavioural control processes. *Trends Cogn Sci (Regul Ed)* 12, 31–40.
- Correia, P.A., Lottem, E., Banerjee, D., Machado, A.S., Carey, M.R., and Mainen, Z.F. (2017). Transient inhibition and long-term facilitation of locomotion by phasic optogenetic activation of serotonin neurons. *Elife* 6, 365.
- Dahlström, A., and Fuxe, K. (1964). Localization of monoamines in the lower brain stem. *Experientia* 20, 398–399.
- Davis, M., Strachan, D.I., and Kass, E. (1980). Excitatory and inhibitory effects of serotonin on sensorimotor reactivity measured with acoustic startle. *Science* 209, 521–523.
- de Kock, C.P.J., Cornelisse, L.N., Burnashev, N., Lodder, J.C., Timmerman, A.J., Couey, J.J., Mansvelder, H.D., and Brussaard, A.B. (2006). NMDA receptors trigger neurosecretion of 5-HT within dorsal raphe nucleus of the rat in the absence of action potential firing. *The Journal of Physiology* 577, 891–905.
- Deneris, E., and Gaspar, P. (2018). Serotonin neuron development: shaping molecular and structural identities. *Wiley Interdiscip Rev Dev Biol* 7.
- Desban, M., Kemel, M.L., Glowinski, J., and Gauchy, C. (1993). Spatial organization of patch and matrix compartments in the rat striatum. *Nsc* 57, 661–671.
- Di Liberto, G., Pantelyushin, S., Kreutzfeldt, M., Page, N., Musardo, S., Coras, R., Steinbach, K., Vincenti, I., Klimek, B., Lingner, T., et al. (2018). Neurons under T Cell Attack Coordinate Phagocyte-Mediated Synaptic Stripping. *Cell* 175, 458–471.e19.
- Di Martino, A., Kelly, C., Grzadzinski, R., Zuo, X.-N., Mennes, M., Mairena, M.A., Lord, C., Castellanos, F.X., and Milham, M.P. (2011). Aberrant striatal functional connectivity in children with autism. *Biol Psychiatry* 69, 847–856.
- Di Matteo, V., Pierucci, M., Esposito, E., Crescimanno, G., Benigno, A., and Di Giovanni, G. (2008). Serotonin modulation of the basal ganglia circuitry: therapeutic implication for Parkinson's disease and other motor disorders. *Prog Brain Res* 172, 423–463.
- Ding, L., and Gold, J.I. (2013). The Basal Ganglia's Contributions to Perceptual Decision Making. 79, 640–649.
- Dolan, R.J., and Dayan, P. (2013). Goals and habits in the brain. 80, 312–325.
- Donoghue, J.P., and Herkenham, M. (1986). Neostriatal projections from individual cortical fields conform to histochemically distinct striatal compartments in the rat. *Brain Res* 365, 397–403.

- Dougalis, A.G., Matthews, G.A.C., Bishop, M.W., Brischoux, F., Kobayashi, K., and Ungless, M.A. (2012). Functional properties of dopamine neurons and co-expression of vasoactive intestinal polypeptide in the dorsal raphe nucleus and ventro-lateral periaqueductal grey. *Eur. J. Neurosci.* *36*, 3322–3332.
- Doya, K. (2002). Metalearning and neuromodulation. *Neural Netw* *15*, 495–506.
- Dölen, G., Darvishzadeh, A., Huang, K.W., and Malenka, R.C. (2013). Social reward requires coordinated activity of nucleus accumbens oxytocin and serotonin. *Nature* *501*, 179–184.
- Drokhlyansky, E., Göz Aytürk, D., Soh, T.K., Chrenek, R., O’Loughlin, E., Madore, C., Butovsky, O., and Cepko, C.L. (2017). The brain parenchyma has a type I interferon response that can limit virus spread. *Proc Natl Acad Sci USA* *114*, E95–E104.
- Dugue, G.P., Lörincz, M.L., Lottem, E., Audero, E., Matias, S., Correia, P.A., Léna, C., and Mainen, Z.F. (2014). Optogenetic recruitment of dorsal raphe serotonergic neurons acutely decreases mechanosensory responsivity in behaving mice. *PLoS ONE* *9*, e105941.
- Dulken, B.W., Buckley, M.T., Navarro Negredo, P., Saligrama, N., Cayrol, R., Leeman, D.S., George, B.M., Boutet, S.C., Hebestreit, K., Pluvinage, J.V., et al. (2019). Single-cell analysis reveals T cell infiltration in old neurogenic niches. *Nature* *571*, 205–210.
- Ecker, J.R., Geschwind, D.H., Kriegstein, A.R., Ngai, J., Osten, P., Polioudakis, D., Regev, A., Šestan, N., Wickersham, I.R., and Zeng, H. (2017). The BRAIN Initiative Cell Census Consortium: Lessons Learned toward Generating a Comprehensive Brain Cell Atlas. *Neuron* *96*, 542–557.
- Economo, M.N., Clack, N.G., Lavis, L.D., Gerfen, C.R., Svoboda, K., Myers, E.W., and Chandrashekar, J. (2016). A platform for brain-wide imaging and reconstruction of individual neurons. *Elife* *5*, e10566.
- Efremova, M., Vento-Tormo, M., Teichmann, S.A., and Vento-Tormo, R. (2019). CellPhoneDB v2.0: Inferring cell-cell communication from combined expression of multi-subunit receptor-ligand complexes. *bioRxiv* *563*.
- Ekstrand, M.I., Nectow, A.R., Knight, Z.A., Latcha, K.N., Pomeranz, L.E., and Friedman, J.M. (2014). Molecular profiling of neurons based on connectivity. *Cell* *157*, 1230–1242.
- Everitt, B.J., and Robbins, T.W. (2005). Neural systems of reinforcement for drug addiction: from actions to habits to compulsion. *Nat Neurosci* *8*, 1481–1489.
- Faul, E.J., Lyles, D.S., and Schnell, M.J. (2009). Interferon response and viral evasion by members of the family rhabdoviridae. *Viruses* *1*, 832–851.
- Fenno, L.E., Mattis, J., Ramakrishnan, C., Hyun, M., Lee, S.Y., He, M., Tucciarone, J., Selimbeyoglu, A., Berndt, A., Grosenick, L., et al. (2014). Targeting cells with single vectors using multiple-feature Boolean logic. *Nat Meth* *11*, 763–772.

- Ferguson, J.M. (2001). SSRI Antidepressant Medications: Adverse Effects and Tolerability. *Prim Care Companion J Clin Psychiatry* 3, 22–27.
- Fernandez, S.P., Cauli, B., Cabezas, C., Muzerelle, A., Poncer, J.-C., and Gaspar, P. (2015). Multiscale single-cell analysis reveals unique phenotypes of raphe 5-HT neurons projecting to the forebrain. *Brain Struct Funct* 221, 1–19.
- Finak, G., McDavid, A., Yajima, M., Deng, J., Gersuk, V., Shalek, A.K., Slichter, C.K., Miller, H.W., McElrath, M.J., Prlic, M., et al. (2015). MAST: a flexible statistical framework for assessing transcriptional changes and characterizing heterogeneity in single-cell RNA sequencing data. *Genome Biology* 16, 278.
- Fisone, G., Snyder, G.L., Fryckstedt, J., Caplan, M.J., Aperia, A., and Greengard, P. (1995). Na⁺,K⁽⁺⁾-ATPase in the choroid plexus. Regulation by serotonin/protein kinase C pathway. *J. Biol. Chem.* 270, 2427–2430.
- Fitzgerald-Bocarsly, P., Dai, J., and Singh, S. (2008). Plasmacytoid dendritic cells and type I IFN: 50 years of convergent history. *Cytokine Growth Factor Rev.* 19, 3–19.
- Fonseca, M.S., Murakami, M., and Mainen, Z.F. (2015). Activation of dorsal raphe serotonergic neurons promotes waiting but is not reinforcing. *Curr Biol* 25, 306–315.
- Fremeau, R.T., Burman, J., Qureshi, T., Tran, C.H., Proctor, J., Johnson, J., Zhang, H., Sulzer, D., Copenhagen, D.R., Storm-Mathisen, J., et al. (2002). The identification of vesicular glutamate transporter 3 suggests novel modes of signaling by glutamate. *Proc Natl Acad Sci USA* 99, 14488–14493.
- Fu, W., Le Maître, E., Fabre, V., Bernard, J.-F., David Xu, Z.-Q., and Hökfelt, T. (2010). Chemical neuroanatomy of the dorsal raphe nucleus and adjacent structures of the mouse brain. *J Comp Neurol* 518, 3464–3494.
- Fu, Y., Tucciarone, J.M., Espinosa, J.S., Sheng, N., Darcy, D.P., Nicoll, R.A., Huang, Z.J., and Stryker, M.P. (2014). A cortical circuit for gain control by behavioral state. *Cell* 156, 1139–1152.
- Gagnon, D., and Parent, M. (2014). Distribution of VGLUT3 in highly collateralized axons from the rat dorsal raphe nucleus as revealed by single-neuron reconstructions. *PLoS ONE* 9, e87709.
- Gartlehner, G., Hansen, R.A., Morgan, L.C., Thaler, K., Lux, L., Van Noord, M., Mager, U., Thieda, P., Gaynes, B.N., Wilkins, T., et al. (2011). Comparative benefits and harms of second-generation antidepressants for treating major depressive disorder: an updated meta-analysis. *Ann. Intern. Med.* 155, 772–785.
- Gerfen, C.R. (1984). The neostriatal mosaic: compartmentalization of corticostriatal input and striatonigral output systems. *Nature* 311, 461–464.
- Ghanem, A., and Conzelmann, K.-K. (2016). G gene-deficient single-round rabies viruses for neuronal circuit analysis. *Virus Res.* 216, 41–54.

Goldman-Rakic, P.S. (1982). Cytoarchitectonic heterogeneity of the primate neostriatum: subdivision into Island and Matrix cellular compartments. *J Comp Neurol* 205, 398–413.

Gong, H., Xu, D., Yuan, J., Li, X., Guo, C., Peng, J., Li, Y., Schwarz, L.A., Li, A., Hu, B., et al. (2016). High-throughput dual-colour precision imaging for brain-wide connectome with cytoarchitectonic landmarks at the cellular level. *Nature Communications* 7, 12142.

Grailhe, R., Grabtree, G.W., and Hen, R. (2001). Human 5-HT(5) receptors: the 5-HT(5A) receptor is functional but the 5-HT(5B) receptor was lost during mammalian evolution. *Eur. J. Pharmacol.* 418, 157–167.

Granger, A.J., Wallace, M.L., and Sabatini, B.L. (2017). Multi-transmitter neurons in the mammalian central nervous system. *Current Opinion in Neurobiology* 45, 85–91.

Graybiel, A.M., and Ragsdale, C.W. (1978). Histochemically distinct compartments in the striatum of human, monkeys, and cat demonstrated by acetylthiocholinesterase staining. *Proc Natl Acad Sci USA* 75, 5723–5726.

Graybiel, A.M., and Rauch, S.L. (2000). Toward a neurobiology of obsessive-compulsive disorder. *28*, 343–347.

Graybiel, A.M., Aosaki, T., Flaherty, A.W., and Kimura, M. (1994). The basal ganglia and adaptive motor control. *Science* 265, 1826–1831.

Guillin, O., Abi Dargham, A., and Laruelle, M. (2007). Neurobiology of dopamine in schizophrenia. *Int Rev Neurobiol* 78, 1–39.

Hale, M.W., and Lowry, C.A. (2011). Functional topography of midbrain and pontine serotonergic systems: implications for synaptic regulation of serotonergic circuits. *Psychopharmacology* 213, 243–264.

Hall, I.C., Rebec, G.V., and Hurley, L.M. (2010). Serotonin in the inferior colliculus fluctuates with behavioral state and environmental stimuli. *J. Exp. Biol.* 213, 1009–1017.

Hammond, T.R., Dufort, C., Dissing-Olesen, L., Giera, S., Young, A., Wysoker, A., Walker, A.J., Gergits, F., Segel, M., Nemesh, J., et al. (2019). Single-Cell RNA Sequencing of Microglia throughout the Mouse Lifespan and in the Injured Brain Reveals Complex Cell-State Changes. *Immunity* 50, 253–271.e256.

Haugas, M., Tikker, L., Achim, K., Salminen, M., and Partanen, J. (2016). Gata2 and Gata3 regulate the differentiation of serotonergic and glutamatergic neuron subtypes of the dorsal raphe. *Development* 143, 4495–4508.

Hayashi, K., Nakao, K., and Nakamura, K. (2015). Appetitive and aversive information coding in the primate dorsal raphé nucleus. *J Neurosci* 35, 6195–6208.

Heiman, M., Schaefer, A., Gong, S., Peterson, J.D., Day, M., Ramsey, K.E., Suárez-Fariñas, M., Schwarz, C., Stephan, D.A., Surmeier, D.J., et al. (2008). A translational profiling approach for

the molecular characterization of CNS cell types. *Cell* 135, 738–748.

Hendricks, T., Francis, N., Fyodorov, D., and Deneris, E.S. (1999). The ETS domain factor Pet-1 is an early and precise marker of central serotonin neurons and interacts with a conserved element in serotonergic genes. *Journal of Neuroscience* 19, 10348–10356.

Henstridge, C.M., Hyman, B.T., and Spires-Jones, T.L. (2019). Beyond the neuron–cellular interactions early in Alzheimer disease pathogenesis. *Nat Rev Neurosci* 20, 1–15.

Hintiryan, H., Foster, N.N., Bowman, I., Bay, M., Song, M.Y., Gou, L., Yamashita, S., Bienkowski, M.S., Zingg, B., Zhu, M., et al. (2016). The mouse cortico-striatal projectome. *Nat Neurosci* 19, 1100–1114.

Hioki, H., Nakamura, H., Ma, Y.-F., Konno, M., Hayakawa, T., Nakamura, K.C., Fujiyama, F., and Kaneko, T. (2010). Vesicular glutamate transporter 3-expressing nonserotonergic projection neurons constitute a subregion in the rat midbrain raphe nuclei. *J Comp Neurol* 518, 668–686.

Hornung, J.-P. (2010). The Neuroanatomy of the Serotonergic System. In *Handbook of the Behavioral Neurobiology of Serotonin*, C.P. Müller, and B.L. Jacobs, eds. (Elsevier), pp. 51–64.

Howerton, A.R., Roland, A.V., and Bale, T.L. (2014). Dorsal raphe neuroinflammation promotes dramatic behavioral stress dysregulation. *J Neurosci* 34, 7113–7123.

Hrvatin, S., Hochbaum, D.R., Nagy, M.A., Cicconet, M., Robertson, K., Cheadle, L., Zilionis, R., Ratner, A., Borges-Monroy, R., Klein, A.M., et al. (2018). Single-cell analysis of experience-dependent transcriptomic states in the mouse visual cortex. *Nat Neurosci* 21, 120–129.

Huang, K.W., Ochandarena, N.E., Philson, A.C., Hyun, M., Birnbaum, J.E., Cicconet, M., and Sabatini, B.L. (2019). Molecular and anatomical organization of the dorsal raphe nucleus. *Elife* 8.

Huot, P., and Fox, S.H. (2013). The serotonergic system in motor and non-motor manifestations of Parkinson's disease. *Exp Brain Res* 230, 463–476.

Huot, P., Fox, S.H., and Brotchie, J.M. (2011). The serotonergic system in Parkinson's disease. *Prog. Neurobiol.* 95, 163–212.

Inaba, K., Mizuhiki, T., Setogawa, T., Toda, K., Richmond, B.J., and Shidara, M. (2013). Neurons in monkey dorsal raphe nucleus code beginning and progress of step-by-step schedule, reward expectation, and amount of reward outcome in the reward schedule task. *J Neurosci* 33, 3477–3491.

Jacobs, B.L., and Fornal, C.A. (1997). Serotonin and motor activity. *Current Opinion in Neurobiology* 7, 820–825.

Jensen, P., Farago, A.F., Awatramani, R.B., Scott, M.M., Deneris, E.S., and Dymecki, S.M. (2008). Redefining the serotonergic system by genetic lineage. *Nat Neurosci* 11, 417–419.

- Jordão, M.J.C., Sankowski, R., Brendecke, S.M., Sagar, Locatelli, G., Tai, Y.-H., Tay, T.L., Schramm, E., Armbruster, S., Hagemeyer, N., et al. (2019). Single-cell profiling identifies myeloid cell subsets with distinct fates during neuroinflammation. *Science* 363.
- Kato, T., Kasahara, T., Kubota-Sakashita, M., Kato, T.M., and Nakajima, K. (2016). Animal models of recurrent or bipolar depression. *Neuroscience* 321, 189–196.
- Kaushalya, S.K., Desai, R., Arumugam, S., Ghosh, H., Balaji, J., and Maiti, S. (2008). Three-photon microscopy shows that somatic release can be a quantitatively significant component of serotonergic neurotransmission in the mammalian brain. *J. Neurosci. Res.* 86, 3469–3480.
- Kawashima, T., Zwart, M.F., Yang, C.-T., Mensh, B.D., and Ahrens, M.B. (2016). The Serotonergic System Tracks the Outcomes of Actions to Mediate Short-Term Motor Learning. *Cell* 167, 933–946.e20.
- Kebschull, J.M., Garcia da Silva, P., Reid, A.P., Peikon, I.D., Albeanu, D.F., and Zador, A.M. (2016). High-Throughput Mapping of Single-Neuron Projections by Sequencing of Barcoded RNA. *Neuron* 91, 975–987.
- Kim, I.-J., Beck, H.N., Lein, P.J., and Higgins, D. (2002). Interferon gamma induces retrograde dendritic retraction and inhibits synapse formation. *J Neurosci* 22, 4530–4539.
- Kiyasova, V., Bonnavion, P., Scotto-Lomassese, S., Fabre, V., Sahly, I., Tronche, F., Deneris, E., Gaspar, P., and Fernandez, S.P. (2013). A subpopulation of serotonergic neurons that do not express the 5-HT1A autoreceptor. *ACS Chem Neurosci* 4, 89–95.
- Klein, A.M., Mazutis, L., Akartuna, I., Tallapragada, N., Veres, A., Li, V., Peshkin, L., Weitz, D.A., and Kirschner, M.W. (2015). Droplet barcoding for single-cell transcriptomics applied to embryonic stem cells. *Cell* 161, 1187–1201.
- Kunkle, B.W., Grenier-Boley, B., Sims, R., Bis, J.C., Damotte, V., Naj, A.C., Boland, A., Vronskaya, M., van der Lee, S.J., Amlie-Wolf, A., et al. (2019). Genetic meta-analysis of diagnosed Alzheimer's disease identifies new risk loci and implicates A β , tau, immunity and lipid processing. *Nat. Genet.* 51, 414–430.
- La Manno, G., Soldatov, R., Zeisel, A., Braun, E., Hochgerner, H., Petukhov, V., Lidschreiber, K., Kastrioti, M.E., Lönnerberg, P., Furlan, A., et al. (2018). RNA velocity of single cells. *Nature* 560, 494–498.
- Lee, S.-B., Lee, H.S., and Waterhouse, B.D. (2008). The collateral projection from the dorsal raphe nucleus to whisker-related, trigeminal sensory and facial motor systems in the rat. *Brain Res* 1214, 11–22.
- Lein, E.S., Hawrylycz, M.J., Ao, N., Ayres, M., Bensinger, A., Bernard, A., Boe, A.F., Boguski, M.S., Brockway, K.S., Byrnes, E.J., et al. (2007). Genome-wide atlas of gene expression in the adult mouse brain. *Nature* 445, 168–176.
- Li, Q., Cheng, Z., Zhou, L., Darmanis, S., Neff, N.F., Okamoto, J., Gulati, G., Bennett, M.L.,

- Sun, L.O., Clarke, L.E., et al. (2019). Developmental Heterogeneity of Microglia and Brain Myeloid Cells Revealed by Deep Single-Cell RNA Sequencing. *Neuron* *101*, 207–223.e210.
- Li, Y., Zhong, W., Wang, D., Feng, Q., Liu, Z., Zhou, J., Jia, C., Hu, F., Zeng, J., Guo, Q., et al. (2016). Serotonin neurons in the dorsal raphe nucleus encode reward signals. *Nature Communications* *7*, 10503.
- Liberzon, A., Birger, C., Thorvaldsdóttir, H., Ghandi, M., Mesirov, J.P., and Tamayo, P. (2015). The Molecular Signatures Database (MSigDB) hallmark gene set collection. *Cell Syst* *1*, 417–425.
- Liu, Z., Zhou, J., Li, Y., Hu, F., Lu, Y., Ma, M., Feng, Q., Zhang, J.-E., Wang, D., Zeng, J., et al. (2014). Dorsal Raphe Neurons Signal Reward through 5-HT and Glutamate. *81*, 1360–1374.
- Lottem, E., Banerjee, D., Vertech, P., Sarra, D., Lohuis, M.O., and Mainen, Z.F. (2018). Activation of serotonin neurons promotes active persistence in a probabilistic foraging task. *Nature Communications* *9*, 1000.
- Lowell, B.B. (2019). New Neuroscience of Homeostasis and Drives for Food, Water, and Salt. *N Engl J Med* *380*, 459–471.
- Lowry, C.A. (2002). Functional subsets of serotonergic neurones: implications for control of the hypothalamic-pituitary-adrenal axis. *J. Neuroendocrinol.* *14*, 911–923.
- Lowry, C.A., Rodda, J.E., Lightman, S.L., and Ingram, C.D. (2000). Corticotropin-releasing factor increases in vitro firing rates of serotonergic neurons in the rat dorsal raphe nucleus: evidence for activation of a topographically organized mesolimbocortical serotonergic system. *J Neurosci* *20*, 7728–7736.
- Luo, L., Callaway, E.M., and Svoboda, K. (2008). Genetic dissection of neural circuits. *57*, 634–660.
- Luo, L., Callaway, E.M., and Svoboda, K. (2018). Genetic Dissection of Neural Circuits: A Decade of Progress. *Neuron* *98*, 256–281.
- Mahmood, T., and Silverstone, T. (2001). Serotonin and bipolar disorder. *J Affect Disord* *66*, 1–11.
- Mandelbaum, G., Taranda, J., Haynes, T.M., Hochbaum, D.R., Huang, K.W., Hyun, M., Venkataraju, K.U., Straub, C., Wang, W., Robertson, K., et al. (2019). Distinct Cortical-Thalamic-Striatal Circuits through the Parafascicular Nucleus. *Neuron* 1–25.
- Marcinkiewicz, C.A., Mazzone, C.M., D'Agostino, G., Halladay, L.R., Hardaway, J.A., DiBerto, J.F., Navarro, M., Burnham, N., Cristiano, C., Dorrier, C.E., et al. (2016). Serotonin engages an anxiety and fear-promoting circuit in the extended amygdala. *Nature* *537*, 97–101.
- Markowitz, J.E., Gillis, W.F., Beron, C.C., Neufeld, S.Q., Robertson, K., Bhagat, N.D., Peterson, R.E., Peterson, E., Hyun, M., Linderman, S.W., et al. (2018). The Striatum Organizes 3D

Behavior via Moment-to-Moment Action Selection. *Cell* 174, 44–58.e17.

Marques, S., Zeisel, A., Codeluppi, S., van Bruggen, D., Mendanha Falcão, A., Xiao, L., Li, H., Häring, M., Hochgerner, H., Romanov, R.A., et al. (2016). Oligodendrocyte heterogeneity in the mouse juvenile and adult central nervous system. *Science* 352, 1326–1329.

Masuda, T., Sankowski, R., Staszewski, O., Böttcher, C., Amann, L., Scheiwe, C., Nessler, S., Kunz, P., Loo, G., Coenen, V.A., et al. (2019). Spatial and temporal heterogeneity of mouse and human microglia at single-cell resolution. *Nature* 570, 1–23.

Mathur, B.N., Capik, N.A., Alvarez, V.A., and Lovinger, D.M. (2011). Serotonin induces long-term depression at corticostriatal synapses. *J Neurosci* 31, 7402–7411.

Mathys, H., Davila-Velderrain, J., Peng, Z., Gao, F., Mohammadi, S., Young, J.Z., Menon, M., He, L., Abdurrob, F., Jiang, X., et al. (2019). Single-cell transcriptomic analysis of Alzheimer's disease. *Nature* 570, 332–337.

Matias, S., Lottem, E., Dugue, G.P., and Mainen, Z.F. (2017). Activity patterns of serotonin neurons underlying cognitive flexibility. *Elife* 6, 365.

Matthews, G.A., Nieh, E.H., Vander Weele, C.M., Halbert, S.A., Pradhan, R.V., Yosafat, A.S., Globber, G.F., Izadmehr, E.M., Thomas, R.E., Lacy, G.D., et al. (2016). Dorsal Raphe Dopamine Neurons Represent the Experience of Social Isolation. *Cell* 164, 617–631.

Matthews, P.R., and Harrison, P.J. (2012). A morphometric, immunohistochemical, and in situ hybridization study of the dorsal raphe nucleus in major depression, bipolar disorder, schizophrenia, and suicide. *J Affect Disord* 137, 125–134.

Maurer, P., Rorive, S., de Kerchove d'Exaerde, A., Schiffmann, S.N., Salmon, I., and de Launoit, Y. (2004). The Ets transcription factor Fev is specifically expressed in the human central serotonergic neurons. *Neurosci Lett* 357, 215–218.

McDevitt, R.A., Tiran-Cappello, A., Shen, H., Balderas, I., Britt, J.P., Marino, R.A.M., Chung, S.L., Richie, C.T., Harvey, B.K., and Bonci, A. (2014). Serotonergic versus nonserotonergic dorsal raphe projection neurons: differential participation in reward circuitry. *Cell Rep* 8, 1857–1869.

McGinley, M.J., Vinck, M., Reimer, J., Batista-Brito, R., Zagha, E., Cadwell, C.R., Tolias, A.S., Cardin, J.A., and McCormick, D.A. (2015). Waking State: Rapid Variations Modulate Neural and Behavioral Responses. *Neuron* 87, 1143–1161.

Meltzer, H.Y., and Massey, B.W. (2011). The role of serotonin receptors in the action of atypical antipsychotic drugs. *Curr Opin Pharmacol* 11, 59–67.

Michelsen, K.A., Schmitz, C., and Steinbusch, H.W.M. (2007). The dorsal raphe nucleus--from silver stainings to a role in depression. *Brain Res Rev* 55, 329–342.

Migueluez, C., Morera-Herreras, T., Torrecilla, M., Ruiz-Ortega, J.A., and Ugedo, L. (2014).

- Interaction between the 5-HT system and the basal ganglia: functional implication and therapeutic perspective in Parkinson's disease. *Front. Neural Circuits* 8, 21.
- Miyazaki, K., Miyazaki, K.W., and Doya, K. (2012). The role of serotonin in the regulation of patience and impulsivity. *Mol. Neurobiol.* 45, 213–224.
- Miyazaki, K.W., Miyazaki, K., Tanaka, K.F., Yamanaka, A., Takahashi, A., Tabuchi, S., and Doya, K. (2014). Optogenetic Activation of Dorsal Raphe Serotonin Neurons Enhances Patience for Future Rewards. *Curr Biol* 24, 2033–2040.
- Monti, J.M. (2010). The structure of the dorsal raphe nucleus and its relevance to the regulation of sleep and wakefulness. *Sleep Medicine Reviews* 14, 307–317.
- Monti, J.M. (2011). Serotonin control of sleep-wake behavior. *Sleep Medicine Reviews* 15, 269–281.
- Moskowitz, M.A., Liebmann, J.E., Reinhard, J.F., and Schlosberg, A. (1979). Raphe origin of serotonin-containing neurons within choroid plexus of the rat. *Brain Res* 169, 590–594.
- Mrdjen, D., Pavlovic, A., Hartmann, F.J., Schreiner, B., Utz, S.G., Leung, B.P., Lelios, I., Heppner, F.L., Kipnis, J., Merkler, D., et al. (2018). High-Dimensional Single-Cell Mapping of Central Nervous System Immune Cells Reveals Distinct Myeloid Subsets in Health, Aging, and Disease. *Immunity* 48, 380–395.e386.
- Mundell, N.A., Beier, K.T., Pan, Y.A., Lapan, S.W., Göz Aytürk, D., Berezovskii, V.K., Wark, A.R., Drokhlyansky, E., Bielecki, J., Born, R.T., et al. (2015). Vesicular stomatitis virus enables gene transfer and transsynaptic tracing in a wide range of organisms. *J Comp Neurol* 523, 1639–1663.
- Muzerelle, A., Scotto-Lomassese, S., Bernard, J.-F., Soiza-Reilly, M., and Gaspar, P. (2016). Conditional anterograde tracing reveals distinct targeting of individual serotonin cell groups (B5-B9) to the forebrain and brainstem. *Brain Struct Funct* 221, 535–561.
- Nakamura, K., Matsumoto, M., and Hikosaka, O. (2008). Reward-dependent modulation of neuronal activity in the primate dorsal raphe nucleus. *J Neurosci* 28, 5331–5343.
- Nautiyal, K.M., Tanaka, K.F., Barr, M.M., Tritschler, L., Le Dantec, Y., David, D.J., Gardier, A.M., Blanco, C., Hen, R., and Ahmari, S.E. (2015). Distinct Circuits Underlie the Effects of 5-HT_{1B} Receptors on Aggression and Impulsivity. 86, 813–826.
- Nectow, A.R., Schneeberger, M., Zhang, H., Field, B.C., Renier, N., Azevedo, E., Patel, B., Liang, Y., Mitra, S., Tessier-Lavigne, M., et al. (2017). Identification of a Brainstem Circuit Controlling Feeding. *Cell* 170, 429–442.e11.
- Niederkofler, V., Asher, T.E., Okaty, B.W., Rood, B.D., Narayan, A., Hwa, L.S., Beck, S.G., Miczek, K.A., and Dymecki, S.M. (2016). Identification of Serotonergic Neuronal Modules that Affect Aggressive Behavior. *Cell Rep* 17, 1934–1949.

- Ogawa, S.K., Cohen, J.Y., Hwang, D., Uchida, N., and Watabe-Uchida, M. (2014). Organization of monosynaptic inputs to the serotonin and dopamine neuromodulatory systems. *Cell Rep* 8, 1105–1118.
- Oh, S.W., Harris, J.A., Ng, L., Winslow, B., Cain, N., Mihalas, S., Wang, Q., Lau, C., Kuan, L., Henry, A.M., et al. (2014). A mesoscale connectome of the mouse brain. *Nature* 508, 207–214.
- Okaty, B.W., Commons, K.G., and Dymecki, S.M. (2019). Embracing diversity in the 5-HT neuronal system. *Nat Rev Neurosci* 169, 800.
- Okaty, B.W., Freret, M.E., Rood, B.D., Brust, R.D., Hennessy, M.L., deBairos, D., Kim, J.C., Cook, M.N., and Dymecki, S.M. (2015). Multi-Scale Molecular Deconstruction of the Serotonin Neuron System. *Neuron* 1–42.
- Osakada, F., and Callaway, E.M. (2013). Design and generation of recombinant rabies virus vectors. *Nat Protoc* 8, 1583–1601.
- Oyibo, H., Cao, C., Ferrante, D.D., Zhan, H., Koulakov, A.A., Enquist, L., Dubnau, J., and Zador, A. (2018). A computational framework for converting high-throughput DNA sequencing data into neural circuit connectivity. *bioRxiv* 1–13.
- Parent, M., Wallman, M.-J., Gagnon, D., and Parent, A. (2011). Serotonin innervation of basal ganglia in monkeys and humans. *J Chem Neuroanat* 41, 256–265.
- Pauls, D.L., Abramovitch, A., Rauch, S.L., and Geller, D.A. (2014). Obsessive-compulsive disorder: an integrative genetic and neurobiological perspective. *Nat Rev Neurosci* 15, 410–424.
- Paxinos, G., and Franklin, K.B.J. (2001). *The Mouse Brain in Stereotaxic Coordinates* (San Diego, California, USA: Academic Press).
- Pfaar, H., Holst, von, A., Vogt Weisenhorn, D.M., Brodski, C., Guimera, J., and Wurst, W. (2002). mPet-1, a mouse ETS-domain transcription factor, is expressed in central serotonergic neurons. *Dev. Genes Evol.* 212, 43–46.
- Pfefferkorn, C., Kallfass, C., Lienenklaus, S., Spanier, J., Kalinke, U., Rieder, M., Conzelmann, K.-K., Michiels, T., and Staeheli, P. (2016). Abortively Infected Astrocytes Appear To Represent the Main Source of Interferon Beta in the Virus-Infected Brain. *J Virol* 90, 2031–2038.
- Pisanello, F., Sileo, L., Oldenburg, I.A., Pisanello, M., Martiradonna, L., Assad, J.A., Sabatini, B.L., and De Vittorio, M. (2014). Multipoint-Emitting Optical Fibers for Spatially Addressable In Vivo Optogenetics.
- Politis, M., and Niccolini, F. (2014). Serotonin in Parkinson's disease. *Behav Brain Res.*
- Pollak Dorocic, I., Fürth, D., Xuan, Y., Johansson, Y., Pozzi, L., Silberberg, G., Carlén, M., and Meletis, K. (2014). A whole-brain atlas of inputs to serotonergic neurons of the dorsal and median raphe nuclei. 83, 663–678.

- Poulin, J.-F., Caronia, G., Hofer, C., Cui, Q., Helm, B., Ramakrishnan, C., Chan, C.S., Dombeck, D.A., Deisseroth, K., and Awatramani, R. (2018). Mapping projections of molecularly defined dopamine neuron subtypes using intersectional genetic approaches. *Nat Neurosci* 21, 1260–1271.
- Poulin, J.-F., Zou, J., Drouin-Ouellet, J., Kim, K.-Y.A., Cicchetti, F., and Awatramani, R.B. (2014). Defining midbrain dopaminergic neuron diversity by single-cell gene expression profiling. *Cell Rep* 9, 930–943.
- Prosniak, M., Hooper, D.C., Dietzschold, B., and Koprowski, H. (2001). Effect of rabies virus infection on gene expression in mouse brain. *Proc Natl Acad Sci USA* 98, 2758–2763.
- Prouty, E.W., Chandler, D.J., and Waterhouse, B.D. (2017). Neurochemical differences between target-specific populations of rat dorsal raphe projection neurons. *Brain Res* 1675, 28–40.
- Qiu, X., Mao, Q., Tang, Y., Wang, L., Chawla, R., Pliner, H.A., and Trapnell, C. (2017). Reversed graph embedding resolves complex single-cell trajectories. *Nat Meth* 14, 979–982.
- Ranade, S.P., and Mainen, Z.F. (2009). Transient firing of dorsal raphe neurons encodes diverse and specific sensory, motor, and reward events. *J Neurophysiol* 102, 3026–3037.
- Ray, R.S., Corcoran, A.E., Brust, R.D., Kim, J.C., Richerson, G.B., Nattie, E., and Dymecki, S.M. (2011). Impaired respiratory and body temperature control upon acute serotonergic neuron inhibition. *Science* 333, 637–642.
- Reardon, T.R., Murray, A.J., Turi, G.F., Wirblich, C., Croce, K.R., Schnell, M.J., Jessell, T.M., and Losonczy, A. (2016). Rabies Virus CVS-N2c(Δ G) Strain Enhances Retrograde Synaptic Transfer and Neuronal Viability. *Neuron* 89, 711–724.
- Reed, M.C., Nijhout, H.F., and Best, J. (2013). Computational studies of the role of serotonin in the basal ganglia. *Front Integr Neurosci* 7, 41.
- Regev, A., Teichmann, S.A., Lander, E.S., Amit, I., Benoist, C., Birney, E., Bodenmiller, B., Campbell, P., Carninci, P., Clatworthy, M., et al. (2017). The Human Cell Atlas. *Elife* 6, 503.
- Ren, J., Friedmann, D., Xiong, J., Liu, C.D., Ferguson, B.R., Weerakkody, T., DeLoach, K.E., Ran, C., Pun, A., Sun, Y., et al. (2018). Anatomically Defined and Functionally Distinct Dorsal Raphe Serotonin Sub-systems. *Cell* 175, 472–487.e20.
- Ren, J., Isakova, A., Friedmann, D., Zeng, J., Grutzner, S., Pun, A., Zhao, G.Q., Kolluru, S.S., Wang, R., Lin, R., et al. (2019). Serotonin Neurons in the Dorsal and Medial Raphe Nuclei: from Single-Cell Transcriptomes to Whole-Brain Projections. *bioRxiv* 16, A261–57.
- Root, D.H., Zhang, S., Barker, D.J., Miranda-Barrientos, J., Liu, B., Wang, H.-L., and Morales, M. (2018). Selective Brain Distribution and Distinctive Synaptic Architecture of Dual Glutamatergic-GABAergic Neurons. *Cell Rep* 23, 3465–3479.
- Saelens, W., Cannoodt, R., Todorov, H., and Saeys, Y. (2019). A comparison of single-cell trajectory inference methods. *Nat. Biotechnol.* 37, 547–554.

- Satija, R., Farrell, J.A., Gennert, D., Schier, A.F., and Regev, A. (2015). Spatial reconstruction of single-cell gene expression data. *Nat. Biotechnol.* *33*, 495–502.
- Saunders, A., Macosko, E.Z., Wysoker, A., Goldman, M., Krienen, F.M., de Rivera, H., Bien, E., Baum, M., Bortolin, L., Wang, S., et al. (2018). Molecular Diversity and Specializations among the Cells of the Adult Mouse Brain. *Cell* *174*, 1015–1030.e1016.
- Schilman, E.A., Klavir, O., Winter, C., Sohr, R., and Joel, D. (2010). The role of the striatum in compulsive behavior in intact and orbitofrontal-cortex-lesioned rats: possible involvement of the serotonergic system. *Neuropsychopharmacology* *35*, 1026–1039.
- Schneeberger, M., Parolari, L., Banerjee, Das, T., Bhave, V., Wang, P., Patel, B., Topilko, T., Wu, Z., Choi, C.H.J., Yu, X., et al. (2019). Regulation of Energy Expenditure by Brainstem GABA Neurons. *Cell* *178*, 672–685.e12.
- Scott, T.P., and Nel, L.H. (2016). Subversion of the Immune Response by Rabies Virus. *Viruses* *8*.
- Sekar, A., Bialas, A.R., de Rivera, H., Davis, A., Hammond, T.R., Kamitaki, N., Tooley, K., Presumey, J., Baum, M., Van Doren, V., et al. (2016). Schizophrenia risk from complex variation of complement component 4. *Nature* *530*, 177–183.
- Seo, C., Guru, A., Jin, M., Ito, B., Sleezer, B.J., Ho, Y.-Y., Wang, E., Boada, C., Krupa, N.A., Kullakanda, D.S., et al. (2019). Intense threat switches dorsal raphe serotonin neurons to a paradoxical operational mode. *Science* *363*, 538–542.
- Sergushichev, A.A. (2016). An algorithm for fast preranked gene set enrichment analysis using cumulative statistic calculation. *bioRxiv* 1–9.
- Shabel, S.J., Proulx, C.D., Trias, A., Murphy, R.T., and Malinow, R. (2012). Input to the lateral habenula from the basal ganglia is excitatory, aversive, and suppressed by serotonin. *Neuron* *74*, 475–481.
- Shepherd, G.M.G. (2013). Corticostriatal connectivity and its role in disease. *Nat Rev Neurosci* *14*, 278–291.
- Shrestha, B., Zhang, B., Purtha, W.E., Klein, R.S., and Diamond, M.S. (2008). Tumor necrosis factor alpha protects against lethal West Nile virus infection by promoting trafficking of mononuclear leukocytes into the central nervous system. *J Virol* *82*, 8956–8964.
- Shutoh, F., Ina, A., Yoshida, S., Konno, J., and Hisano, S. (2008). Two distinct subtypes of serotonergic fibers classified by co-expression with vesicular glutamate transporter 3 in rat forebrain. *Neurosci Lett* *432*, 132–136.
- Spaethling, J.M., Piel, D., Dueck, H., Buckley, P.T., Morris, J.F., Fisher, S.A., Lee, J., Sul, J.-Y., Kim, J., Bartfai, T., et al. (2014). Serotonergic neuron regulation informed by in vivo single-cell transcriptomics. *Faseb J.* *28*, 771–780.

- Steinbusch, H.W., Nieuwenhuys, R., Verhofstad, A.A., and van der Kooy, D. (1981). The nucleus raphe dorsalis of the rat and its projection upon the caudatoputamen. A combined cytoarchitectonic, immunohistochemical and retrograde transport study. *J. Physiol. (Paris)* 77, 157–174.
- Sternson, S.M., Nicholas Betley, J., and Cao, Z.F.H. (2013). Neural circuits and motivational processes for hunger. *Current Opinion in Neurobiology* 23, 353–360.
- Stuart, T., Butler, A., Hoffman, P., Hafemeister, C., Papalexi, E., Mauck, W.M., Hao, Y., Stoerckius, M., Smibert, P., and Satija, R. (2019). Comprehensive Integration of Single-Cell Data. *Cell* 177, 1888–1902.e21.
- Subramanian, A., Tamayo, P., Mootha, V.K., Mukherjee, S., Ebert, B.L., Gillette, M.A., Paulovich, A., Pomeroy, S.L., Golub, T.R., Lander, E.S., et al. (2005). Gene set enrichment analysis: a knowledge-based approach for interpreting genome-wide expression profiles. *Proc Natl Acad Sci USA* 102, 15545–15550.
- Takase, L.F., Nogueira, M.I., Baratta, M., Bland, S.T., Watkins, L.R., Maier, S.F., Fornal, C.A., and Jacobs, B.L. (2004). Inescapable shock activates serotonergic neurons in all raphe nuclei of rat. *Behav Brain Res* 153, 233–239.
- Tasic, B., Yao, Z., Graybiel, L.T., Smith, K.A., Nguyen, T.N., Bertagnoli, D., Goldy, J., Garren, E., Economou, M.N., Viswanathan, S., et al. (2018). Shared and distinct transcriptomic cell types across neocortical areas. *Nature* 563, 72–78.
- Tassone, A., Madeo, G., Schirinzi, T., Vita, D., Puglisi, F., Ponterio, G., Borsini, F., Pisani, A., and Bonsi, P. (2011). Activation of 5-HT₆ receptors inhibits corticostriatal glutamatergic transmission. *Neuropharmacology* 61, 632–637.
- Templin, J.S., Bang, S.J., Soiza-Reilly, M., Berde, C.B., and Commons, K.G. (2012). Patterned expression of ion channel genes in mouse dorsal raphe nucleus determined with the Allen Mouse Brain Atlas. *Brain Res* 1457, 1–12.
- Trapnell, C., Cacchiarelli, D., Grimsby, J., Pokharel, P., Li, S., Morse, M., Lennon, N.J., Livak, K.J., Mikkelsen, T.S., and Rinn, J.L. (2014). The dynamics and regulators of cell fate decisions are revealed by pseudotemporal ordering of single cells. *Nat. Biotechnol.* 32, 381–386.
- Urban, D.J., Zhu, H., Marcinkiewicz, C.A., Michaelides, M., Oshibuchi, H., Rhea, D., Aryal, D.K., Farrell, M.S., Lowery-Gionta, E., Olsen, R.H.J., et al. (2016). Elucidation of The Behavioral Program and Neuronal Network Encoded by Dorsal Raphe Serotonergic Neurons. *Neuropsychopharmacology* 41, 1404–1415.
- Ursin, R. (2002). Serotonin and sleep. *Sleep Medicine Reviews* 6, 55–69.
- Van Bockstaele, E.J., Biswas, A., and Pickel, V.M. (1993). Topography of serotonin neurons in the dorsal raphe nucleus that send axon collaterals to the rat prefrontal cortex and nucleus accumbens. *Brain Res* 624, 188–198.

- van den Pol, A.N., Ding, S., and Robek, M.D. (2014). Long-distance interferon signaling within the brain blocks virus spread. *J Virol* 88, 3695–3704.
- Vanlandewijck, M., He, L., Mäe, M.A., Andrae, J., Ando, K., Del Gaudio, F., Nahar, K., Lebouvier, T., Laviña, B., Gouveia, L., et al. (2018). A molecular atlas of cell types and zonation in the brain vasculature. *Nature Publishing Group* 554, 475–480.
- Vaswani, M., Linda, F.K., and Ramesh, S. (2003). Role of selective serotonin reuptake inhibitors in psychiatric disorders: a comprehensive review. *Prog Neuropsychopharmacol Biol Psychiatry* 27, 85–102.
- Vento-Tormo, R., Efremova, M., Botting, R.A., Turco, M.Y., Vento-Tormo, M., Meyer, K.B., Park, J.-E., Stephenson, E., Polański, K., Goncalves, A., et al. (2018). Single-cell reconstruction of the early maternal-fetal interface in humans. *Nature* 563, 347–353.
- Vertes, R.P. (1991). A PHA-L analysis of ascending projections of the dorsal raphe nucleus in the rat. *J Comp Neurol* 313, 643–668.
- Virk, M.S., Sagi, Y., Medrihan, L., Leung, J., Kaplitt, M.G., and Greengard, P. (2016). Opposing roles for serotonin in cholinergic neurons of the ventral and dorsal striatum. *Proc Natl Acad Sci USA* 113, 734–739.
- Wallace, M.L., Saunders, A., Huang, K.W., Philson, A.C., Goldman, M., Macosko, E.Z., McCarroll, S.A., and Sabatini, B.L. (2017). Genetically Distinct Parallel Pathways in the Entopeduncular Nucleus for Limbic and Sensorimotor Output of the Basal Ganglia. *Neuron* 94, 138–152.e5.
- Wang, H.-L., Zhang, S., Qi, J., Wang, H., Cachope, R., Mejias-Aponte, C.A., Gomez, J.A., Mateo-Semidey, G.E., Beaudoin, G.M.J., Paladini, C.A., et al. (2019). Dorsal Raphe Dual Serotonin-Glutamate Neurons Drive Reward by Establishing Excitatory Synapses on VTA Mesoaccumbens Dopamine Neurons. *Cell Rep* 26, 1128–1142.e7.
- Wang, X., Allen, W.E., Wright, M.A., Sylwestrak, E.L., Samusik, N., Vesuna, S., Evans, K., Liu, C., Ramakrishnan, C., Liu, J., et al. (2018). Three-dimensional intact-tissue sequencing of single-cell transcriptional states. *Science* 361.
- Wasselus, M., Valentino, R.J., and Van Bockstaele, E.J. (2011). Collateralized dorsal raphe nucleus projections: a mechanism for the integration of diverse functions during stress. *J Chem Neuroanat* 41, 266–280.
- Waterhouse, B.D., Mihailoff, G.A., Baack, J.C., and Woodward, D.J. (1986). Topographical distribution of dorsal and median raphe neurons projecting to motor, sensorimotor, and visual cortical areas in the rat. *J Comp Neurol* 249, 460–76–478–81.
- Watkins, C.C., Sawa, A., and Pomper, M.G. (2014). Glia and immune cell signaling in bipolar disorder: insights from neuropharmacology and molecular imaging to clinical application. *Nature Publishing Group* 4, e350.

Weinreb, C., Wolock, S., Tusi, B.K., Socolovsky, M., and Klein, A.M. (2018). Fundamental limits on dynamic inference from single-cell snapshots. *Proc Natl Acad Sci USA* *115*, E2467–E2476.

Weissbourd, B., Ren, J., DeLoach, K.E., Guenther, C.J., Miyamichi, K., and Luo, L. (2014). Presynaptic partners of dorsal raphe serotonergic and GABAergic neurons. *83*, 645–662.

Welch, J.D., Kozareva, V., Ferreira, A., Vanderburg, C., Martin, C., and Macosko, E.Z. (2019). Single-Cell Multi-omic Integration Compares and Contrasts Features of Brain Cell Identity. *Cell* *177*, 1873–1887.e17.

Wickersham, I.R., Lyon, D.C., Barnard, R.J.O., Mori, T., Finke, S., Conzelmann, K.-K., Young, J.A.T., and Callaway, E.M. (2007). Monosynaptic restriction of transsynaptic tracing from single, genetically targeted neurons. *53*, 639–647.

Wickersham, I.R., Sullivan, H.A., and Seung, H.S. (2010). Production of glycoprotein-deleted rabies viruses for monosynaptic tracing and high-level gene expression in neurons. *Nat Protoc* *5*, 595–606.

Wiltschko, A.B., Johnson, M.J., Iurilli, G., Peterson, R.E., Katon, J.M., Pashkovski, S.L., Abaira, V.E., Adams, R.P., and Datta, S.R. (2015). Mapping Sub-Second Structure in Mouse Behavior. *Neuron* *88*, 1121–1135.

Wyler, S.C., Spencer, W.C., Green, N.H., Rood, B.D., Crawford, L., Craige, C., Gresch, P., McMahon, D.G., Beck, S.G., and Deneris, E. (2016). Pet-1 Switches Transcriptional Targets Postnatally to Regulate Maturation of Serotonin Neuron Excitability. *J Neurosci* *36*, 1758–1774.

Yokogawa, T., Hannan, M.C., and Burgess, H.A. (2012). The dorsal raphe modulates sensory responsiveness during arousal in zebrafish. *J Neurosci* *32*, 15205–15215.

Young, M.D., Wakefield, M.J., Smyth, G.K., and Oshlack, A. (2010). Gene ontology analysis for RNA-seq: accounting for selection bias. *Genome Biology* *11*, R14.

Young, S.Z., Taylor, M.M., and Bordey, A. (2011). Neurotransmitters couple brain activity to subventricular zone neurogenesis. *Eur J Neurosci* *33*, 1123–1132.

Zeisel, A., Hochgerner, H., Lönnerberg, P., Johnsson, A., Memic, F., van der Zwan, J., Häring, M., Braun, E., Borm, L.E., La Manno, G., et al. (2018). Molecular Architecture of the Mouse Nervous System. *Cell* *174*, 999–1014.e22.

Zeng, H., and Sanes, J.R. (2017). Neuronal cell-type classification: challenges, opportunities and the path forward. *Nat Rev Neurosci* *18*, 530–546.

Zhao, P., Liu, S., Zhong, Z., Jiang, T., Weng, R., Xie, M., Yang, S., and Xia, X. (2018). Analysis of expression profiles of long noncoding RNAs and mRNAs in brains of mice infected by rabies virus by RNA sequencing. *Sci Rep* *8*, 11858.

Zhao, P., Zhao, L., Zhang, T., Qi, Y., Wang, T., Liu, K., Wang, H., Feng, H., Jin, H., Qin, C., et

al. (2011). Innate immune response gene expression profiles in central nervous system of mice infected with rabies virus. *Comp. Immunol. Microbiol. Infect. Dis.* *34*, 503–512.

Zilionis, R., Nainys, J., Veres, A., Savova, V., Zemmour, D., Klein, A.M., and Mazutis, L. (2017). Single-cell barcoding and sequencing using droplet microfluidics. *Nat Protoc* *12*, 44–73.